CHALMERS

Energy-efficient Generating System for HVDC Off-shore Wind Turbine

POOPAK ROSHANFEKR

Department of Energy and Environment
Division of Electric Power Engineering
CHALMERS UNIVERSITY OF TECHNOLOGY
Göteborg, Sweden 2013

THESIS FOR THE DEGREE OF LICENTIATE OF ENGINEERING

Energy-efficient Generating System for HVDC Off-shore Wind Turbine

POOPAK ROSHANFEKR

Department of Energy and Environment
Division of Electric Power Engineering
CHALMERS UNIVERSITY OF TECHNOLOGY
Göteborg, Sweden 2013

Energy-efficient Generating System for HVDC Off-shore Wind Turbine
POOPAK ROSHANFEKR

To dear Sonja whose unlimited support
made this work to be done

iv

Energy-efficient Generating System for HVDC Off-shore Wind Turbine
POOPAK ROSHANFEKR
Department of Energy and Environment
Division of Electric Power Engineering
Chalmers University of Technology

Abstract

This thesis investigates the design of energy efficient generating systems for off-shore wind turbines. For the generator part of the electric drive system, a surface mounted permanent magnet synchronous generator (SPMSG), an interior permanent magnet generator (IPMSG) as well as a synchronous reluctance generator (SynRG) have been investigated. The system includes a gearbox to increase the rotor speed to be suitable for the generator speed. The system is investigated with IGBT-equipped converters. Furthermore, different dc-link voltages are studied.

The results indicate that the most suitable system when cost is ignored includes an IPMSG with a dc-link voltage between the voltage level that gives maximum torque per ampere operation for the whole operation region and the minimum dc-link voltage level which gives the required rated torque. If the IPMSG is replaced by a SynRG with the same size, 74% of the IPMSG rated power can be converted. Furthermore, if instead a SPMSG with the same size is used, the annual energy efficiency of the system is lower compared to the IPMSG, and for both the SynRG and the SPMSG, the power factor becomes lower, compared to the IPMSG. One found disadvantage of the IPMSG is the relatively high torque ripple. Therefore, two methods to reduce the torque ripple are suggested and investigated, showing a substantial torque ripple reduction of about two thirds if either a fractional slot winding or if skewing of the stator is used.

Index Terms: high voltage direct current (HVDC), wind energy, IGBT active rectifier, surface permanent magnet synchronous generator (SPMSG), interior permanent magnet synchronous generator (IPMSG), synchronous reluctance generator (SynRG), finite element method (FEM), dc-link voltage, diode (passive) rectifier, annual energy efficiency.

Acknowledgements

I would like to express my special thanks to my supervisor, Associate Professor Sonja Tidblad Lundmark for giving me the best support and supervision that was ever possible. Her excellent knowledge, wise advices, kindness and patience made every moment of working with her enjoyable. Her active participation in this work and her trust in me encouraged me to continue my studies during the time that I was very frustrated.

I am also indebted to my co-supervisor Dr. Mikael Alatalo for his nice discussions and inputs. The technical insight of the examiner of this work Prof. Torbjörn Thiringer is highly appreciated.

I would like to express my thanks to all members of the reference group of the off-shore HVDC wind park project, with special gratitude to Dr. Aron Szucs for his great comments and ideas regarding my part of the wind park project.

I wish to also thank my dear friend Arash Mazaheri for his great work within a part of the project and thanks to Sergio García Colino and Shamim Keshavarz for their contribution to this thesis.

Many thanks go to Eva, Lotten and Bengt for being there for me during the tough times.

Last but definitely not least, I owe my sincere gratitude to my family for their support and encouragement.

Poopak Roshanfekr
Göteborg, Sweden, 2013

Contents

Chapter 1

Introduction

1.1 Background and motivation

An increase in usage of electricity and a diversity of utilization of energy sources for electricity production are future scenarios all over the world. In Europe, there is currently much work on developments in the energy field in order to meet the climate targets 20-20-20 by reducing carbon emissions, increasing the proportion of energy from renewable energy sources and increasing energy efficiency. One of the interesting renewable energy sources for generation of electrical power is wind energy. The expansion of wind power takes place both on land (on-shore) and at sea (off-shore). However, today most wind turbines are erected on land. Problems with finding suitable places to install wind farms on land and the existence of huge fairly shallow areas in the North Sea and the Baltic Sea where off-shore wind farms can be located, has prompted a great interest in placing off-shore wind farms, which is also advantageous because of favorable wind conditions.

For large off-shore wind farms with a long distance to the shore, High Voltage Direct Current (HVDC) transmission offers technical and economical advantages in comparison with Alternating Current (AC) connections [1]- [2]. An example of a wind farm using a dc-transmission system is the Borkum wind park. Figure 1.1 shows the generating and transmission system used in Borkum. Even though a dc-transmission is used for the Borkum wind farm, still 50/60 Hz technology, for instance bulky 50/60 Hz transformers are used within the park. A future possibility for remote off-shore wind farms could be a dc-transmission line, a high frequency dc/dc converter instead of a 50/60 Hz transformer and a completely dc-based wind energy collection system as seen in Fig. 1.2. In this case the need for heavy and large platforms is reduced. Another observation is that the choice of dc-link voltage for the generating system becomes fairly freely selectable.

Most wind turbine generators operate at a generator voltage level of 690 V. The highest voltage level used within an on-shore wind farm is usually in the range of 33-36 kV. Off-shore wind farms tend to be bigger and often the distance to the next transformer station is longer than for on-shore wind farms. Therefore, higher voltage levels can be useful for off-

shore applications in order to minimize the power losses. However, since the size and cost of the transformer are increased for higher voltage levels, a collection voltage of 36 kV seems to be the most cost-effective solution for the off-shore wind turbines as well [3]. In future off-shore wind farms if a high frequency dc/dc transformer is used instead of a 50/60 Hz transformer, a dc voltage level of 40-70 kV for the energy transportation to the collection point could be appropriate. This voltage is too high to connect an inverter and operate the wind turbine generator directly from. Accordingly, a dc/dc converter is needed to boost the voltage, before the energy is sent out into the grid.

The design of a high voltage generating system that collects the distributed wind energy with a high energy efficiency at a low cost can be a challenge.
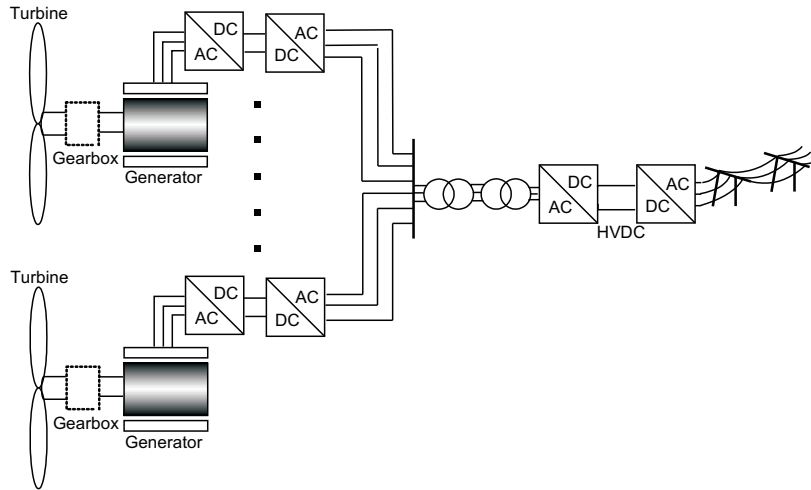

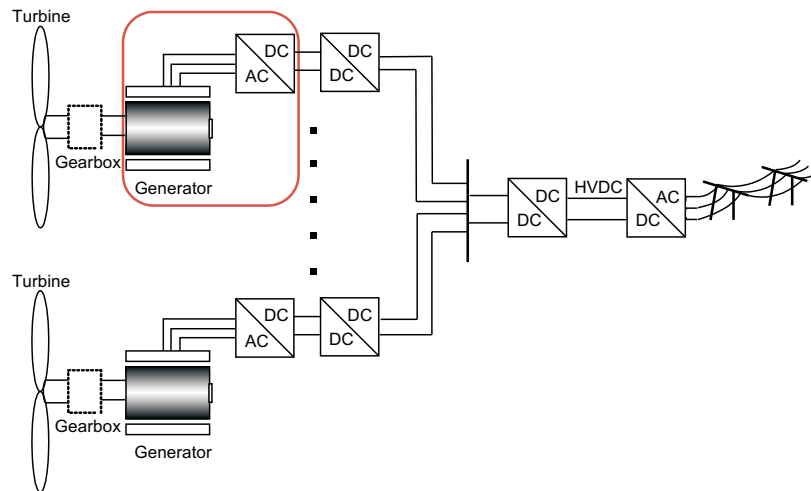Figure 1.1: Generator and transmission system in the Borkum wind farm.

Figure 1.2: Generator and transmission system in the future remote off-shore wind farms.

Permanent magnet synchronous generators are popular in wind turbine application nowadays, since they have higher torque to weight ratio compared to other AC generators [4] and a good efficiency. When using a PMSG a choice can be made between using surface mounted magnets and magnets placed inside the rotor. SPMSGs can more easily have a lower torque ripple, while IPMSGs on the other hand generate flux concentration in the rotor that can allow thinner magnets [5]. A comparison of interior and surface permanent magnet machines for traction purposes has been done in [6] in terms of power density, electrical efficiencies, losses and torque. In [7] four types of surface and interior permanent magnet generators are compared in order to introduce a suitable structure of a PMSG for a large-scale wind power generation system. However, that study had been conducted at the rated operating condition and the features that are compared are the average torque, power and efficiency. While, in wind turbine applications it is very important to have a high efficiency at lower wind since the wind speed is usually lower than the rated wind speed.

The Synchronous Reluctance Machine (SynRM) has a long history. The first SynRM was introduced by Kostko in 1923 [8]. The synchronous reluctance motor was developed particularly in the 1960's as a line-start synchronous AC motor [9]. During the 1990's a substantial amount of work and research on the design and control of synchronous reluctance motors have been done [9], [10], [11], [12], [13], [14] and [15]. Recently, the SynRM have been further improved [16], [17] and [18]. Even though most of the researchers have explored the application of the reluctance machine as a motor, the field of the synchronous reluctance generator (SynRG) has also been brought to attention [19], [20] and [21]. Several applications for synchronous reluctance machines are proposed in [22]. One of the interesting applications of the SynRG is for wind turbine generation systems [21], since SynRGs are robust, inexpensive and they have a simple rotor construction. Although synchronous permanent magnet motors often are a very good choice for many variable-speed drive applications, the advantages of using synchronous reluctance motors is that, the today very expensive magnets are not needed. In [21] a small wind turbine generation system with SynRG has been investigated. However, the system is not compared with any other generation systems.

Most MW size wind generating systems of today, use generator voltages of 690 V and then it is sufficient to use 1700 V IGBT components. An example is the Gamesa G10X 4.5 MW turbine which is a medium rotor speed permanent magnet generator [23]. There is, however, an interest to increase this voltage since a medium voltage drive train can be more convenient to install, due to the ability of operating at high power levels and accordingly lower current levels, leading to less extensive cabling. It then offers lower copper losses than the same rated low voltage set-up [24]. According to [25] and [26] the rated voltage of the IGBTs typically increases with increasing dc-link voltage for synchronous type generators. The off-shore Areva Multibrid M5000 wind turbine [27], which is a 5 MW permanent magnet synchronous generator with rated voltage of 3.3 kV

uses the ABB converter platform PCS 6000 Wind since the end of 2009 [24] [28]. This medium voltage converter has the voltage levels of 3.3 kV and 4.16 kV [29]. In [30] it was shown that the selection of dc-link voltage using a given module had an important impact on the losses. When going up in voltage there is a variety of high voltage IGBT modules that can be used, all the way up to 6.5 kV modules. If the voltage goes up, then the question is: Is it beneficial to use modules of higher voltage, still a couple in series, or is it better to use many of lower voltage modules? From an on-state loss point of view, it seems beneficial to use a module of higher voltage but how it is then with the switching losses and what is then the resulting total energy efficiency? It is stated in [31], that in industrial power conversion, low voltage converters are most cost-efficient at low power levels (up to 2 MW) while at high power levels medium voltage is preferable. It is also mentioned that the medium voltage converter have less components compared to a low voltage level converter, hence it is more reliable. However, the annual energy of the whole system was not mentioned.

1.2 Purpose of the thesis and main contributions

The aim of the thesis is to investigate different generating systems for off-shore wind turbines with HVDC connections. Main aspects are to study energy efficiencies and weight/cost of the system. To achieve the goal of the project, a 3 or 2 stage gearbox, a surface and an interior mounted permanent magnet synchronous generator as well as a synchronous reluctance generator with an active transistor converter have been studied. For the system with surface permanent magnet generator, a diode (passive) rectifier is investigated due to the lower cost potential. This thesis focuses mainly on the part inside the red box which is shown in Fig. 1.2.

To the best of author's knowledge, the main contribution of the thesis are:

- Determination of the power density and annual energy efficiency performance for two PMSM, with the same geometry, with magnets placed on the surface and inside the rotor.

- Investigation of the power density of a synchronous reluctance wind generator in relation to a permanent magnet synchronous generator.

- Comparative studies on the machine annual energy efficiency for a wind turbine consisting of a permanent magnet synchronous machine with a wind turbine comprising with a synchronous reluctance machine.

1.3 Structure of the thesis

This thesis is organized into 7 chapters. The first chapter describes the background information, motivation and purpose of the thesis. Chapter 2 -3 present the theory of the used machines and power electronics and in Chapter 4 the theory of wind turbine is presented. Chapter 5 builds the main structure of this thesis. This chapter presents the design of the generators and the design of the wind turbine converters. In Chapter 6 the analysis of the study is addressed. Finally, Chapter 7 concludes the thesis and present suggestions for the future work.

1.4 List of publications

The publications originating from the project are:

I. P. Roshanfekr, T. Thiringer and S. Lundmark, "Efficiency comparison of a 5 MW wind turbine PMSG-equipped generating system using various dc-link voltages," in *Electrical Vehicles and Renewable Energies (EVER) Conference on*, March 2012.

II. P. Roshanfekr, T. Thiringer , M. Alatalo and S. Lundmark, "Performance of two 5 MW permanent magnet wind turbine generators using surface mounted and interior mounted magnets," in *Electrical Machines (ICEM), 2012 XXth IEEE International Conference on*, 2012, pp. 1041-1047.

III. P. Roshanfekr, T. Thiringer , S. Lundmark and M. Alatalo, "Selecting IGBT module for a high voltage 5 MW wind turbine PMSG-equipped generating system," in *Power Electronics and Machines in Wind Applications (PEMWA), 2012 IEEE*, 2012, pp.1-6.

IV. P. Roshanfekr, T. Thiringer , S. Lundmark and M. Alatalo, "DC-link voltage selection for a multi-MW wind turbine", submitted to COMPEL *The International Journal for Computation and Mathematics in Electrical and Electronic Engineering*, Paper under review.

Chapter 2

Machine theory

In this section the theory of different machines which are used in this work will be explained.

2.1 Basic machine theory

First we review some of the basic magnetic formulas.

The magnetic flux density B established within a material with the permeability μ by the magnetic field strength H is [32]

$$B = \mu H \tag{2.1}$$

The permeability μ is defined in terms of the permeability of air (μ_0), and a relative permeability μ_r

$$\mu = \mu_0 \mu_r \tag{2.2}$$

where $\mu_0 = 4\pi \times 10^{-7}$ and μ_r can be from 1.0 for air to several thousands for iron [33].

Equation (2.1) shows a linear relation between B and H if μ is constant. However, for materials used in electrical machine cores, permeability is not usually constant (see an example of this in Fig. 5.5).

Flux is a surface integral of the flux density [34],

$$\phi = \int B dA_s \tag{2.3}$$

where A_s is the cross sectional area.

Inductance describes a coil's ability to produce flux linkage ψ [34]. In [33], it is shown that for a simple magnetic structure shown in Fig. 2.1,

$$\phi = \frac{Ni}{\Re} \tag{2.4}$$

where the reluctance of a magnetic circuit $\Re$ is

$$\Re = \frac{l}{\mu A} \tag{2.5}$$
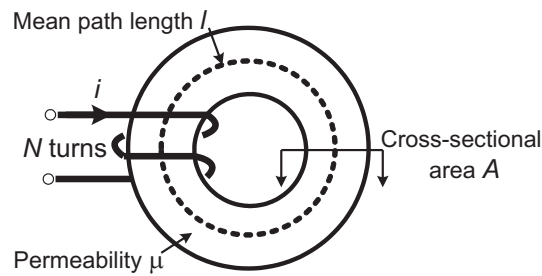
Figure 2.1: Magnetic reluctance [33].

It is also shown in [33] that a coil such as shown in Fig. 2.2 has a self-inductance L which is defined as

$$L = \frac{N\phi}{i} = \frac{\psi}{i} \tag{2.6}$$
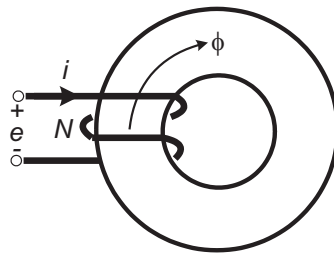
Figure 2.2: Self-inductance L [33].

By substituting (2.4) in (2.6),

$$L = \frac{N^2}{\Re} \tag{2.7}$$

According to [34] the magnetic energy is

$$W_\phi = \int_V \frac{1}{2}(B \cdot H)dV \tag{2.8}$$

where V is the volume of the magnetic field.

Assuming the permeability of the magnetic medium constant and substituting (2.1) in (2.8) the magnetic energy is

$$W_\phi = \int_V \frac{1}{2}\frac{B^2}{\mu}dV \tag{2.9}$$

The magnetic energy in the linear region (where *L* is constant) can also be calculated as

$$W_\phi = L \int_0^i i\,di = \frac{1}{2}Li^2 \tag{2.10}$$

From (2.9) and (2.10) we have:

$$\left.\begin{array}{l} W_\phi = \dfrac{1}{2\mu} \int_V B^2 dV \\[2ex] W_\phi = \dfrac{1}{2}Li^2 \end{array}\right\} \Rightarrow L = \frac{1}{\mu i^2} \int_V B^2 dV \tag{2.11}$$

The magnetomotive force for a coil, for instance as the one shown in Fig. 2.2 is

$$mmf = Ni \tag{2.12}$$

If Ni is substituted from (2.4) into (2.12), then

$$mmf = \phi \Re \tag{2.13}$$

Inserting (2.3) and (2.5) in (2.13), we get

$$mmf = \frac{B}{\mu}l = Hl \tag{2.14}$$

2.2 Permanent magnet synchronous machine (PMSM)

The Permanent Magnet Synchronous Machine is here considered to be a polyphase AC motor with rotor mounted permanent magnets and sinusoidal distribution of the stator phase windings as well as fed with sinusoidal currents (thus the brushless dc permanent magnet machine, BLDC, is not considered here).The permanent magnets provide the field excitation in the machine instead of the field windings.

By having the magnets on/in the rotor, the electrical losses of the machine are reduced and the absence of mechanical components such as slip rings and brushes make the machine lighter.

Compared to induction motors in which the stator current contains magnetizing as well as torque-producing components, the use of the permanent magnets in the rotor of permanent magnet machines makes it unnecessary to supply magnetizing current through the stator to obtain constant air-gap flux, so the stator current is mainly used to produce torque. Therefore, for the same output, the PMSM will operate at a higher power factor and it will be more efficient than the induction machine.

The PMSMs have a wide range of applications. E.g. the application of PM servo motors fed from static inverters is increasing [32]. The PMSM can be used in large power synchronous motors rated more than 1 MW. Large PMSMs can be used both in low speed drives as well as high speed drives.

2.2.1   Cons and pros of PMSM

The use of permanent magnets in construction of electrical machines brings the followings advantages:

- The magnetic field is provided by the permanent magnet and there is no need for additional DC supply for magnetization (excitation circuit). Therefore, without slip rings, and brushes the machine becomes robust and maintenance free.

- The efficiency of the PMSM in comparison with an Electrically Magnetized Synchronous Machine (EMSM) is higher since the rotor copper losses disappear as there is no rotor winding.

- Higher torque to weight ratio compared to other AC generators.

- Better dynamic performance than EMSM [32].

However, the PMSM has some disadvantages:

- At high temperature or at powerful magnetic fields inside a generator, the permanent magnets could be demagnetized (although this is rarely a problem today) [35].

- Difficulties for transportation and security in delivery as well as high cost of permanent magnet material.

2.2.2   Construction of PMSM

The magnets of the permanent magnet machines can be placed in different parts of the rotor. The most common rotor configurations of the permanent magnet synchronous machines which are shown in Fig. 2.3 are:

- Surface mounted magnet rotor (Fig. 2.3(a)).

- Interior mounted magnet rotor (Fig. 2.3(b)).

- Inset mounted magnet rotor (Fig. 2.3(c)).

Surface mounted permanent magnet synchronous machines can more easily have a lower torque ripple while interior and inset mounted permanent magnet synchronous machines on the other hand generate flux concentration in the rotor that can allow thinner or weaker magnets [5]. Interior and inset mounted permanent magnet synchronous machines have unequal direct and quadrature inductance which produces a reluctance torque in addition to the torque created by the magnets. Interior mounted permanent magnet machines more easily have robustness against magnet demagnetization. However, the vibration and noise production in surface mounted permanent magnet synchronous machines is less than in interior permanent magnet machines [36]. In this thesis the surface and interior mounted permanent magnet machine are both investigated.
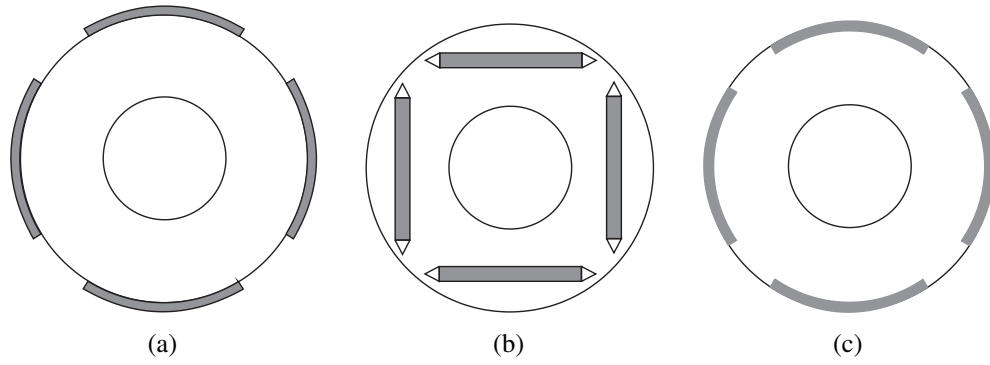
Figure 2.3: Rotor configurations for PMSM; (a) surface mounted magnet, (b) interior mounted magnet, (c) inset mounted magnet.

2.2.3 Dynamic model of PMSM

According to [37] the mathematical model of a PMSM in the dq synchronously rotating reference frame for assumed sinusoidal stator excitation is

$$u_{sd} = R_s i_{sd} + L_d \frac{i_{sd}}{dt} - \omega_{el} L_q i_{sq} \tag{2.15}$$

$$u_{sq} = R_s i_{sq} + L_q \frac{i_{sq}}{dt} + \omega_{el} L_d i_{sd} + \omega_{el} \Psi_m \tag{2.16}$$

$$T_e = \frac{3}{2} p [\Psi_m i_{sq} + (L_d - L_q) i_{sq} i_{sd}] \tag{2.17}$$

where u_{sd} and u_{sq} are d- and q-axis stator voltages, R_s is the resistance of the stator windings, L_d and L_q are d and q axis inductances, ω_{el} is the angular velocity of the rotor, i_{sd} and i_{sq} are d- and q-axis stator currents, Ψ_m is the permanent magnet flux linkage, T_e is the electromagnetic torque and p is the number of pole pairs.

Based on (2.15) and (2.16) the equivalent circuit of a PMSM can be obtained. see Fig. 2.4.
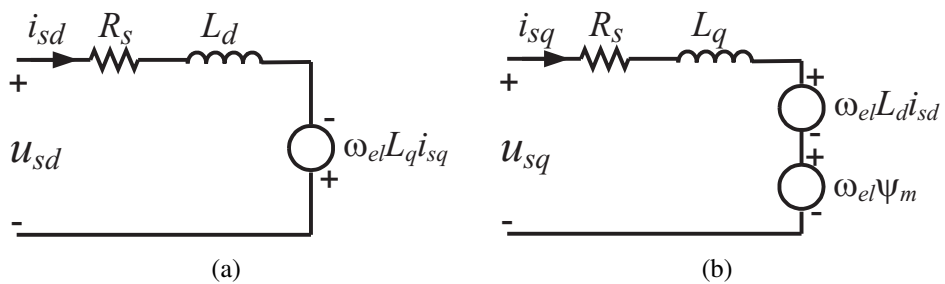
Figure 2.4: Equivalent circuit of a PMSM; (a) d-axis circuit, (b) q-axis circuit [37].

In steady state (2.15) and (2.16) become

$$u_{sd} = R_s i_{sd} - \omega_{el} L_q i_{sq} \tag{2.18}$$

$$u_{sq} = R_s i_{sq} + \omega_{el} L_d i_{sd} + \omega_{el} \Psi_m \tag{2.19}$$

2.2.4 Operation of PMSM

As can be seen in (2.17), in PMSMs the torque consists of two terms. The second term in surface mounted permanent magnet synchronous machines is zero, since there is no saliency; i.e. $L_d = L_q$.

In interior mounted permanent magnet synchronous machines, $L_q > L_d$, so to have both terms in the same direction, the stator current (i_s) should be in the second quadrant (Q_2) for the motoring mode and in the third quadrant (Q_3) for the generating mode.

For constant current using the phasor diagram given in Fig. 2.5 and noting that γ (the current phase angle) is measured from the q-axis in the positive (anticlockwise) direction in the phasor diagram, the d- and q-axis currents can be written

$$i_{sd} = -i_s \sin \gamma; \ i_{sq} = i_s \cos \gamma \tag{2.20}$$
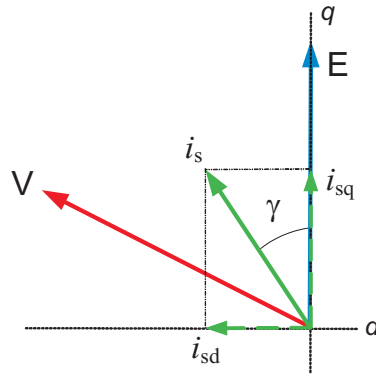
Figure 2.5: Phasor diagram for motoring mode.

By substituting (2.20) in (2.17), we get

$$T_e = \frac{3}{2} p \left[\psi_m i_s \cos \gamma - \frac{1}{2} i_s^2 (L_d - L_q) \sin 2\gamma \right] \tag{2.21}$$

All quantities in (2.21) are RMS values. By differentiating (2.21) with respect to γ, the value of γ which gives the maximum torque can be calculated. Therefore,

$$\gamma_{T\max} = \sin^{-1} \frac{1}{4} \left[\frac{\psi_m}{(L_d - L_q) i_s} + \sqrt{\left(\frac{\psi_m}{(L_d - L_q) i_s} \right)^2 + 8} \right] \tag{2.22}$$

Unfortunately, γ is not fixed. Saturation causes L_d and L_q to vary which complicates finding the optimum value of γ. If there is no saliency, then from (2.21) the current phase angle that maximizes the torque is $\gamma = 0$. This means that the stator current (i_s) will be oriented in the q-axis in phase with back-emf (E) [38] (see Fig. 2.5).

2.2.5   MTPA control strategy

There are several control strategies to improve the performance and reduce the losses of a PMSM [39]. The copper losses can be minimized by the Maximum Torque Per Ampere (MTPA) control strategy which consequently increases the efficiency [40]. For this control method there must be a sufficient voltage from the inverter to be able to have the current which is needed to obtain the desired torque. When the converter voltage is limited, there might be a need of more negative i_{sd} current to achieve the desired torque, since the voltage required to get MTPA is not sufficient from the converter. This is known as flux weakening. In [38], it is shown that the voltage limits are in the shape of ellipses in an id/iq-diagram and these ellipses shrink as the speed increases. The reason for this is that the back-emf is high at high speeds, and according to (2.18) and (2.19), there is less voltage available for achieving the initially desired current. Figure 2.6 shows the voltage limit ellipses for different speeds. The green curve represents the MTPA operating points. As can be seen, when the speed is low (blue voltage limit ellipse), the desired torque using MTPA is possible. However, as the speed increases (red and purple voltage limit ellipses) a more negative d current and also a higher current is needed to obtain the desired torque. In this thesis this type of control is used to control the generators. In the following sections this type of control for the SPMSG and IMPSG is described.
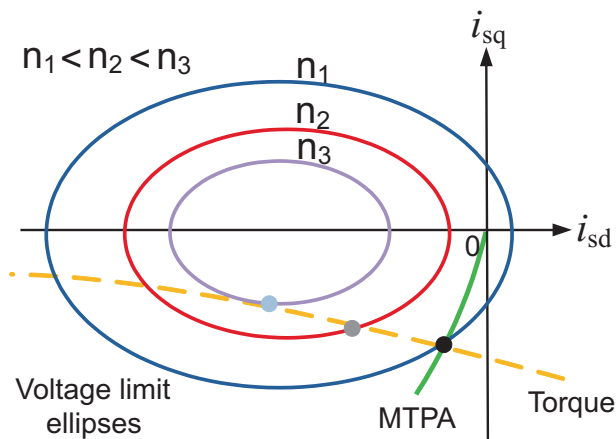

Figure 2.6: Voltage limits and MTPA curves for a generator.

2.2.5.1 MTPA operation of SPMSG

As was mentioned before, in SPMSGs the MTPA from (2.21) is attained with the current along the q-axis. It is shown in [38] that the voltage limit ellipse becomes a circle when $L_d = L_q$. As there is no saliency, from (2.17) it is obvious that the torque lines become parallel to the d-axis. The voltage limits circles and the MTPA line (green line) as well as the torque lines for a SPMSG is shown in Fig. 2.7.

From Fig. 2.7 it can be seen that as long as the speed is low and the current is low, there is no problem to operate the generator in MTPA to achieve the torques in Fig. 2.7. We are then following the green line. This means that if the voltage limit is the blue circle there is no problem to operate the generator at MTPA to get any torque (T_1, T_2 or T_3), since the MTPA line is inside this voltage limit.

As the speed increases the voltage limit circle shrinks. Then it is not possible to achieve a torque at MTPA operation if the desired torque is outside the voltage limit circle. E.g. if the voltage limit is the red circle, then we can achieve T_1 and T_2 at MTPA operation. However, it is not possible to achieve T_3. If the voltage limit is the purple circle, we can achieve T_1 at MTPA. However, to obtain T_2 we need to follow the black line. Now we use more current to obtain the required torque compared to the MTPA case.
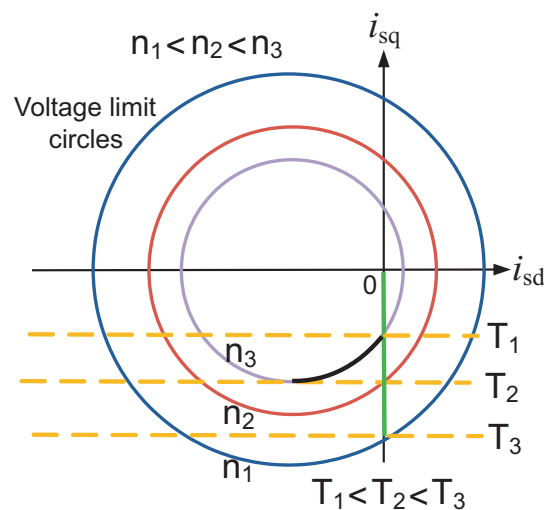
Figure 2.7: Voltage limits, MTPA and torques curves for a SPMSG.

2.2.5.2 MTPA operation of IPMSG

The voltage limits ellipses, the MTPA line (green line) and the torque lines for an IPMSG are shown in Fig. 2.8. From the figure it can be seen that when the speed is low and the voltage limit is the blue ellipse, all the torques in Fig. 2.8 are achievable using MTPA, since the MTPA line is inside this voltage limit. When speed increases and the voltage limit is the red ellipse, it is possible to achieve T_1 at MPTA operation. However, to achieve

T_2 and T_3 we need to follow the gray line. If the speed increases more and the voltage limit is the purple ellipse, to achieve T_1, T_2 and T_3 we need to follow the black line. Therefore, more current is needed to obtain the required torque compared to the MTPA case.
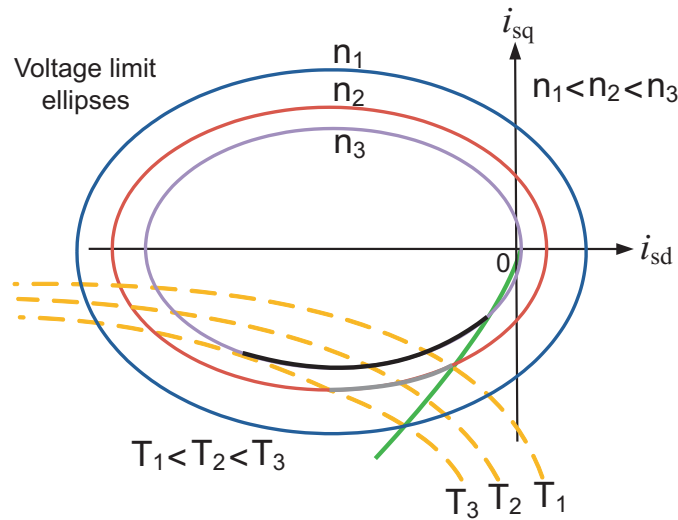
Figure 2.8: Voltage limits, MTPA and torques curves for an IPMSG.

2.3 Synchronous reluctance machine (SynRM)

The synchronous reluctance machine (SynRM) has a long history. The first SynRM was introduced by Kostko in 1923 [8]. The synchronous reluctance motor was developed particularly in the 1960's as a line-start synchronous AC motor [9]. During the 1990's, a substantial amount of work and research on the design and control of synchronous reluctance motors have been done [9], [10], [11], [12], [13], [14] and [15]. Recently, the SynRM have been even more improved [16], [17] and [18].

Even though most of the researchers have explored the application of the reluctance machine as a motor, the field of the synchronous reluctance generator (SynRG) has also been brought to attention [19], [20] and [21]. Several applications for synchronous reluctance machines are proposed in [22]. One of the interesting applications of the SynRG is for wind turbine generation systems [21], since SynRGs are robust, inexpensive and they have a simple rotor construction. Moreover, they have low noise emission and are suitable for variable speed operation. Although synchronous permanent magnet motors often are a very good choice for many variable-speed drive applications, the advantages of using synchronous reluctance motors is that, the today very expensive magnets are not needed.

2.3.1 Cons and pros of SynRM

The SynRM has the followings advantages:

- Simple rotor structure allowing inexpensive manufacturing.

- No rotor copper losses.

- Much lower torque ripple and low noise compared to switch reluctance machines [40].

- From control point of view, it can be an alternative to induction motors in many applications, such as in robotics, traction and low-cost drives [40].

- Suitable for super high speed applications in machine tools and molecular pumps [41].

- Lower temperature in machine windings, shaft and bearings compared to induction machines [16].

However, the SynRM has some disadvantages:

- Lower torque density and power factor compared to a PMSM.

- Needs a larger inverter compared to induction machines [16].

2.3.2 Rotor construction of SynRM

The saliency (the difference between L_d and L_q) in a SynRM can be created by using different shapes of insulation layers inside the rotor of a SynRM (see [16] and [42]). Fig. 2.9 shows the rotor that is used in this work. If the d- and q- axis is considered as it is shown in Fig. 2.9, the inductance in the d-axis will be greater than the inductance in the q-axis ($L_d > L_q$).
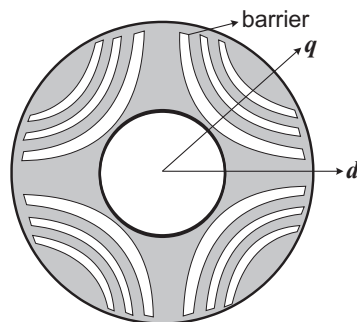

Figure 2.9: One type of rotor structure of a SynRM.

In general the performance of a SynRM improves as the saliency ratio (ξ)

$$\xi = \frac{L_d}{L_q} \tag{2.23}$$

increases [43]. Therefore, in designing a SynRM one objective should always be considered: The q-axis inductance must be decreased as much as possible. In [16], it is shown that the best shape for barriers is the same shape as the d-axis flux lines inside a solid rotor.

2.3.3 SynRM model and equivalent circuit

Equations (2.15), (2.16), (2.18) and (2.19) are also valid for the SynRM, with the remark that ψ_m is equal to zero in the SynRM. Based on (2.15) and (2.16), the equivalent circuit of a SynRM is shown in Fig. 2.10.
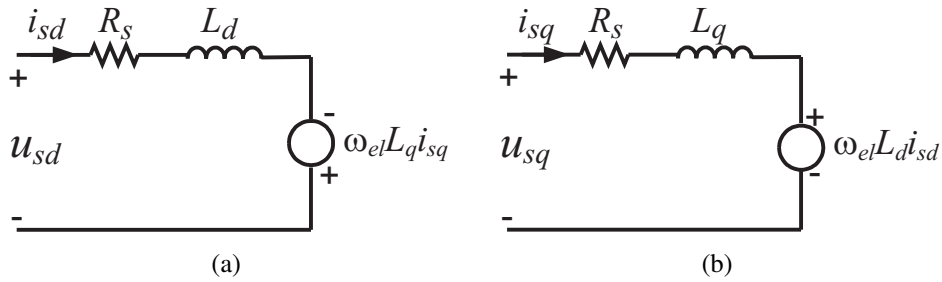
Figure 2.10: Equivalent circuit of a SynRM; (a) d-axis circuit, (b) q-axis circuit [41].

The SynRM torque relation has been derived and analyzed in [42] and [44]. The SynRM torque in the dq-coordinate system is

$$T = \frac{3}{2}p\left(L_d - L_q\right)I^2 \sin\left(2\theta\right) \tag{2.24}$$

where p is the number of pole pairs, L_d is the d-axis inductance, L_q is the q-axis inductance, I is the RMS value of the stator current and θ is the current angle (angle between d-axis and current).

In [43] it is shown that the power factor of a SynRM is related to the saliency ratio ξ by

$$\cos\varphi = (\xi - 1)\sqrt{\left[\frac{\sin 2\theta}{2\left(\tan\theta + \xi^2\cot\theta\right)}\right]} \tag{2.25}$$

2.3.4 Operation of SynRM

From (2.24), T as a function of θ for different currents can be plotted. This plot together with the MTPA line is shown in Fig. 2.11.
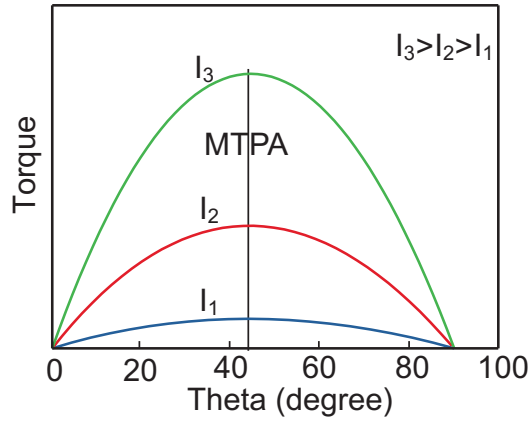
Figure 2.11: Operation diagram for SynRM [16].

As can be seen from Fig. 2.11 the maximum torque is achieved when $\theta = 45\,^\circ$. However, this is for linear (unsaturated) conditions. When the machine comes into saturation, the MTPA angle will be higher than $45\,^\circ$, see [16] and [43].

If $\theta = 45\,^\circ$, the power factor for different saliency ratios can be plotted from (2.25) which is shown in Fig. 2.12.
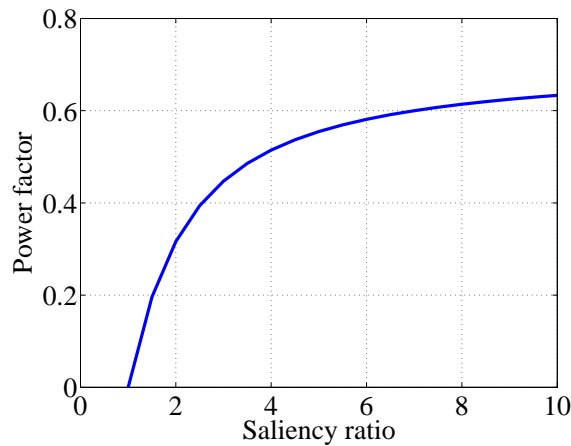
Figure 2.12: Power factor vs saliency ratio for $\theta = 45\,^\circ$ [43].

As can be seen from Fig. 2.12, when $\theta = 45\,^\circ$ a power factor of only 0.633 is achieved even with $\xi = 10$. However, according to [38] and [43] a synchronous reluctance motor can be operated at maximum power factor value of

$$\cos\varphi = \frac{\xi - 1}{\xi + 1} \tag{2.26}$$

with using the current phase angle

$$\theta = \tan^{-1}\sqrt{\xi} \tag{2.27}$$

In Fig. 2.13, the power factor versus different saliency ratios for $\theta = \tan^{-1} \sqrt{\xi}$ is plotted. As can be seen, the power factor at $\xi = 10$ has improved from 0.633 to 0.818.
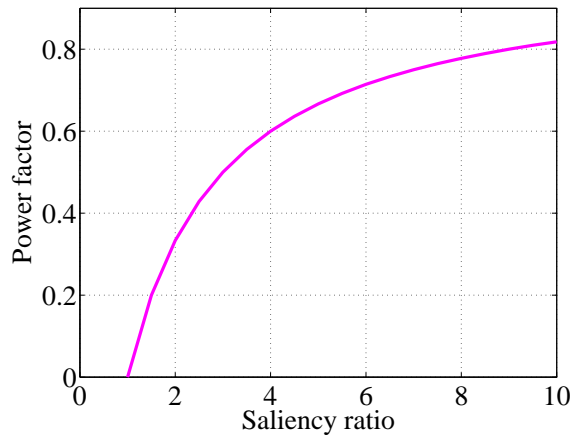
Figure 2.13: Power factor vs saliency ratio for $\theta = \tan^{-1} \sqrt{\xi}$ [43].

From Fig. 2.12 and Fig. 2.13, it is obvious that the power factor strongly depends on the operating point θ as well as the saliency ratio. In Fig. 2.14, the power factor versus current angle for different saliency ratio is plotted.
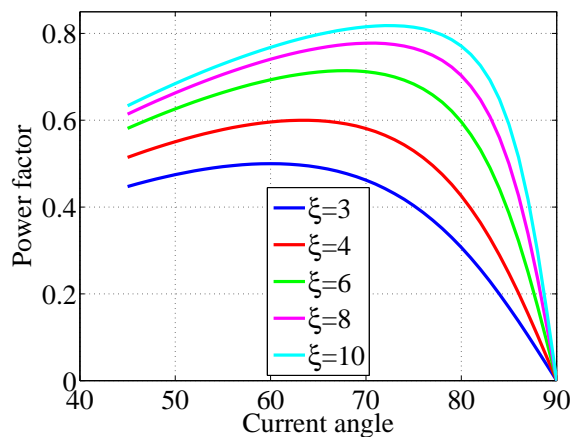
Figure 2.14: Power factor vs current angle with different saliency ratios.

There are other possible operation points for the SynRM, if a different control strategy is applied. However, since in this thesis the MTPA control strategy is used, they are not considered.

2.4 Machine loss calculation

In this work, the copper and iron losses are the considered electric machine losses. The mechanical losses such as friction and windage losses are neglected.

2.4.1 Copper loss

The copper losses are calculated according to

$$P_{cu} = 3R_s \left| I_s \right|^2 \tag{2.28}$$

where P_{cu} is the copper loss, R_s is the armature phase resistance and $\left| I_s \right|$ is the RMS magnitude value of the phase current.

2.4.2 Core loss

Core loss is mainly consisting of hysteresis loss and eddy current loss. Hysteresis loss is due to the materials unwillingness to change its magnetic state; the larger the area of the hysteresis loop, the larger the loss is. Hysteresis loss also depends on the frequency; the higher the frequency the more times the hysteresis loop is ran through, and the higher is the loss. Hysteresis loss can be reduced by annealing which means a heat-treatment of the material with high temperatures of $\approx 1000\,^\circ\mathrm{C}$ [45]. The hysteresis loss may be calculated with the formula

$$P_{hy} = K_{hy} f B^\alpha \ \mathrm{W/m}^3 \tag{2.29}$$

where k_{hy} and α are constants (α =1.6-2.4) which depend on the magnetic properties of the material.

In a similar way, the eddy current loss may be calculated with

$$P_{ec} = K_{ec} f B^2 \ \mathrm{W/m}^3 \tag{2.30}$$

where k_{ec} is a constant that depends on the magnetic properties of the material but it also varies with lamination thickness. Common values of lamination thickness are 0.35 to 0.65 mm [45], but thinner ones exist, like 0.27 mm and even 0.1 mm. For thicker laminations, the constant k_{ec} is higher and consequently, the eddy current loss is higher.

Core loss is independent of load and it is therefore also called no-load loss. Core loss is difficult to measure as it is difficult to separate core loss and mechanical loss. It is also difficult to calculate the core loss. Empirical formulas, like (2.29) and (2.30) can be used but then we have to know not only values of the constants but also values of the flux density and the frequency. The flux density may vary inside the core parts, and the frequency could also vary due to harmonics. So, often calculations of the core loss are very approximate. An alternative is to do FEM calculations in order to find proper values of *B* for each element, and then calculate the core loss for each element and frequency using either (2.29) and (2.30), or graphs from the manufacturer showing core loss per weight, as seen in Fig. 2.15.
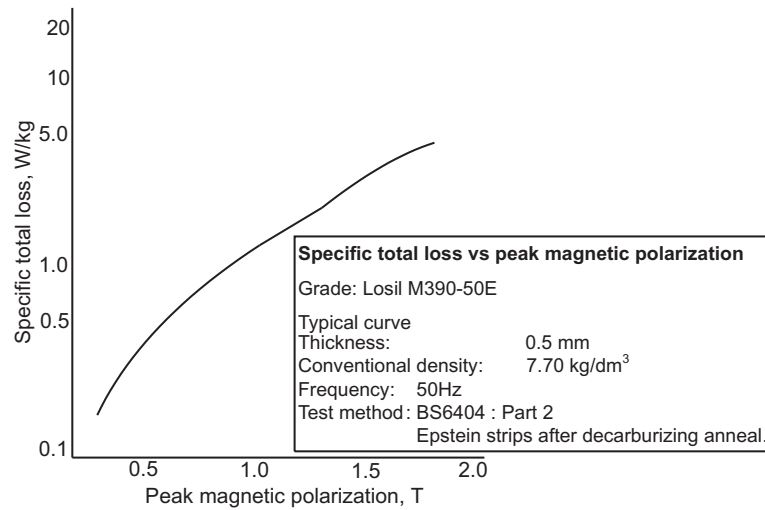
Figure 2.15: Loss curve showing core loss per weight for different flux densities at 50 Hz, for the material Losil M340-50E, where E stands for alloyed steel and the rest of the name implies that it has a guaranteed loss value of 3.4 W/kg at 1.5 T, and 50 Hz, being 0.5 mm thick [45].

This procedure will anyway give only an estimate of the core loss considering that electrical steels are tested and graded under pure sinusoidal conditions. These ideal conditions hardly represent the magnetising conditions in an electric machine. As the presence of flux harmonics increases the core losses of electrical steels, it is likely that the calculated loss will be lower than the actual core loss.

To calculate the core losses for different wind speeds, two methods are used in this work.

2.4.2.1 First method

This method is used when it is assumed that the machine works in the linear region. For this case the relation

$$P_{Fe} = k\omega_{el}^2 \tag{2.31}$$

is used, where P_{Fe} is the iron (core) loss, k is a constant extracted from the iron losses at rated speed from Maxwell. Further, ω_{el} is the electrical speed of the machine in *rad/s*.

2.4.2.2 Second method

To calculate the core losses considering the non-linear region of the machine, for each wind speed the core losses are taken from Maxwell. Information about how the core loss calculation is done in Maxwell can be found in [46].

2.5   Machine parameters calculation

2.5.1   Stator slot pitch and pole pitch

The stator slot pitch, τ_s, which is shown in Fig. 2.16 in meters is calculated as

$$\tau_s = \frac{\pi D_{ins}}{Q} \tag{2.32}$$

where D_{ins} is the inner stator diameter shown in Fig. 2.17 and Q is the number of slots.

The pole pitch, τ_p, which is expressed in meters is

$$\tau_p = \frac{\pi D_{otr}}{2p} \tag{2.33}$$

where D_{otr} is the outer rotor diameter (see Fig. 2.17).

The pole pitch for a surface mounted permanent magnet machine as well as an interior mounted permanent magnet machine is depicted in Fig. 2.16.

(a)   (b)
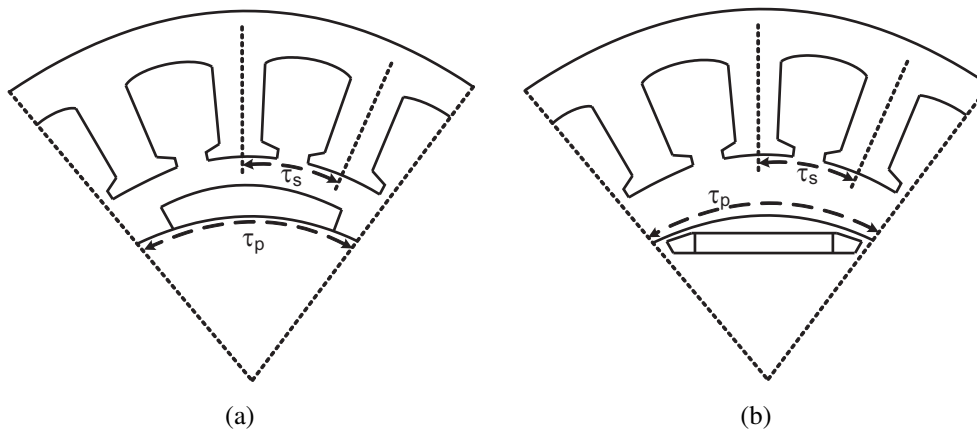
Figure 2.16: Stator slot pitch and pole pitch; (a) surface permanent magnet machine, (b) interior permanent magnet machine.
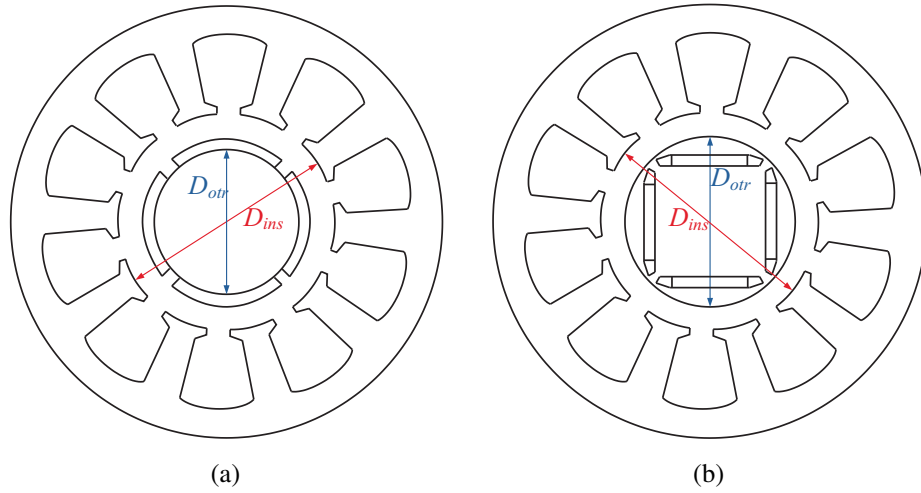
Figure 2.17: Inner stator diameter and outer rotor diameter; (a) surface permanent magnet machine, (b) interior permanent magnet machine.

2.5.2 Phase resistance

The resistance of a copper conductor can be calculated as

$$R = \rho \frac{l_{copper}}{A_{copper}} \tag{2.34}$$

where ρ is the copper resistivity which increases as the temperature increases and it is shown in Fig. 2.18, l_{copper} is the coil (conductor) length and A_{copper} is the copper area.
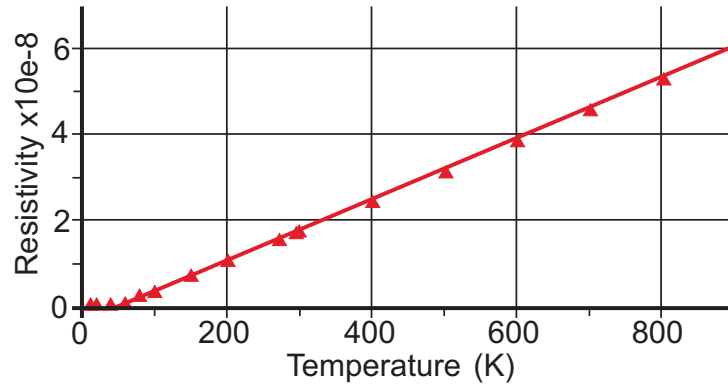
Figure 2.18: Resistivity of copper as a function of temperature.

In this work to calculate the phase resistance, l_{copper} in (2.34) the following expression is used

$$l_{copper} = 2 \left(L_{machine} + l_e \right) \frac{N_{coil}}{a} \frac{N_c}{a} \tag{2.35}$$

23

where $L_{machine}$ is the machine length, a is the number of parallel branches, N_{coil} is the number of coils, N_c is the number of conductors per slot per phase and l_e is the length of a single end winding.

In (2.35), N_{coil} is

$$N_{coil} = \frac{Q}{m} \tag{2.36}$$

where m is the number of phases and l_e in meters according to [32] is

$$l_e \approx (0.083p + 1.217)\frac{pD_{ins} + H_{tooth}}{2p} + 0.02 \tag{2.37}$$

where H_{tooth} is the height of the stator tooth as shown in Fig. 2.19. (D_{ins} can be found in Fig. 2.17).
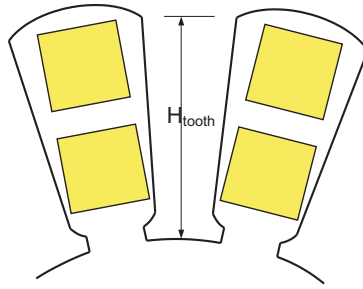
Figure 2.19: Stator tooth height.

2.5.3 Winding factor

The winding factor is [34]

$$k_{w\upsilon} = k_{p\upsilon}k_{d\upsilon}k_{sq\upsilon} = \sin\left(\upsilon\frac{y}{y_Q}\frac{\pi}{2}\right) \cdot \frac{2\sin\left(\frac{\upsilon}{m}\frac{\pi}{2}\right)}{\frac{Q}{mp}\sin\left(\upsilon\pi\frac{p}{Q}\right)} \cdot \frac{\sin\left(\upsilon\frac{s}{y_Q}\frac{\pi}{2}\right)}{\upsilon\frac{s}{y_Q}\frac{\pi}{2}} \tag{2.38}$$

where $k_{p\upsilon}$ is the pitch factor for the υth harmonic, $k_{d\upsilon}$ is the distribution factor for the υth harmonic and $k_{sq\upsilon}$ is the skew factor for the υth harmonic. y is the coil pitch expressed in the number of slots and y_Q is the pole pitch expressed by the number of slots per pole. That means

$$y_Q = \frac{Q}{2p} \tag{2.39}$$

For the first harmonic where υ=1 and if there is no skewing, i.e. the skew factor is one, the winding factor can be calculated as

$$k_w = k_p k_d \tag{2.40}$$

where

$$k_p = \sin\left(\frac{y}{y_Q}\frac{\pi}{2}\right) \tag{2.41}$$

and according to [34] k_d is

$$k_d = \frac{\sin\left(\dfrac{q\alpha_u}{2}\right)}{q\sin\left(\dfrac{\alpha_u}{2}\right)} \tag{2.42}$$

where α_u in electrical degrees is

$$\alpha_u = p\frac{2\pi}{Q} \tag{2.43}$$

and q is the number of slots per pole per phase

$$q = \frac{Q}{2pm} \tag{2.44}$$

2.5.4 Air-gap and Carter's factor

In an electrical machine the flux density in the air-gap always decreases at the slot opening. Therefore, it is not easy to define the average flux density in the air gap between the stator and the rotor. However, if considering the air-gap to be longer than the physical distance between the teeth bottom and the rotor surface (using Carter's coefficient [k_{Cs}]), the lower flux density in the slot opening can be accounted for. The modified length of the air-gap is

$$g' = k_{Cs}g \tag{2.45}$$

where g is the actual air-gap length and k_{Cs} is Carter's coefficient which is calculated according to

$$k_{Cs} = \frac{\tau_s}{\tau_s - b_e} \tag{2.46}$$

where τ_s is given in (2.32) and b_e is

$$b_e = kB_{s0} \tag{2.47}$$

where B_{s0} is the slot opening and k is calculated according to

$$k = \frac{\dfrac{B_{s0}}{g}}{5 + \dfrac{B_{s0}}{g}} \tag{2.48}$$

2.5.5 Slot fill factor

Slot fill factor is a measure of how much copper that is put into the stator slot [38]. For a double-layer winding, the following relation is obtained.

$$SF_g = \frac{2A_{coil}}{A_{slot}} \tag{2.49}$$

A_{coil} is the coil area and is shown in Fig. 2.20 and A_{slot} is the slot area and is shown in Fig. 2.21.
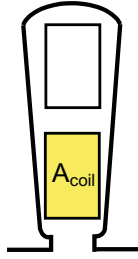
Figure 2.20: Coil area.
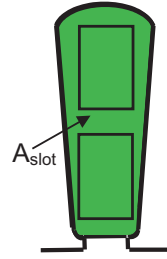
Figure 2.21: Slot area.

2.5.6 Current density and electric loading

The current density is

$$J = \frac{I_s N_c}{a A_{coil}} \tag{2.50}$$

where I_s is the RMS value of stator current.

According to [34] and [47] the electric loading (linear current density) is

$$A_c = \frac{2m N_s I_s}{\pi D_{air-gap}} \tag{2.51}$$

where N_s is the number of turns in series and $D_{air-gap}$ is the air-gap diameter which is shown in Fig. 2.22.

In (2.51), the number of series turns (N_s) is

$$N_s = \frac{N_{turns}}{a} \tag{2.52}$$

where

$$N_{turns} = N_{coil} \times N_c \tag{2.53}$$
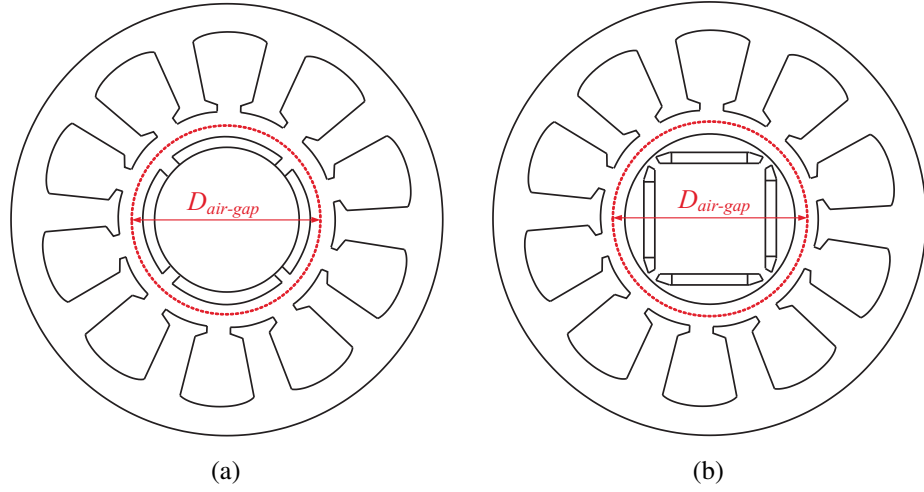
Figure 2.22: Air-gap diameter; (a) surface permanent magnet machine, (b) interior permanent magnet machine.

2.5.7 Magnetizing inductance

The direct-axis inductance of a synchronous machine consists of a direct-axis magnetizing inductance (L_{md}) and the leakage inductance ($L_{leakage}$)

$$L_d = L_{md} + L_{leakage} \tag{2.54}$$

In the same way, the quadrature-axis inductance of a synchronous machine consists of a quadrature-axis magnetizing inductance (L_{mq}) and also the leakage inductance ($L_{leakage}$)

$$L_q = L_{mq} + L_{leakage} \tag{2.55}$$

According to [34] the magnetizing inductance of the direct-axis of a *m*-phase machine can be calculated as

$$L_{md} = \frac{2m\mu_0 \left(k_w N_s\right)^2 \tau_p}{p\pi^2} \frac{L_{machine}}{g'} \tag{2.56}$$

where τ_p can be replaced by (2.33).

For a 3-phase surface mounted permanent magnet machine using (2.56) and (2.33) and considering the air-gap plus the magnet length, the magnetizing inductance can be calculated as

$$L_{md} = L_{mq} = \frac{3\mu_0 \left(k_w N_s\right)^2 D_{otr}}{\pi p^2} \frac{L_{machine}}{g' + \dfrac{l_m}{\mu_r}} \tag{2.57}$$

In [38], it is shown that for a 3-phase interior mounted permanent magnet machine the d- and q-axis magnetizing inductances are

27

$$L_{md} = \Gamma_d \frac{3\mu_0 \left(k_\omega N_s\right)^2 D_{otr}}{\pi p^2} \frac{L_{machine}}{g'}$$
$$L_{mq} = \Gamma_q \frac{3\mu_0 \left(k_\omega N_s\right)^2 D_{otr}}{\pi p^2} \frac{L_{machine}}{g'}$$

(2.58)

where

$$\Gamma_d = \frac{g'}{g_{effd}}$$

(2.59)

and

$$\Gamma_q = \frac{g'}{g_{effq}}$$

(2.60)

In (2.59), g_{effd} is the effective air-gap in the d-axis including the effects of the magnet and the saliency and can be calculated according to

$$g_{effd} = \frac{g'}{k_{1ad} - \dfrac{k_1 k_{\alpha d}}{1 + P_m R_g}}$$

(2.61)

where R_g is the reluctance of the air-gap between θ_1 and θ_2 which is shown in Fig. 2.23 and can be calculated according to (2.62) where the value of $\theta_2 - \theta_1$ should be in radian.
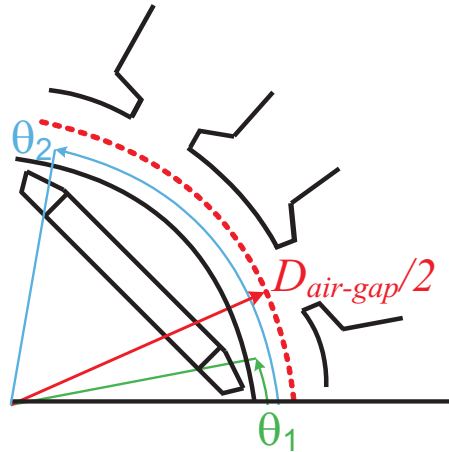

Figure 2.23: Calculation of L_d and L_q [38].

$$R_g = \frac{g'}{\mu_0 \dfrac{D_{air-gap}}{2} \left(\theta_2 - \theta_1\right) L_{machine}}$$

(2.62)

P_m is the magnet permeance and is

$$P_m = \mu_0 \mu_r \frac{Magnet\ width \times L_{machine}}{Magnet\ thickness}$$

(2.63)

Magnet width and magnet thickness are shown in Fig. 2.24.
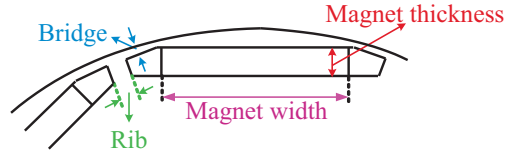
Figure 2.24: IPMSG magnet parameters.

In [38], it is shown that k_1, $k_{\alpha d}$ and k_{1ad} in (2.61) are calculated according to

$$k_1 = \frac{4}{\pi} \sin \frac{(\theta_2 - \theta_1) p}{2} \tag{2.64}$$

$$k_{\alpha d} = \frac{\sin \dfrac{(\theta_2 - \theta_1) p}{2}}{\dfrac{(\theta_2 - \theta_1) p}{2}} \tag{2.65}$$

$$k_{1ad} = \frac{(\theta_2 - \theta_1) p}{\pi} + \frac{\sin [(\theta_2 - \theta_1) p]}{\pi} \tag{2.66}$$

In (2.60), g_{effq} is the effective air-gap in the q-axis and can be calculated according to

$$g_{effq} = \frac{g'}{k_{1aq}} \tag{2.67}$$

where k_{1aq} is

$$k_{1aq} = \frac{(\theta_2 - \theta_1) p}{\pi} - \frac{\sin [(\theta_2 - \theta_1) p]}{\pi} \tag{2.68}$$

In [38], it is shown that the rib length between the magnet (is shown in Fig. 2.24) can increase the value of L_{mq}. The increase of L_{mq} can be calculated according to

$$\Upsilon = \frac{p \sin^{-1} \left(\dfrac{rib}{\dfrac{D_{otr}}{2}} \right)}{180} \tag{2.69}$$

In (2.69), $\sin^{-1} \left(\frac{rib}{\frac{D_{otr}}{2}} \right)$ should be in degrees.

$$k_\Upsilon = \Upsilon + \frac{\sin (\Upsilon \pi)}{\pi} \tag{2.70}$$

$$k_{1aq-withrib} = k_{1aq} + k_\Upsilon \tag{2.71}$$

$$L_{mq-withrib} = \frac{k_{1aq-withrib}}{k_{1aq}} L_{mq} \tag{2.72}$$

where L_{mq} is calculated from (2.58).

2.5.8 Leakage inductance

The leakage inductance can be divided into different leakage inductances which are [34]:

- Slot leakage inductance

- Tooth tip leakage inductance.

- End winding leakage inductance.

- Air-gap leakage inductance.

- Skew leakage inductance.

However, the most dominant inductances are slot and tooth tip leakage inductances.

2.5.8.1 Slot leakage inductance

In this part the calculation of slot leakage for a double-layer full and short pitch winding is presented based on [34].

If we assume a slot with double-layer windings like the one shown in Fig. 2.25, then one of the slot leakage fluxes is the grey line which is shown in Fig. 2.25.
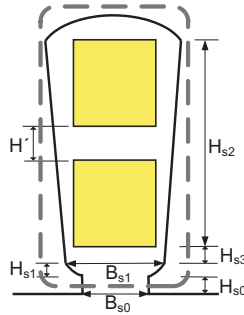
Figure 2.25: Stator slot leakage flux at the slot opening.

If N_3 is the number of conductors in one slot and B (flux density) is constant in the height H_{S0}, then according to (2.5) and (2.7) we have

$$
\left.
\begin{aligned}
L_{slot-leakage1} &= \frac{N_3^2}{\Re_1} \\
\Re_1 &= \frac{B_{s0}}{\mu_0 H_{s0} L_{machine}}
\end{aligned}
\right\}
\Rightarrow L_{slot-leakage1} = \frac{N_3^2 \mu_0 H_{s0} L_{machine}}{B_{s0}}
\tag{2.73}
$$

In (2.73), $L_{slot-leakage1}$ is the slot leakage inductance resulting from the flux leakage shown in Fig. 2.25.

Another slot leakage flux is the blue line which is shown in Fig. 2.26. Flux density, B, is also constant throughout the height H_{S3}. The slot leakage inductance in this area ($L_{slot-leakage2}$) is calculated according to
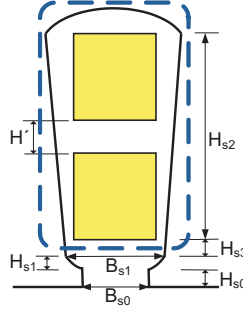
Figure 2.26: Stator slot leakage flux at height H_{S3}.

$$\left.\begin{array}{l} L_{slot-leakage2} = \dfrac{N_3^2}{\Re_2} \\[2em] \Re_2 = \dfrac{B_{s1}}{\mu_0 H_{s3} L_{machine}} \end{array}\right\} \Rightarrow L_{slot-leakage2} = \dfrac{N_3^2 \mu_0 H_{s3} L_{machine}}{B_{s1}} \tag{2.74}$$

We also need to consider the flux leakage inside the slot from the bottom to the top of the slot. However, the leakage between the layers (H′) will not be considered. In this area, the flux is not constant, since the encircled current changes with height (Fig. 2.27).
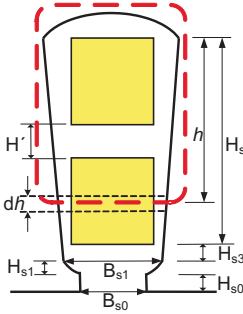
Figure 2.27: Stator slot leakage flux from bottom to the top of the slot.

If the number of turns at height h is assumed to be N_h, then N_h is

$$N_h = \frac{N_3 h}{H_{s2} - H'} \tag{2.75}$$

Using (2.12) the *mmf* at height h is

$$mmf_h = N_h i = \frac{N_3 h}{H_{s2} - H'} i \tag{2.76}$$

31

where i is the current flowing in the conductors.

From (2.14) mmf_h can also be written as

$$mmf_h = H(h)B_{s1} \tag{2.77}$$

Therefore

$$\left.\begin{array}{l} \text{mmf}_h = H(h)B_{s1} \\ \text{mmf}_h = \dfrac{N_3 h}{H_{s2} - H'}i \end{array}\right\} \Rightarrow H(h) = \dfrac{\dfrac{N_3 h}{H_{s2} - H'}i}{B_{s1}} \Rightarrow H(h) = \dfrac{N_3 h i}{(H_{s2} - H')B_{s1}} \tag{2.78}$$

According to (2.1), we also have

$$B\left(h\right) = \mu_0 H\left(h\right) = \mu_0 \frac{N_3 h}{\left(H_{s2} - H'\right)B_{s1}}i \tag{2.79}$$

In the slot the volume of magnetic field is

$$dV = B_{s1}L_{machine}dh \tag{2.80}$$

According to (2.11), (2.79), and (2.80)

$$\left.\begin{array}{l} dV = B_{s1}L_{machine}dh \\ L_{slot-leakage3} = \dfrac{1}{\mu_0 i^2}\displaystyle\int_V (B\left(h\right))^2 dV \end{array}\right\} \Rightarrow$$

$$L_{slot-leakage3} = \frac{B_{s1}L_{machine}}{\mu_0 i^2}\int_0^{H_{s2}-H'} \mu_0^2 \frac{N_3^2 i^2}{(H_{s2}-H')^2 B_{s1}^2}h^2 dh$$

$$\Rightarrow L_{slot-leakage3} = \frac{\mu_0 B_{s1}L_{machine}N_3^2}{(H_{s2}-H')^2 B_{s1}^2}\left(\frac{1}{3}(H_{s2}-H')^3\right) = \frac{\mu_0 L_{machine}N_3^2(H_{s2}-H')}{3B_{s1}} \tag{2.81}$$

For a more complicated slot where H_{s1} is not zero, in addition to the three slot leakage inductances that we had before we will also have leakage flux according to the green path as shown in Fig. 2.28.
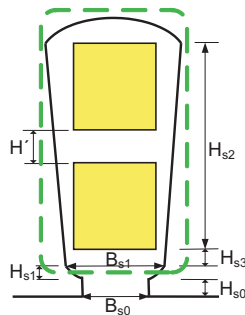

Figure 2.28: Stator slot leakage flux at height H_{S1}

This inductance according to [34] is

$$L_{slot-leakage4} = N_3^2 \mu_0 L_{machine} \frac{H_{s1}}{B_{s1} - B_{s0}} \ln \frac{B_{s1}}{B_{s0}} \tag{2.82}$$

For a double-layer full pitch winding the inductance caused by the leakage flux according to the orange path shown in Fig. 2.29 is $L_{slot-leakage5}$.
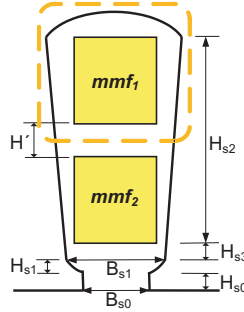
Figure 2.29: Stator slot leakage flux between the two layers.

The total magnetomotive force in the slot can be calculated as

$$\left.\begin{array}{l} mmf_1 + mmf_2 = mmf_{total} \\ mmf_{total} = N_3 i \\ mmf_1 = mmf_2 \end{array}\right\} \Rightarrow mmf_1 = \frac{N_3 i}{2} \tag{2.83}$$

We have

$$\left.\begin{array}{l} mmf_1 = H(h)B_{s1} \\ mmf_1 = \dfrac{N_3 i}{2} \end{array}\right\} \Rightarrow H(h) = \frac{\dfrac{N_3 i}{2}}{B_{s1}} \Rightarrow H(h) = \frac{N_3 i}{2B_{s1}} \tag{2.84}$$

The volume of magnetic field is

$$\left.\begin{array}{l} dV = B_{s1}L_{machine}dH \\ L_{slot-leakage5} = \dfrac{1}{\mu_0 i^2} \displaystyle\int_V B^2 dV \end{array}\right\} \Rightarrow L_{slot-leakage5} = \frac{B_{s1}L_{machine}}{\mu_0 i^2} \int_0^{H'} \mu_0^2 \frac{N_3^2 i^2}{4B_{s1}^2} dH$$

$$\Rightarrow L_{slot-leakage5} = \frac{\mu_0 B_{s1}L_{machine}N_3^2}{4B_{s1}^2}(H') = \frac{\mu_0 L_{machine}N_3^2 H'}{4B_{s1}} \tag{2.85}$$

So the 5 different inductances are calculated according to the equations below

$$L_{slot-leakage5} = N_3^2 \mu_0 L_{machine} \frac{H'}{4B_{s1}} \tag{2.86}$$

$$L_{slot-leakage4} = N_3^2 \mu_0 L_{machine} \frac{H_{s1}}{B_{s1} - B_{s0}} \ln \frac{B_{s1}}{B_{s0}} \tag{2.87}$$

$$L_{slot-leakage3} = N_3^2 \mu_0 L_{machine} \frac{H_{s2} - H'}{3B_{s1}} \qquad (2.88)$$

$$L_{slot-leakage2} = N_3^2 \mu_0 L_{machine} \frac{H_{s3}}{B_{s1}} \qquad (2.89)$$

$$L_{slot-leakage1} = N_3^2 \mu_0 L_{machine} \frac{H_{s0}}{B_{s0}} \qquad (2.90)$$

The total slot leakage inductance is calculated according to

$$L_{slot-leakageTotal} = \frac{Q}{am} \frac{1}{a} L_{slot-leakage} \qquad (2.91)$$

Figure 2.30 shows the total slot leakage inductance.
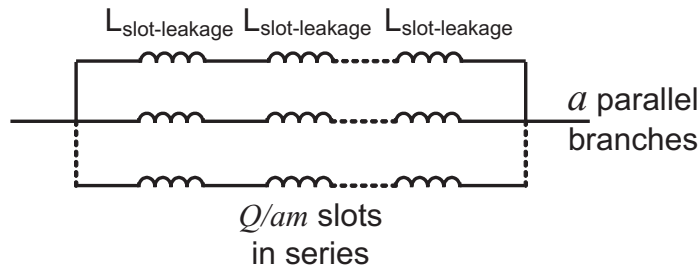
Figure 2.30: Total inductance [34].

$L_{slot-leakage}$ is the sum of (2.86) to (2.90)

$$
\begin{aligned}
L_{slot-leakage} &= L_{slot1} + L_{slot2} + L_{slot3} + L_{slot4} + L_{slot5} = \\
N_3^2 \mu_0 L_{machine} &\left(\frac{H_{s0}}{B_{s0}} + \frac{H_{s3}}{B_{s1}} + \frac{H_{s2} - H'}{3B_{s1}} + \frac{H_{s1}}{B_{s1} - B_{s0}} \ln \frac{B_{s1}}{B_{s0}} + \frac{H'}{4B_{s1}} \right) \\
\Gamma_{double-full} &= \frac{H_{s0}}{B_{s0}} + \frac{H_{s3}}{B_{s1}} + \frac{H_{s2} - H'}{3B_{s1}} + \frac{H_{s1}}{B_{s1} - B_{s0}} \ln \frac{B_{s1}}{B_{s0}} + \frac{H'}{4B_{s1}}
\end{aligned}
\qquad (2.92)
$$

So the total slot leakage inductance is calculated according to

$$
\begin{aligned}
L_{slot-leakageTotal\_full} &= \frac{Q}{am} \frac{1}{a} L_{slot-leakage} \\
&= \frac{Q}{m} \left(\frac{N_3}{a} \right)^2 \mu_0 L_{machine} \left(\frac{H_{s0}}{B_{s0}} + \frac{H_{s3}}{B_{s1}} + \frac{H_{s2} - H'}{3B_{s1}} + \frac{H_{s1}}{B_{s1} - B_{s0}} \ln \frac{B_{s1}}{B_{s0}} + \frac{H'}{4B_{s1}} \right) \\
L_{slot-leakageTotal\_full} &= \frac{Q}{m} \left(\frac{N_3}{a} \right)^2 \mu_0 L_{machine} \Gamma_{double-full}
\end{aligned}
$$
$$(2.93)$$

For a short pitch double-layer winding according to [34]

$$L_{slot-leakage} = N_3^2 \mu_0 L_{machine} \Gamma_{double-short}$$
$$\Gamma_{double-short} = k_1 \frac{H_{s2} - H'}{3B_{s1}} + k_2 \left(\frac{H_{s0}}{B_{s0}} + \frac{H_{s3}}{B_{s1}} + \frac{H_{s1}}{B_{s1} - B_{s0}} \ln \frac{B_{s1}}{B_{s0}} \right) + \frac{H'}{4B_{s1}}$$

(2.94)

$$L_{slot-leakageTotal\_short} = \frac{Q}{m} \left(\frac{N_3}{a} \right)^2 \mu_0 L_{machine} \Gamma_{double-short}$$

(2.95)

For a three phase winding the coefficients k_1 and k_2 are calculated according to [34] as

$$k_1 = 1 - \frac{9}{16}\varepsilon$$

(2.96)

$$k_2 = 1 - \frac{3}{4}\varepsilon$$

(2.97)

where ε is:

$$\varepsilon = 1 - \frac{y}{\tau_p}$$

(2.98)

2.5.8.2 Tooth tip leakage inductance

The tooth tip leakage flux is shown in Fig. 2.31.
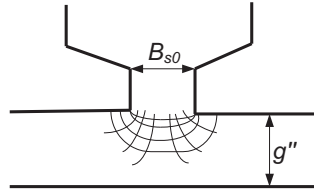
Figure 2.31: Tooth tip flux path

The tooth tip leakage inductance according to [34] is calculated as shown below

$$L_{tooth-tip} = \frac{Q}{m} \left(\frac{N_3}{a} \right)^2 \mu_0 L_{machine} \Gamma_{tooth-tip}$$
$$\Gamma_{tooth-tip} = k_2 \frac{5 \left(\dfrac{g''}{B_{s0}} \right)}{5 + 4 \left(\dfrac{g''}{B_{s0}} \right)}$$

(2.99)

where for a surface mounted permanent magnet machine, g'' is

$$g'' = physical\_airgap + \frac{magnet\_thickness}{\mu_r}$$

(2.100)

2.5.8.3 End winding inductance

End winding inductance is difficult to calculate accurately [38]. Luckily this inductance is quite small. To calculate the end winding inductance, two methods are used in this work.

First method

According to [32] the end winding inductance is

$$L_{end} = \frac{Q}{m} \left(\frac{N_3}{a} \right)^2 q\mu_0 l_e \Gamma_{end} \tag{2.101}$$

The length of a single end winding l_e can be calculated from (2.37) and the specific permeance of the end winding Γ_{end} for a double-layer winding is [32]

$$\Gamma_{end} \approx 0.3 \tag{2.102}$$

Second method

According to [34] the end winding inductance is

$$L_{end} = \frac{Q}{m} \left(\frac{N_3}{a} \right)^2 q\mu_0 l_w \lambda_w \tag{2.103}$$

The average length l_w of the end winding and the product $l_w \lambda_w$ can be written in the form

$$\begin{aligned} l_w &= 2l_{ew} + W_{ew} \\ l_w \lambda_w &= 2l_{ew}\lambda_{1ew} + W_{ew}\lambda_w \end{aligned} \tag{2.104}$$

where l_{ew} is the axial length of the end winding measured from the end of the stack, and W_{ew} is the coil span according to Fig. 2.32. λ_{1ew} and λ_w are the corresponding permeance factors. These factors for a synchronous machine are taken from [34] and given in Table 2.1.
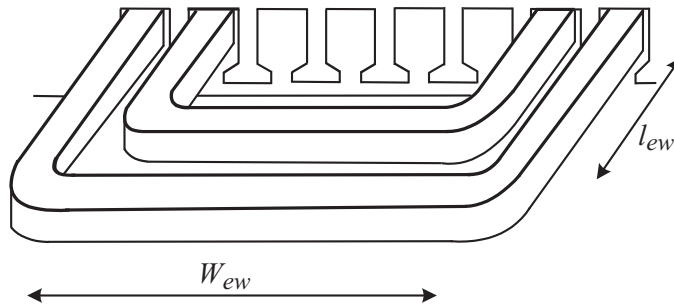

Figure 2.32: Dimensions of an end winding [34].

Table 2.1: Permeance factors of the end windings of a synchronous machine [34]

Cross-section of end winding	Nonsalient-pole machie		Salient-pole machine	
	λ_{1ew}	λ_w	λ_{1ew}	λ_w
	0.342	0.413	0.297	0.232
	0.380	0.130	0.324	0.215
	0.371	0.166	0.324	0.243
	0.493	0.074	0.440	0.170
	0.571	0.073	0.477	0.187
	0.605	0.028	0.518	0.138

The first three rows in Table 2.1 are accurate for 3-plane windings of different layout, and the last three options for different layouts of 2-plane windings. (A 2-plane winding means that an arbitrary radius of the machine may intersect not more than two phases.) Which option to choose, regarding the cross-sections given, is not clear from [34] but it is assumed in this work that the winding shown in Fig. 2.32, as well as the winding shown in Fig. 2.33 is represented by the cross-section picture looking like a lying F (row 4 in Table 2.1).

According to [34], the permeance factors depend on several things, like the number of planes, the number of phases, the winding type, the rotor type and the end winding length over pole-pitch ratio.
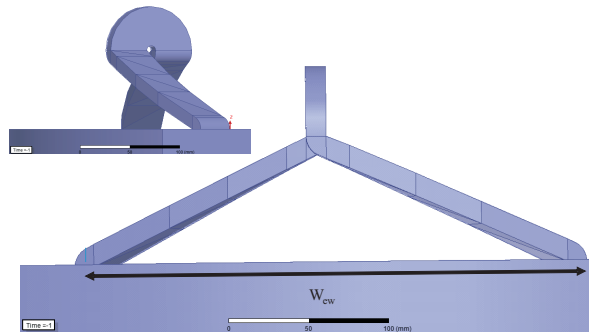
Figure 2.33: End winding shape.

Chapter 3

Power electronic theory

In this section two power semiconductor switches, diode and IGBT, are described. The active and passive rectifier and their loss calculations are presented.

3.1 Power semiconductor switches

3.1.1 Diode

A diode is a semiconductor made of Silicon, Germanium, Silicon Carbide or Selenium. The circuit symbol of the diode is shown in Fig. 3.1. The important property of a diode is its directional conduction which means that it conducts electric current in one direction, from anode (A) to cathode (K). When the anode is positively charged relative to the cathode and an applied voltage over the diode is greater than a definite forward threshold voltage, the diode starts to conduct and the current flows from anode to cathode. If the diode is reversed biased or the voltage across the diode is less than forward threshold voltage, then the diode blocks the current. The ideal and the actual i-v characteristic of a diode can be found in [33]. The idealized characteristics can be used for analyzing the system. However, for calculation of losses, the actual voltage-current relation should be considered.
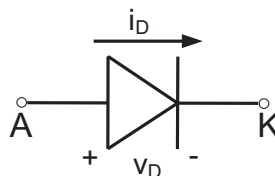
Figure 3.1: Diode symbol.

3.1.2 IGBT

The IGBT (Insulated Gate Bipolar Transistor) is a three-terminal power semiconductor switch which can be used to control the flow of electrical energy. It has fast switching (turn-on and turn-off times on the order of 1 μs [33], or even a bit lower) and a high efficiency. IGBTs are often not put in to the power electronic converters as discrete components, instead they are typically put into modules, which also comprise the needed free-wheeling diodes. In Fig. 3.2 the circuit symbol of the IGBT is shown.
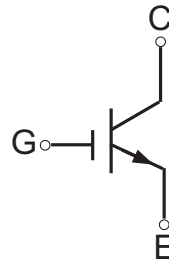
Figure 3.2: IGBT symbol.

The main advantages of the IGBT according to [33] are:

- It has a high impedance gate, which only needs a small amount of energy to switch this device.

- It has a small on-state (conduction) voltage even in devices with large blocking voltage ratings.

3.2 Active rectifier

Three-phase controlled rectifiers have a wide range of applications, from small rectifiers to large HVDC transmission systems. They are used for many kinds of motor drives, traction equipment, controlled power supplies and many other applications [48]. One type of these rectifiers is the force-commutated (switching) pulse width modulated (PWM). PWM rectifiers are built with semiconductors with gate-turn-off capability. This allows full control of the converter, because the valves can be switched ON and OFF whenever it is required. Active rectifiers belong to this type of rectifiers.

The force-commutated three-phase rectifiers are used in two ways: (a) as a current source rectifier, where power reversal is done by dc voltage reversal and (b) as a voltage source rectifier, where power reversal is done by current reversal at the dc link. In this thesis the voltage source three-phase rectifier is used which is the most utilized rectifier [48]. Figure 3.3 shows the topology of this type of rectifier.
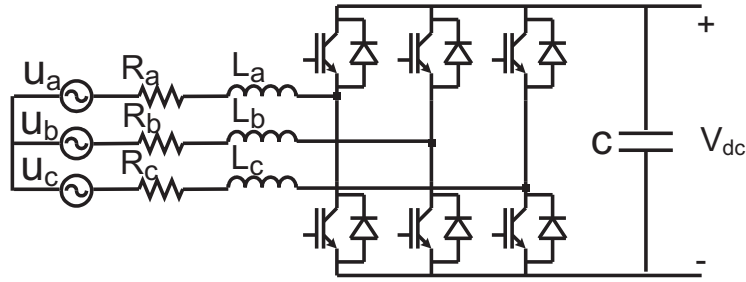
Figure 3.3: A voltage source three-phase active rectifier topology.

This type of rectifier uses actively controlled switches such as IGBTs in order to rectify the voltage. Typically they have 6 IGBTs and diodes, a so called two-level converter, and are PWM modulated, with a PWM frequency of 2-20 kHz, the higher for lower power levels. A more thorough description of the operation of a voltage source three-phase active rectifier with IGBTs can be found in [48].

In a two-level converter with a PWM control strategy, three voltage references are typically coming from the current regulator. These references are compared to a triangular wave (carrier wave) which has the PWM frequency (switching frequency) which is shown in Fig. 3.4. If the reference voltages are higher than the carrier wave, the upper side switch in that leg is turned on, otherwise the lower side switch is turned on.
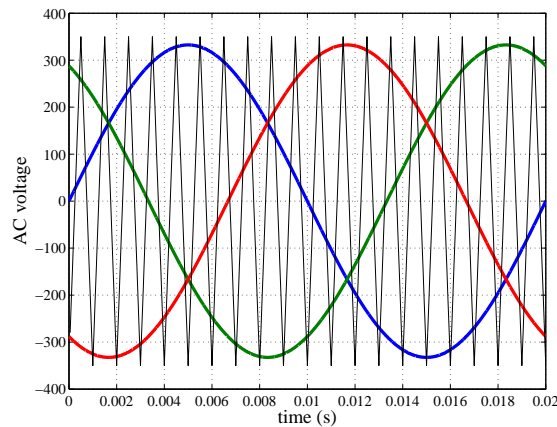
Figure 3.4: Voltage reference waveforms using no zero-sequence addition and carrier wave form.

The dc-link voltage in Fig. 3.3 is then related to the ac voltages as

$$V_{dc} = \frac{2U_a}{M} \tag{3.1}$$

where U_a is the peak phase voltage of the generator and M is the modulation index which is usually maximized to

$$M \leq 0.95 \tag{3.2}$$

which is a margin to guarantee controllability of the current, to provide a minimum on and off time of the modules, and to account for the blanking time and the losses in the converter.

If zero sequences are added to the voltage references, for the same peak phase generator voltage, the dc-link voltage will be 15% lower compared to the PWM control strategy. However, this is not considered in this work.

3.2.1 Active rectifier loss calculation

The by far most dominant losses in an active rectifier with IGBTs, in its steady-state operation, are conduction and switching losses. The other losses such as gate driver losses, auxiliary circuit losses, capacitor losses and snubber losses are not considered in this work. Therefore, they are not represented here as well.

3.2.1.1 IGBT loss calculation

The conduction and switching losses of the IGBTs in this work are calculated according to [49] as

$$P_{cond\_IGBT} = \left(\frac{1}{2\pi} + \left(\frac{M \cos \varphi}{8} \right) \right) V_{CE0} . \hat{I}_1 + \left(\frac{1}{8} + \left(\frac{M \cos \varphi}{3\pi} \right) \right) r_{CE} . \hat{I}_1^2 \tag{3.3}$$

$$P_{sw\_IGBT} = f_{sw} E_{sw\_IGBT} \left(\frac{1}{\pi} . \frac{\hat{I}_1}{I_{ref}} \right)^{K_i} . \left(\frac{V_{cc}}{V_{ref}} \right)^{K_v} \tag{3.4}$$

$$E_{sw\_IGBT} = E_{sw\_IGBT\_On} + E_{sw\_IGBT\_Off} \tag{3.5}$$

In (3.3), P_{cond_IGBT} is the conduction losses in the IGBT. The semiconductor resistive value, r_{CE} can be taken from the IGBT module data sheet. M is the modulation index, $\cos\varphi$ is the power factor and $\hat{I}_1$ is the peak value of the IGBT module current which is calculated according to

$$\hat{I}_1 = \frac{|I_s|}{n_{parallel}} \tag{3.6}$$

where $|I_s|$ is the magnitude of the stator current and $n_{parallel}$ (the number of parallel modules to fulfil the needed current) is calculated according to

$$n_{parallel} = \frac{Max \left(|I_{s,RMS}| \right)}{I_{rated,RMS}} \tag{3.7}$$

In (3.7), $Max(|I_{s,RMS}|)$ is the maximum stator current magnitude in RMS and $I_{rated,RMS}$ can typically be set equal to half the rated current value of the IGBT module. V_{CE0} is the voltage of the IGBT when the current is very low.

P_{sw_IGBT} in (3.4) is the switching losses for the IGBT. f_{sw} is the switching frequency, I_{ref} is the rated current value of the IGBT module for which the switching loss values are given in the data sheet, V_{ref} is the module reference voltage (voltage level for which the switching losses are given in the data sheet) and E_{sw_IGBT} is the switching energy loss for the transistor at I_{ref} and V_{ref}. V_{cc} is the voltage per module. K_i and K_v are scaling parameters. For the IGBT K_i is 1 and K_v is 1.35 according to [49].

3.2.1.2 Diode loss calculation

Also for diodes the most dominant losses are conduction and switching losses. Here, these diode losses are calculated according to [49].

$$P_{cond\_D} = \left(\frac{1}{2\pi} - \left(\frac{M\cos\varphi}{8} \right) \right) V_{F0}.\hat{I}_1 + \left(\frac{1}{8} - \left(\frac{M\cos\varphi}{3\pi} \right) \right) r_F.\hat{I}_1^2 \qquad (3.8)$$

$$P_{sw\_D} = f_{sw} E_{sw\_D} \left(\frac{1}{\pi}.\frac{\hat{I}_1}{I_{ref}} \right)^{K_i} . \left(\frac{V_{cc}}{V_{ref}} \right)^{K_v} \qquad (3.9)$$

In (3.8), P_{cond_D} is the conduction losses in the diode. The scaling parameters, K_i and K_v, for the diode are 0.6 according to [49]. The resistive value, r_F can be taken from the IGBT module data sheet.

P_{sw_D} in (3.9) is the switching losses for the diode. I_{ref} and V_{ref} are respectively the rated current value and the reference voltage of the IGBT module for which the switching loss values are given in the data sheet and E_{sw_D} is the switching energy loss for the diode at I_{ref} and V_{ref}.

3.3 Passive rectifier

The first conversion of AC output voltage of a generator to a DC voltage could be the duty of a diode rectifier. This kind of rectifier is inexpensive and robust. If a rectifier is made with only diodes, it is called diode rectifier or passive rectifier, since there is no active control of the power semiconductors. A diode rectifier can be an interesting option where power can flow from AC side to DC side [33]. When a diode rectifier is used, a dc-dc converter such as a full bridge converter is needed to control the dc-link voltage.

3.3.1 Three-phase diode rectifier

The topology of a three-phase diode rectifier is shown in Fig. 3.5.
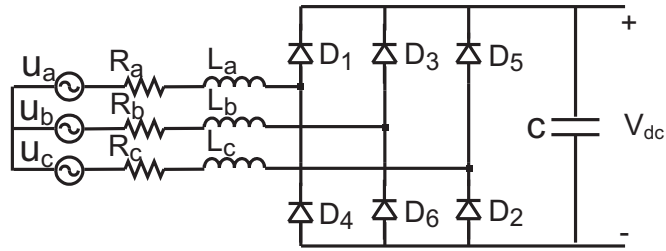
Figure 3.5: A three-phase diode rectifier topology.

3.3.2 Passive rectifier loss calculation

Diode losses consist of both conduction and switching losses. However, in a passive rectifier the conduction losses are dominant and the switching losses can then be neglected; due to the natural commutation and the fact that the commutations occur at low frequency. The conduction losses can be calculated as

$$P_{cond\_diode}(t) = v_D(t)i_D(t) \tag{3.10}$$

where v_D is the forward voltage and it can be found in the data sheet of the diode in a graph as a function of the diode current i_D.

Chapter 4

Wind turbine theory

To study the behavior of a wind turbine, basic knowledge of wind turbine power, energy and wind turbine types is necessary. Therefore, in this chapter the formulas for calculating the power of the wind, wind turbine mechanical power and annual energy capture of the wind turbine are given. The type of the wind turbine which is going to be used in this thesis is discussed. Different transmission lines are represented.

4.1   Wind turbine operation

4.1.1   Wind speed distribution

If the wind speed is considered as a continuous random variable, then the probability of a specific wind speed can be described with a probability density function. One way to approximate the probability density of wind speeds is by the Weibull distribution, which is formulated as

$$f\left(\omega\right) = \left(\frac{k}{c}\right)\left(\frac{\omega}{c}\right)^{k-1}\exp\left[-\left(\frac{\omega}{c}\right)^{k}\right] \tag{4.1}$$

where $f\left(\omega\right)$ is the probability density, k is the shape factor which varies a little, but it can be considered to be 2 for normal sites [50], ω is the wind speed and c is the scale factor which is calculated according to

$$c = \frac{\bar{\omega}}{\Gamma\left(1 + \dfrac{1}{k}\right)} \tag{4.2}$$

In (4.2), $\bar{\omega}$ is the average wind speed and it can be calculated as

$$\bar{\omega} = \int\limits_{0}^{\infty} \omega f\left(\omega\right)d\omega \tag{4.3}$$

and Γ is Euler's gamma function which is expressed as

$$\Gamma(x) = \int_0^\infty t^{x-1} e^{-t} dt \tag{4.4}$$

4.1.2 Power performance

The kinetic energy (E_k) of a parcel of air of mass m, flowing at wind speed ω as it is explained in [51] is

$$E_k = \frac{1}{2} m \omega^2 \tag{4.5}$$

If ρ is the air density, the thickness of the parcel is x and A is the cross-section area as it is shown in Fig. 4.1, then (4.5) can be rewritten as

$$E_k = \frac{1}{2} \rho A x \omega^2 \tag{4.6}$$
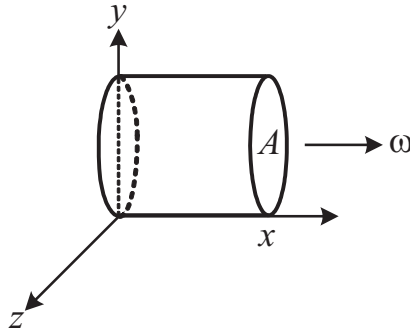
Figure 4.1: Packet of air moving with speed ω.

In Fig. 4.1, if side x is moving with speed ω and the opposite side is fixed at the origin, the mass is increasing uniformly. Therefore, the kinetic energy will also increase uniformly with x.

The power in the wind, P_ω, is the derivative of kinetic energy in (4.6) with respect to time,

$$P_\omega = \frac{dE_k}{dt} = \frac{1}{2} \rho A \omega^2 \frac{dx}{dt} = \frac{1}{2} \rho A \omega^3 \tag{4.7}$$

In a wind turbine the blades (rotor) convert the kinetic energy of wind into rotational mechanical energy. The mechanical power extracted from the wind power by a wind turbine is expressed as

$$P_m = C_p P_\omega = \frac{1}{2} C_p \rho A \omega^3 \tag{4.8}$$

where A is the rotor swept area and C_p is called coefficient of performance and is not a constant value.

A wind turbine has a maximum power which is called the rated power (P_{rated}). The rated power is achieved at a wind speed that is called rated wind speed (ω_{rated}). The value of C_p is kept at its largest possible value up to the rated wind speed, or slightly below the rated wind speed for some turbines, in order to convert the maximum power possible from the wind power. Then C_p is reduced while P_ω continues to increase with wind speed, in order to maintain the output power at its rated value as it is shown in Fig. 4.2. More information regarding how C_p varies can be found in [51]. As can be seen in Fig. 4.2, for low wind speeds (usually below 3-4 m/s), the mechanical power is insufficient to overcome the friction and make the blades rotate. Hence, for low wind speeds the turbine is shut down.
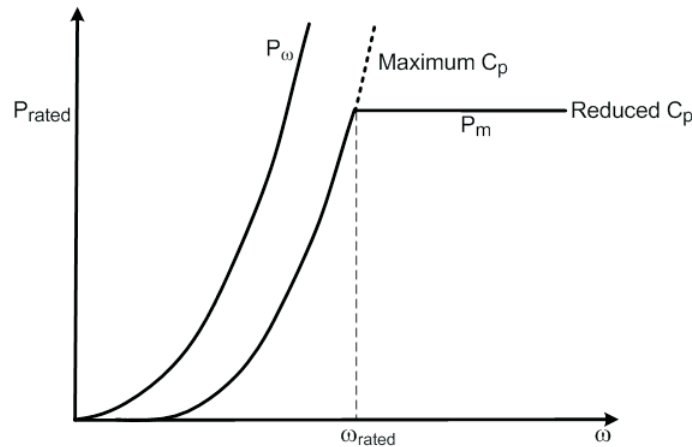

Figure 4.2: Wind and mechanical power of a typical variable speed wind turbine [51].

4.1.3 Energy capture calculation

The total amount of energy that a wind turbine produces is very important, since it gives the total income. Therefore, the energy collected from the wind over a period of time needs to be calculated. If this energy is calculated for a period of one year, it is called annual energy capture. For this purpose, the power and the probability density ($f(\omega)$) can be used. The amount of energy a wind turbine produces at a given average wind speed is

$$E_{\bar{\omega}} = T \int P(\omega) f(\omega) \, d\omega \qquad (4.9)$$

where T is the number of hours per year. If we need to calculate the annual energy losses (E_{loss}), then $P(\omega)$ will be the losses as a function of the wind speed. The losses can be any kind of loss, such as generator losses, converter losses, gearbox losses or the total losses. Depending on what we are looking for, the type of loss can be selected. To calculate the mechanical annual energy (E_{mec}), the mechanical power of the turbine, P_m from (4.8), is used as $P(\omega)$ in (4.9).

The annual energy efficiency of a wind turbine for a specific average wind speed, *E* in percentage, can then be calculated using

$$E = \left(1 - \frac{E_{loss}}{E_{mec}}\right) 100 \tag{4.10}$$

As mentioned before, *E* is the annual energy efficiency for a specific average wind speed.

4.2 Variable speed full power converter wind turbines

Wind turbine technology can be classified into different types. A detailed overview of different types of wind turbines and their comparisons can be found in [52]. The perhaps most common type in the future when it comes to large turbines is the variable speed wind turbine with a full-scale power converter. A schematic view of this type of wind turbine is depicted in Fig. 4.3. In this thesis a generating system based on this concept of wind turbines, specially adapted for a dc output voltage, is considered.

One advantage of a variable speed full power converter wind turbine shown in Fig. 4.3 is that different generator types such as an induction generator or a synchronous generator can be used. Another advantage is that it gives us the opportunity to choose a wide range of speeds for the generator. One choice is to remove the gearbox and connect the turbine rotor directly to a low speed generator which has a high number of poles and a large diameter. This type of wind turbines are known as direct-drive or directly driven. Another choice is to utilize a multi-stage gearbox, in the same way as in the fixed speed and many variable speed with partial power converter wind turbines, in order to reduce the generator's volume. The third choice is to use a single-stage gearbox that increases the speed of the turbine rotor by a factor of roughly 10 [52] yielding a low speed generator. This concept which is known as the Multibrid, has drawn substantial attention. That is simply because it has some advantages of higher speed generators such as smaller size compared to direct-drive and it has a smaller gearbox than the multi-stage gearbox wind turbine.
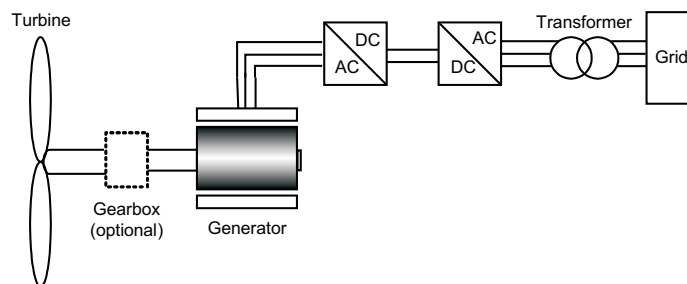

Figure 4.3: Wind turbine with full power converter with an AC transmission line.

4.3   HVDC off-shore wind turbines

In large off-shore wind farms, the transmission of huge power over long distances is a challenging task. High Voltage Alternating Current (HVAC) and High Voltage Direct Current (HVDC) are two choices for connections and power transmission in these wind turbines. HVAC connection is an economic solution for wind farms up to a few hundred MW with transmission distance shorter than 50-75 km [1]. A wind turbine with AC transmission lines is depicted in Fig. 4.3. However, for a wind farm size greater than 350 MW, if the distance to the shore becomes very long, approximately 100 km, HVDC transmission offers some advantages compared to HVAC [2], such as lower losses and low voltage drop in the transmission, no charging current in the cable, fast decoupled control of active and reactive power because of the dc-link [53]. Moreover a benefit is that a dc-supplied off-shore installation is isolated from main-land disturbances, and vice versa [2]. Figure 4.4 shows a schematic view of a wind turbine with DC transmission lines.
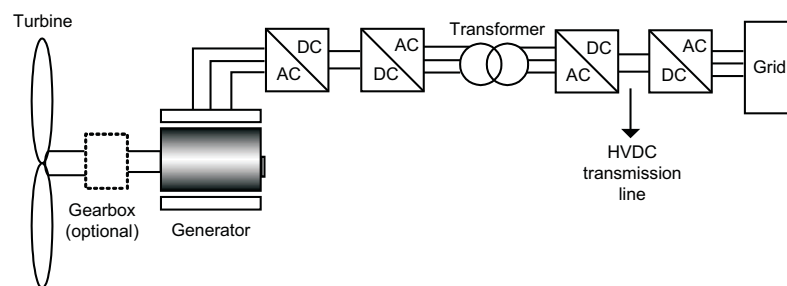

Figure 4.4: Wind turbine with full power converter with HVDC transmission line.

Chapter 5

Wind generator system design

In this Chapter the design of a surface mounted permanent magnet synchronous generator, an interior mounted permanent magnet synchronous generator as well as a synchronous reluctance generator is presented. To decrease the nearly high torque ripple of the IPMSG and SynRG, two methods for the IPMSG and one solution for SynRG are presented and the results are compared. A gearbox to increase the rotor speed suitable for the generators' speed is considered. The generators have 3 phases.

5.1   Speed selection

The value of the rotor speed in relation to the power is determined from an existing large wind turbine investigated in a previous project [54]. Figure 5.1 and 5.2 show power and rotor speed versus wind speed for the 2 MW wind turbine in [54]. The power of this turbine is scaled up to get a 5 MW wind turbine, with the same rated wind speed which is 12 m/s. The power of the generator versus wind speed and the rotor speed as a function of wind speed related to the 5 MW wind turbine are shown in Fig. 5.3 and Fig. 5.4. As can be seen in Fig. 5.4 the turbine speed at rated wind speed is 14.8 rpm. The gearbox ratio is assumed to be 50.67 and accordingly the generator speed becomes 750 rpm. It should be mentioned that the rotor speed of a 5 MW wind turbine turns slower than a 2 MW wind turbine, since the rotor diameter is bigger. However, as the gearbox losses are not considered in this thesis, we can still consider the generator speed of 750 rpm and in such a case just change the gearbox ratio. Thus, the turbine rotor speed versus wind speed of this 5 MW wind turbine is assumed to be the same as the turbine rotor speed of the 2 MW wind turbine.
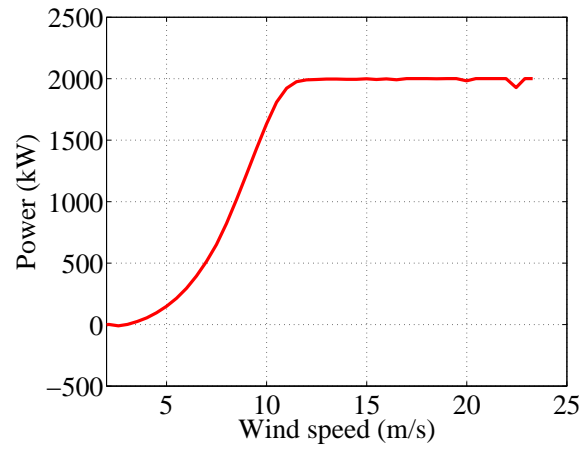
Figure 5.1: Electric power versus wind speed for the 2 MW turbine [54].
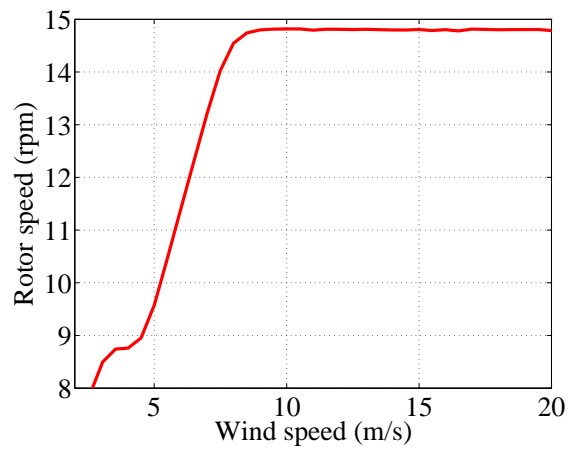

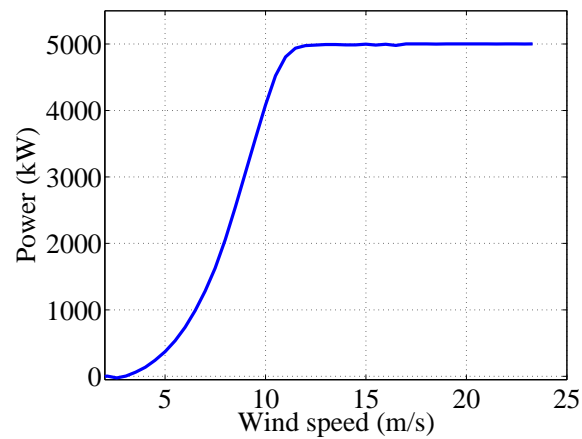Figure 5.2: Rotor speed versus wind speed for the 2 MW turbine [54].

Figure 5.3: Power versus wind speed for the investigated wind turbine system.
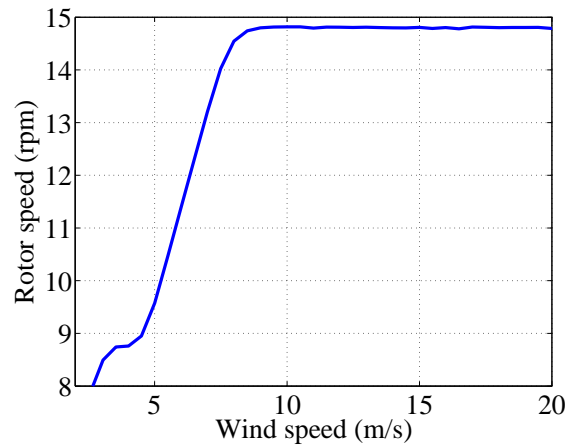
Figure 5.4: Rotor speed versus wind speed for the investigated wind turbine system.

5.2 FEM modelling

The Finite Element Method (FEM) is a numerical analysis for solving problems which are described by partial differential equations. FEM uses a complex system of points called nodes which makes a grid called a mesh. The finer the mesh is, the more accurate results can be achieved. This method is more accurate than analytical methods when it comes to electrical machines. There are generally two types of FEM modeling, two-dimensional (2D) and three-dimensional (3D). 3D model gives more accurate results considering end windings and leakage flux in the axial direction, while 2D is faster and saves time.

The software used to model the generators in this thesis is Ansys RMxprt and Ansys Maxwell.

Rotational Machine Expert (RMXprt) is a template-based design tool which speeds up the design and optimization of rotating electrical machines. With already existing templates for specific machines and by using classical analytical machine theory and equivalent magnetic circuit methods, RMxprt can calculate machine performance, which makes it possible to derive a suitable design in a short time before making a FEM model.

Maxwell is an electromagnetic field simulation software that uses FEM to solve static, frequency-domain, and time-varying electromagnetic and electric fields. Maxwell offers both 2D and 3D models. In this thesis for the sake of saving time a Maxwell 2D model is used. Moreover, according to [55] it seems to be fairly accurate to use a 2D model and introduce the end winding inductance on phase inductance to account for the 3D end effects.

5.3 Design of a 5 MW surface mounted permanent magnet synchronous generator

In this section a surface mounted permanent magnet synchronous generator (SPMSG) with a 2 or 3 stage gearbox for a 5 MW wind turbine is designed. The main aspect in this design is how to design a machine with low weight and cost, but with higher efficiency. This can be done by varying several parameters. The number of poles and slots, size of the machine and slots, the material of the stator and magnets etc.

5.3.1 Stator, rotor and permanent magnet material

The stator material properties affects the iron losses of the machine. Here, the material that is chosen for the generator stator and rotor is M235−35A (0.35 mm thickness) which is a non-linear material and chosen from the Maxwell library. This material is a laminated steel with the stacking factor of 0.95. The thinner the steel laminations are, the lower the iron losses will be and the higher the stacking factor. However, the cost for a thin lamination will be higher compared to, for example, lamination with a thickness of 0.5 mm. The B-H curve of this material is shown in Fig. 5.5. Stator and rotor material data and material loss curves versus different frequencies are given in Table 5.1 and Fig. 5.6.
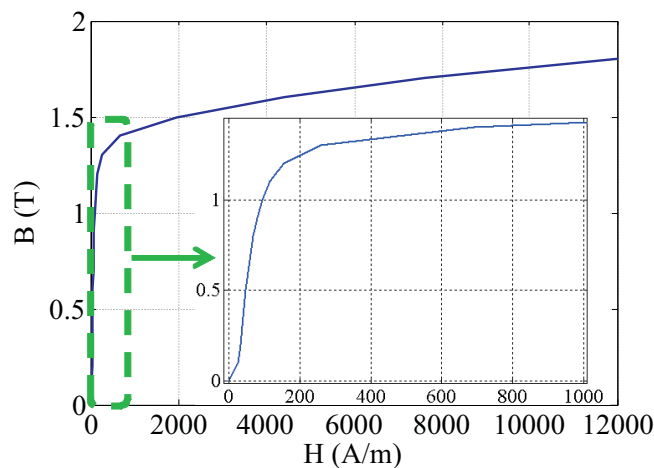

Figure 5.5: B-H curve of the stator and rotor material.

Table 5.1: Stator and rotor material characteristics

Parameter	Value
Mass density	7700 kg/m^3
Conductivity	2.5 MS/m
Core loss coefficients:	
Hysteresis loss coefficient	221.12
Eddy current loss coefficient	0.32
Excess loss coefficient	0
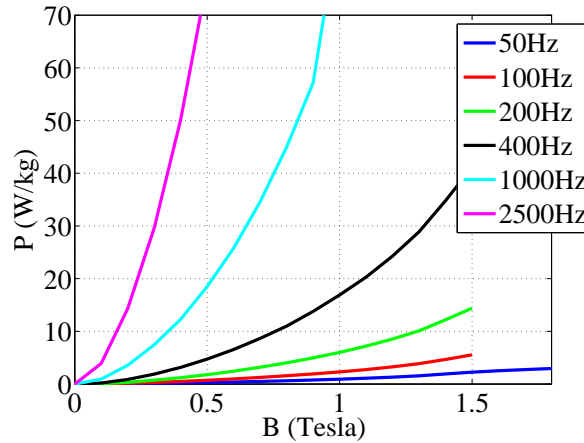
Figure 5.6: Steel loss curves at different frequencies.

The permanent magnet material used in high-performance electrical machines is most often a type of rare-earth magnet called Neodymium Iron Boron (NdFeB). This material can give the highest energy product and is thus one of the most powerful type of permanent magnets made. Therefore, for the permanent magnets of the SPMSG this material is used. The data of the used permanent magnet material is shown in Table 5.2.

Table 5.2: Permanent magnet material data

Parameter	Value
Mass density	7550 kg/m^3
Conductivity	625 kS/m
Relative permeability	1.044
Coercive force	838 kA/m

According to the data in Table 5.2, the remanence of the magnet material can then be calculated as

$$B_r = \mu_0 \mu_r H_c \tag{5.1}$$

where μ_0 is the permeability of air which is $4\pi \times 10^{-7}$, μ_r is the relative permeability of the material and H_c is the coercive force. Therefore, the remanence of the selected magnet material is 1.1 T. However, the remanence of some Neodymium magnets can be higher.

5.3.2 Number of poles and frequency

According to [56], by increasing the number of poles, the thickness of the stator yoke can be reduced and therefore the usage of stator core material for the yoke can also be reduced. More power output or torque can be achieved by using more poles for the same frame due to the reduction of yoke thickness. Since the operating frequency increases proportionally to the number of poles in order to achieve the desired speed, both eddy current loss and hysteresis loss increase despite the fact that the mass of the stator core material is reduced. Increasing the number of poles also makes the end windings shorter which leads to less copper losses. Here an eight pole machine is selected.

After defining the number of poles and speed of the machine, the frequency of the machine can be calculated according to

$$f = \frac{np}{60} \tag{5.2}$$

where n is the rotor speed in rpm and p is the number of pole pairs.

As was explained in Section 5.1, the generator speed is considered to be 750 rpm. Therefore the frequency of the machine is 50 Hz.

5.3.3 Air-gap length

The air-gap length influences the characteristics of an electrical machine significantly. In permanent magnet synchronous machines, the air-gap length is determined by mechanical constrains. In [34] it is shown that this value is similar to those values encountered in induction machines and if the number of pole pairs is greater than 1 ($p > 1$), the air-gap length in mm can be calculated as:

$$g = 0.18 + 0.006P^{0.4} \tag{5.3}$$

where P is the power of machine in Watts. According to (5.3), the air-gap length for this machine can be selected to be 3 mm. However, according to [57] if the magnets are originally glued on the rotor surface they may fly away from the surface. One way to avoid this problem is to bond the magnets with a cylindrical sleeve made of high-strength alloy as shown in Fig. 5.7. Therefore the air-gap length is considered to be 5 mm.
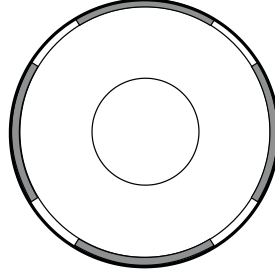
Figure 5.7: Rotor with surface mounted magnets and sleeve ring [57].

5.3.4 Machine dimensions

The initial dimensions for designing the machine are estimated according to

$$S = CD_{ins}^2 L_{machine} n_{syn} \tag{5.4}$$

where S is the apparent power, D_{ins} is the inner stator diameter, $L_{machine}$ is the machine length, C and n_{syn} are calculated using the equations below

$$C = \frac{\pi^2}{\sqrt{2}} k_w A_c \hat{B}_g \tag{5.5}$$

where C is called the machine constant, k_w is the winding factor which depends on the winding arrangement, A_c is the RMS value of the electric loading (linear current density) and $\hat{B}_g$ is the peak value of the flux density in the air-gap.

In (5.4), n_{syn} is calculated according to

$$n_{syn} = \frac{f}{p} \tag{5.6}$$

where f is the frequency of the machine. Equations (5.4)-(5.6) can be found in [34] in which a range of proper values for A_c and $\hat{B}_g$ for different machines are given. After using some suitable values for A_c and $\hat{B}_g$ based on [34] and assuming k_w=1 and $\frac{L_{machine}}{D_{ins}} \approx 1$ (according to [38]), the initial values for the machine dimensions were selected. This machine was designed in order to keep reasonable flux density and current density levels at 5 MW, as well as obtaining low losses using the RMxprt and Maxwell software. The final machine size values are shown in Table 5.3.

Table 5.3: Machine size

Parameter	Value
Outer stator diameter	1100 mm
Inner stator diameter	758 mm
Outer rotor diameter	748 mm
Inner rotor diameter	400 mm
Stator and rotor length	945 mm

5.3.5 Number of slots

Due to the large size of the stator, the number of slots are considered to be 72 in order to reduce the amplitude of the cogging torque [58]. The stator slot size values are shown in Table 5.4. This type of slot can be used for circular cross-section wires as well as rectangular wires.

Table 5.4: Stator slot size of the SPMSG

Parameter	Value
Hs0	6 mm
Hs1	2 mm
Hs2	90 mm
Bs0	10.4 mm
Bs1	16 mm
Bs2	24 mm
Rs	12 mm
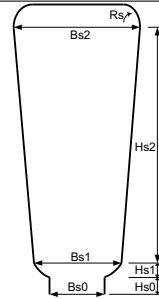
5.3.6 Magnet shape, width and coverage

Curved magnets with the largest thickness in the center and the thinnest thickness at the two ends improve the curvature of the flux waveforms. In this way, the eddy current losses can be reduced [56]. In this thesis the magnets are slightly curved. Figure 5.8 shows the shape of one magnet of the designed machine. The black magnet is without curving and the red magnet shows the magnet used for the investigated generator.

Figure 5.8: Magnet shape. Black without curving and red curved magnet.

The magnet width and coverage can affect the tooth eddy current losses of the machine, hence creating higher iron losses. In [57], it is shown that when the magnet coverage approaches a high value (close to 1.0), the tooth eddy current losses increases dramatically. On the other hand, if the magnet coverage is very low (magnet width less than one slot pitch), no tooth has constant flux density. Therefore, for a permanent magnet motor, the optimum magnet coverage according to [56] is

$$\frac{1}{mq} \leq \alpha \leq \frac{mq - 1}{mq} \tag{5.7}$$

where α is the magnet coverage, m is the number of phases and q is the number of slots per pole per phase.

Magnet width has also significant effects on cogging torque. The fundamental sinusoidal component of cogging torque can be eliminated by an appropriate choice of the magnet width [59]. The optimum magnet coverage to achieve the least cogging torque is

$$\alpha = \frac{n + 0.14}{mq} \tag{5.8}$$

where *n* is any integer number which satisfies $\alpha < 1$ [56]. Combining (5.7) and (5.8), the optimum magnet coverage for the SPMSG designed in this thesis is 0.79. The choice of α is then also considering that the yoke eddy current loss is assumed to be smaller when the magnet coverage is larger, as suggested in [56].

It was seen in Maxwell that if a magnet coverage of 0.7 is used, a slightly higher torque (0.4% higher) can be achieved with the same weight of the magnet. However, the cogging torque and the yoke eddy current loss may be increased.

In this work, a magnet coverage of 0.7 is used. The magnet thickness in the middle of the magnet (which is the thickest part) is 28 mm.

5.3.7 Active material weight

The active material weight for the SPMSG machine used in this thesis then becomes as given in Table 5.5

Table 5.5: Active material weight for SPMSG

Parameter	Value
Stator core steel weight	2397 kg
Rotor core steel weight	1731 kg
Copper weight	1024 kg
Permanent magnet weight	312 kg
Total active material weight	5464 kg

5.3.8 Winding arrangements

A double-layer winding is chosen for this machine, since double-layer windings can be designed with any coil pitch, while single-layer windings have limited possibilities in that regard [60] and armatures of nearly all synchronous machines are wound with double-layer windings [47]. The coils are selected to be short-pitched because the end winding of the short-pitch winding are shorter than the ones of the full-pitch winding which leads to lower cost of copper, lower resistance (higher efficiency) as well as it reduces certain harmonics in the air-gap field and the back-emf. The connection of phase A is illustrated in Fig. 5.9. Table 5.6 shows the winding data of the machine.
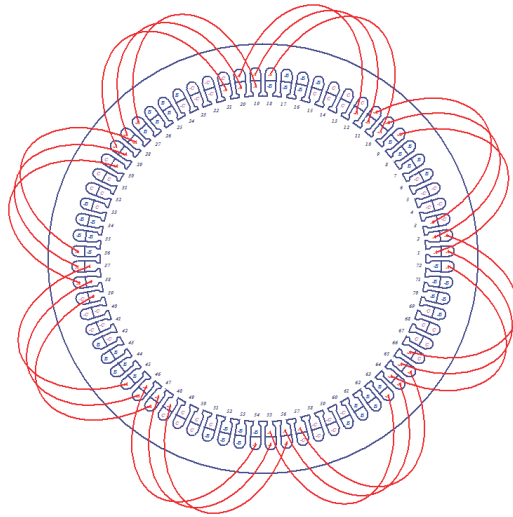
Figure 5.9: Phase A winding connection.

Table 5.6: Winding data for the SPMSG

Symbol	Parameter	Value
$2N_c$	Number of conductors per slot	14
N_c	Number of conductors per slot per phase	7
y	Coil pitch	8
a	Number of parallel branches	2
SF_g	Slot fill factor	50%

5.3.9 Parameters calculation

5.3.9.1 Winding factor

Using (2.40), (2.41) and (2.42) the winding factor for the first harmonic for this machine then becomes

$$k_w = 0.9452 \tag{5.9}$$

5.3.9.2 Phase resistance

The value of coil area (A_{coil} in Fig. 2.20) is taken from Maxwell which is

$$A_{coil} = 507.0392 \times 10^{-6} m^2 \tag{5.10}$$

The copper area is

$$A_{copper} = \frac{A_{coil}}{N_c} = 72.434 \times 10^{-6} m^2 \qquad (5.11)$$

According to (2.37) the length of a single end winding is

$$l_e = 0.626 m \qquad (5.12)$$

and according to (2.35) the copper length per phase is

$$l_{copper} = 131.964 m \qquad (5.13)$$

The copper resistivity at different temperatures can be found in Fig. 2.18. Therefore, The resistance at $20\,^{\circ}$C becomes

$$R = \rho \frac{l_{copper}}{A_{copper}} = 0.0172 \times 10^{-6} \frac{131.964}{72.434 \times 10^{-6}} = 31.33 \times 10^{-3} \Omega \qquad (5.14)$$

The resistance at $75\,^{\circ}$C becomes

$$R = \rho \frac{l_{copper}}{A_{copper}} = 0.0217 \times 10^{-6} \frac{131.964}{72.434 \times 10^{-6}} = 39.5 \times 10^{-3} \Omega \qquad (5.15)$$

According to (2.49) the slot fill factor is 50%. The slot area is calculated using the data in Table 5.4.

Skin effect

The skin depth can be calculated as

$$\delta = \sqrt{\frac{2\rho}{2\pi f \mu}} \qquad (5.16)$$

For low frequencies according to [61]

$$\frac{R_{ac}}{R} = 1 + \left(\frac{1}{48}\right) \left(\frac{r_{copper}}{\delta}\right)^4 \qquad (5.17)$$

The skin depth of the copper of this machine using (5.16) at $20\,^{\circ}$C for a copper permeability of 1.256629×10^{-6} is

$$\delta = 9.33 \times 10^{-3} m \qquad (5.18)$$

If we assume that the wires are rounded, the copper radius can be calculated as

$$r_{copper} = \sqrt{\frac{A_{copper}}{\pi}} \qquad (5.19)$$

which for this machine is $r_{copper} = 4.8 \times 10^{-3} m$

From (5.17)

$$R_{ac} = 1.0015 R \qquad (5.20)$$

which means that the skin effect can be neglected for this generator. The skin effect at $75\,^{\circ}$C is even smaller.

5.3.9.3 Inductance

According to (2.57), (2.95), (2.99), (2.101) and (2.103) the magnetizing and leakage inductances are calculated. The values of calculated inductances as well as the values taken from RMxprt is shown in Table 5.7. However, these values are only valid if the machine is working in the linear region.

Table 5.7: Non-saturated inductances for SPMSG

Symbol	Parameter	Calculated Value	RMxprt Value
L_{md} and L_{mq}	Magnetizing inductance (d and q)	9.57 mH	9.64 mH
L_{slot}	Slot leakage inductance	3.5 mH	-
$L_{tooth-tip}$	Tooth tip leakage inductance	0.966 mH	-
$L_{leakage}$	Total leakage inductance	4.49 mH	4.49 mH
L_{total}	Magnetizing plus leakage inductance	14.06 mH	14.14 mH
$L_{end-winding}$	End winding inductance	0.83 mH (1st method) 0.77 mH (2nd method)	0.4 mH

As can be seen in Table 5.7, most values match very well. However, the value of end winding inductance is different with different methods and the RMxprt value. In the RMxprt design, the end winding length (l_e) becomes the shortest possible, 0.42 m compared to 0.626 m which is the estimated value from (2.37). Therefore, the RMxprt value of $L_{end-winding}$ in Table 5.7 should be lower than the calculated value. With the end winding length of 0.42 m (instead of 0.626 m), the calculated value of $L_{end-winding}$ becomes instead 0.32 mH if (2.103) is combined with the accurate values of permeance factors from Table 2.1, which confirms the statement from [38] that end winding inductance is difficult to calculate accurately.

If the machine is not working in the linear region, we need a practical method, according to [38], to determine the saturated values of L_d and L_q. For any i_d and i_q, the flux linkages Ψ_d and Ψ_q can be calculated by FEM analysis, and then L_d and L_q can be obtained from

$$L_d = \frac{\Psi_d - \Psi_m}{i_d} \tag{5.21}$$

and

$$L_q = \frac{\Psi_q}{i_q} \tag{5.22}$$

For any value of i_q, from (5.22) a unique value of L_q can be obtained. However, to calculate L_d, using (5.21) a value for Ψ_m is needed. In [38], it is explained in details how Ψ_m should be calculated. The simplest way is that Ψ_m is equal to the value of Ψ_d when $i_d = i_q = 0$. This means that $\Psi_d - \Psi_m$ is zero. However, because of cross-saturation

$\Psi_d - \Psi_m$ can be nonzero when i_q is set to the normal load-point value, even if $i_d = 0$. Therefore, in [38], it is suggested to calculate Ψ_m with a load-point value of i_q and $i_d = 0$. In this way, Ψ_m is calculated with the full effect of cross-saturation in the q-axis, which decreases the value of Ψ_m and a unique value of L_d will be obtained from (5.21) at each operating point.

Table 5.8 shows the values of Ψ_m, L_d and L_q calculated using Maxwell, considering saturation for some operation points. As can be seen in Table 5.8, at full load operation (wind speed from 12-25 m/s), the total d- and q-axis inductances are 12 mH which is 83% of the inductance in the linear region.

Table 5.8: Inductance and magnet flux linkage considering saturation

Wind speed (m/s)	d and q total inductance (mH)	Ψ_m (Wb)
3	14.52	13.3
4	13.95	13.3
5	13.3	13.3
6	13.17	13.27
7	13.38	13.23
8	13.37	13.13
9	13.1	12.98
10	12.66	12.49
11	12.16	12.03
12-25	12	11.85

5.3.9.4 Current, current density and electric loading

Using Maxwell and setting the angle of current to $90°$ and applying three phase sinusoidal currents to the stator windings, the minimum current which gives the desired torque (63.7 kN.m) for the rated wind speed and higher speeds, is 635 A (RMS). Therefore the current density of this machine at full load based on (2.50) is

$$J = 4.4 \ A/mm^2 \tag{5.23}$$

According to (2.51), the electric loading of the machine becomes

$$A_c = 135 \ kA/m \tag{5.24}$$

With this value of electric loading, a direct water cooling is needed for this machine according to [34].

5.3.10 Torque, induced voltage and flux density

Now that the SPMSG is designed and the full load current is calculated, the torque, induced voltage waveforms and flux density distribution can be obtained in Maxwell. Applying the sinusoidal currents

$$
\begin{aligned}
i_a &= \sqrt{2}I_{rms}\cos\left(2\pi ft + \theta\right) \\
i_b &= \sqrt{2}I_{rms}\cos\left(2\pi ft + \theta - 120°\right) \\
i_c &= \sqrt{2}I_{rms}\cos\left(2\pi ft + \theta - 240°\right)
\end{aligned}
\tag{5.25}
$$

to the stator windings, the full load torque and induced voltages can be obtained in Maxwell. In (5.25), $I_{rms} = 635\ A$, $\theta = -90°$ and $f = 50\ Hz$.

Figure 5.10 shows the torque waveform as a function of time for one period for the designed SPMSG. As can be seen from the figure, the torque is negative which shows that the machine is operating as a generator. The generator torque is not constant and varies with rotor position. However, the torque ripple is low (peak to peak value of torque ripple is 2.4% of the total torque) and the average torque is 63.7 kNm which corresponds to a 5 MW power level.
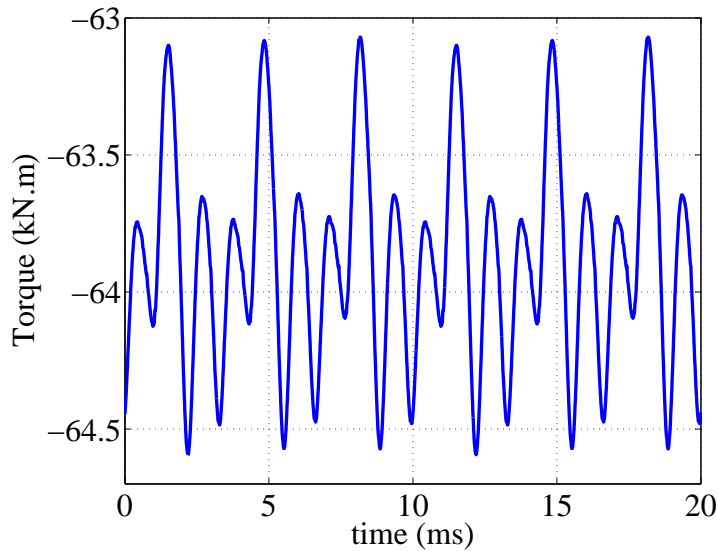
Figure 5.10: Torque waveform for SPMSG during one period.

The torque ripple can according to [62] be caused by

- Different magnetic permeance that the magnets face due to the stator slots, even when there is no current in the stator windings. This is often called cogging torque [63].

- Different permeance seen by the magnets due to magnetic saturation.

- Harmonics in the back-emf.

The 3-phase induced voltages of this SPMSG are shown in Fig. 5.11. As can be seen in the figure, the induced voltages are not sinusoidal. One reason is that the magnets are not totally curved. Using FFT (Fast Fourier Transform) the peak phase value of the induced voltages at full load are 5.017 kV. The FFT of different harmonics are shown in Fig. 5.12.
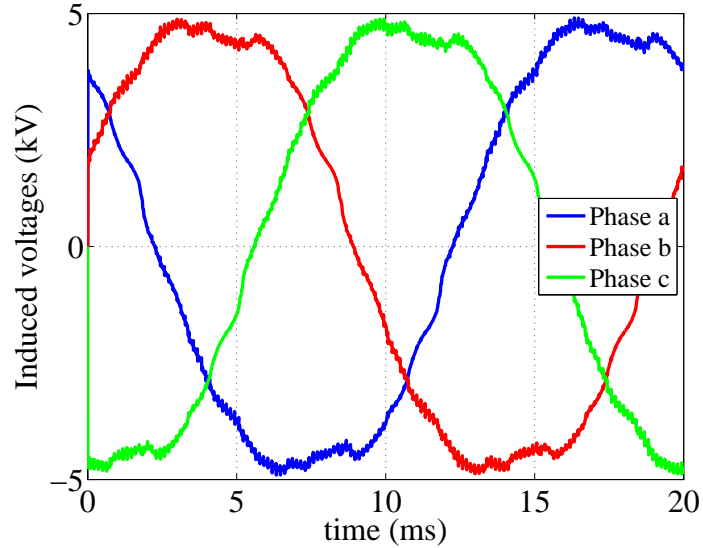
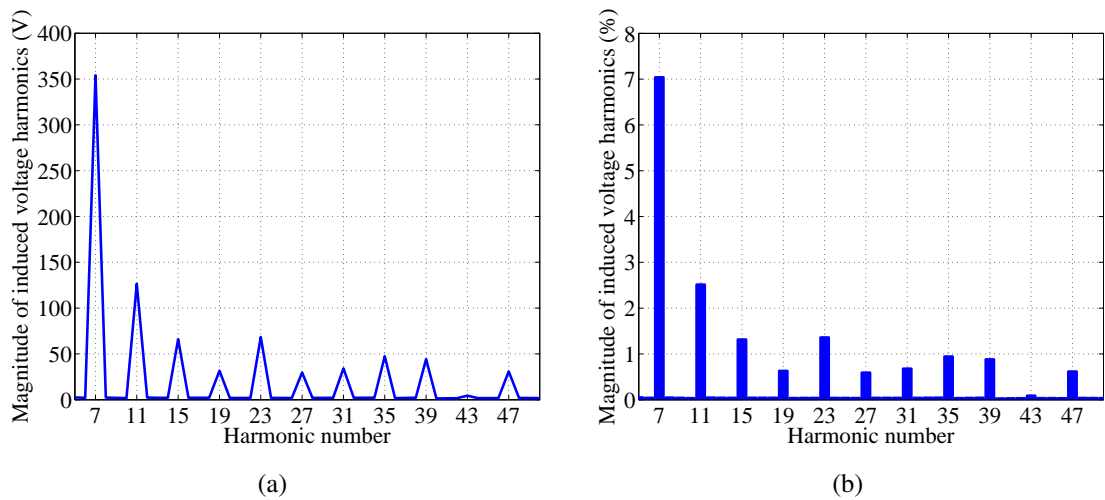Figure 5.11: Induced voltage waveforms for SPMSG at full load during one period.

Figure 5.12: Harmonics amplitude of the induced voltage for the SPMSG; (a) in Volt, (b) in percentage of the fundamental.

The Total Harmonic Distortion (THD) of the induced voltage for this SPMSG is 7.92%.

65

Figure 5.13 shows the flux density at (a) no-load and (b) at load for this machine. As can be seen, the maximum flux density in the teeth at no-load is 1.65 T and 1.4 T in the yoke. At load the highest flux density is 1.88 T.

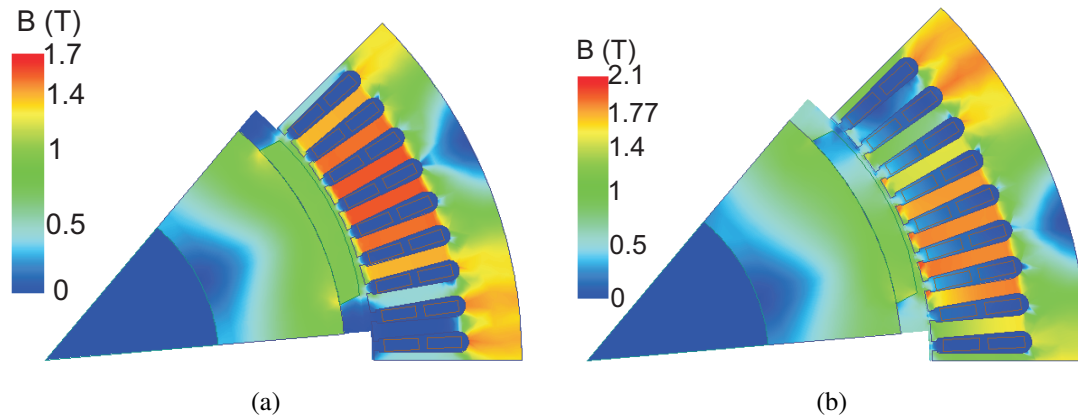(a)   (b)

Figure 5.13: Flux density for the SPMSG; (a) at no-load, (b) at full-load.

The period of the cogging torque is one slot pitch and the cogging frequency is [64]

$$f_{cogging} = 2mqf \tag{5.26}$$

where m is the number of phases, q is the number of slots per pole per phase and f is the machine frequency. To obtain the cogging torque in Maxwell, the mesh should be very fine. The cogging torque for the SPMSG in one period is shown in Fig. 5.14. The amplitude of the cogging torque is 240 Nm.
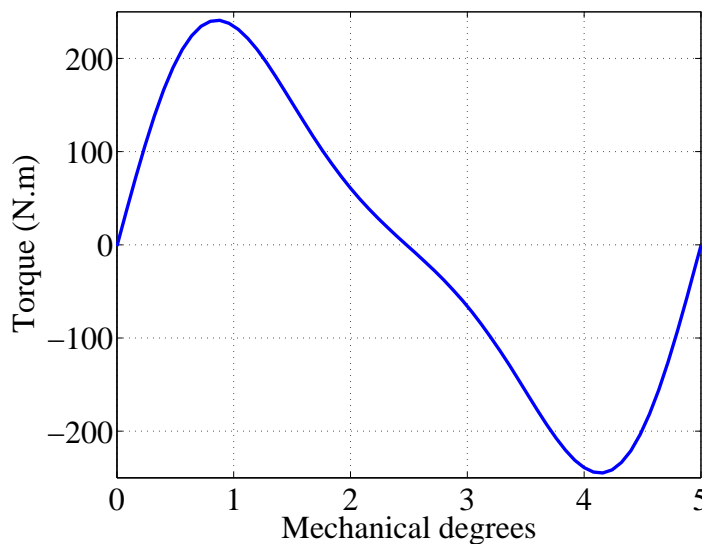
Figure 5.14: Cogging torque for SPMSG during one period.

5.4 Design of a 5 MW interior mounted permanent magnet synchronous generator

An Interior mounted Permanent Magnet Synchronous Generator (IPMSG) with the same amount of magnet and copper and almost the same amount of iron as the SPMSG in Section 5.3 is designed in order to compare the performance of the IPMSG with the SPMSG, see the main dimensions in Table 5.9. However, since rotors with interior magnets can provide a more secure magnet setting [57], the air-gap for the IPMSG is considered to be 3 mm which is calculated from (5.3). As the stator and shaft diameter of this machine have the same size as the dimensions of the SPMSG, because of the smaller air-gap and removing the magnets from the surface of the rotor, the rotor of the IPMSG is heavier than that of the SPMSG rotor.

Table 5.9: Machine size

Parameter	Value
Outer stator diameter	1100 mm
Inner stator diameter	758 mm
Outer rotor diameter	752 mm
Inner rotor diameter	400 mm
Stator and rotor length	945 mm

The stator slot size is the same as the SPMSG of which the data can be found in Table 5.4.

The active material weight for the IPMSG machine used in this thesis is given in Table 5.10.

Table 5.10: Active material weight of the IPMSG

Parameter	Value
Stator core steel weight	2397 kg
Rotor core steel weight	1812 kg
Copper weight	1024 kg
Permanent magnet weight	312 kg
Total active material weight	5545 kg

The magnet size is given in Table 5.11. The parameters are shown in Fig. 2.24.

Table 5.11: Magnet size

Parameter	Value
Magnet thickness	28 mm
Magnet width	195 mm
Bridge	1 mm
Rib	20 mm

The d- and q-axis magnetizing inductances as well as the leakage inductances for the IPMSG are calculated according to (2.58), (2.72), (2.95), (2.99), (2.101) and (2.103). The values thus achieved are shown in Table 5.12 and compared with values from RMxprt. As can be seen, the values match well with the exception of the end winding inductance, which was discussed in Section 5.3.9.3.

Table 5.12: Non-saturated inductances for IPMSG

Symbol	Parameter	Calculated Value	RMxprt Value
L_{md}	D-axis magnetizing inductance	12.45 mH	13 mH
L_{mq}	Q-axis magnetizing inductance	47.46 mH	49.88 mH
L_{slot}	Slot leakage inductance	3.5 mH	-
$L_{tooth-tip}$	Tooth tip leakage inductance	0.21 mH	-
$L_{leakage}$	Total leakage inductance	3.72 mH	4.14 mH
L_{totald}	D-axis magnetizing plus leakage inductance	16.16 mH	17.15 mH
L_{totalq}	Q-axis magnetizing plus leakage inductance	51.18 mH	54 mH
$L_{end-winding}$	End winding inductance	0.83 mH (1st method) 0.83 mH (2nd method)	0.4 mH

Table 5.13 shows the values of Ψ_m, L_d and L_q calculated according to (5.21) and (5.22) using Maxwell considering saturation for some operation points.

MTPA operation can be obtained with $I_{rms} = 555\ A$ and current angle $(\theta) = -125°$. With this current, the value of current density and electric loading is given in Table 5.14. These two parameters are calculated according to (2.50) and (2.51).

Table 5.14: IPMSG current density and electric loading

Symbol	Parameter	Value
J	Current density	$3.8\ A/m^2$
A_c	Electric loading	$118\ kA/m$

Table 5.13: Inductance and magnet flux linkage considering saturation for IPMSG

Wind speed (m/s)	d-axis total inductance (mH)	q-axis total inductance (mH)	Ψ_m (Wb)
3	19	46.4	13.91
4	17.5	46.2	13.91
5	11.54	44.45	13.87
6	12.04	42.49	13.77
7	11.3	38.31	13.52
8	10.76	31.63	13.19
9	10.32	26.18	12.72
10	10.29	23.32	12.2
11	10.36	21.74	11.81
12-25	10.42	21.34	11.7

5.4.1 Torque, induced voltage and flux density

Applying the sinusoidal currents

$$
\begin{aligned}
i_a &= \sqrt{2}I_{rms}\cos\left(2\pi ft + \theta\right) \\
i_b &= \sqrt{2}I_{rms}\cos\left(2\pi ft + \theta - 120°\right) \\
i_c &= \sqrt{2}I_{rms}\cos\left(2\pi ft + \theta - 240°\right)
\end{aligned}
\tag{5.27}
$$

to the stator winding the full load torque and induced voltages can be obtained in Maxwell. In (5.27), $I_{rms} = 555\ A$, $\theta = -125°$ and $f = 50\ Hz$. Figure 5.15 shows the torque waveform as a function of time in one period for the designed IPMSG. The average torque is 64 kNm (yielding 5 MW), similar to that of the SPMSG. The torque ripple is almost 10 kNm (about 15% of the rated torque) which is higher compared to the SPMSG case.
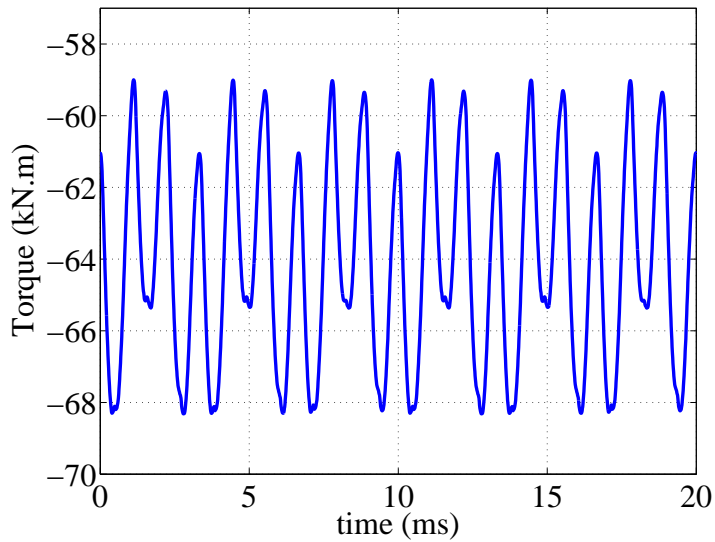
Figure 5.15: Torque waveform for IPMSG during one period.

The 3-phase induced voltages of this IPMSG are shown in Fig. 5.16. As can be seen, the induced voltages are not sinusoidal. Using FFT the peak phase value of the induced voltages at full load are 4.84 kV. The FFT of different harmonics are shown in Fig. 5.17.
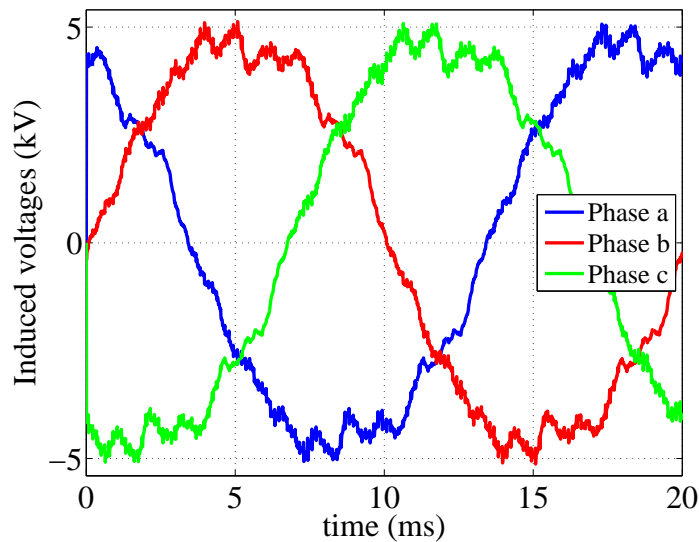

Figure 5.16: Induced voltage waveforms for IPMSG at full load during one period.
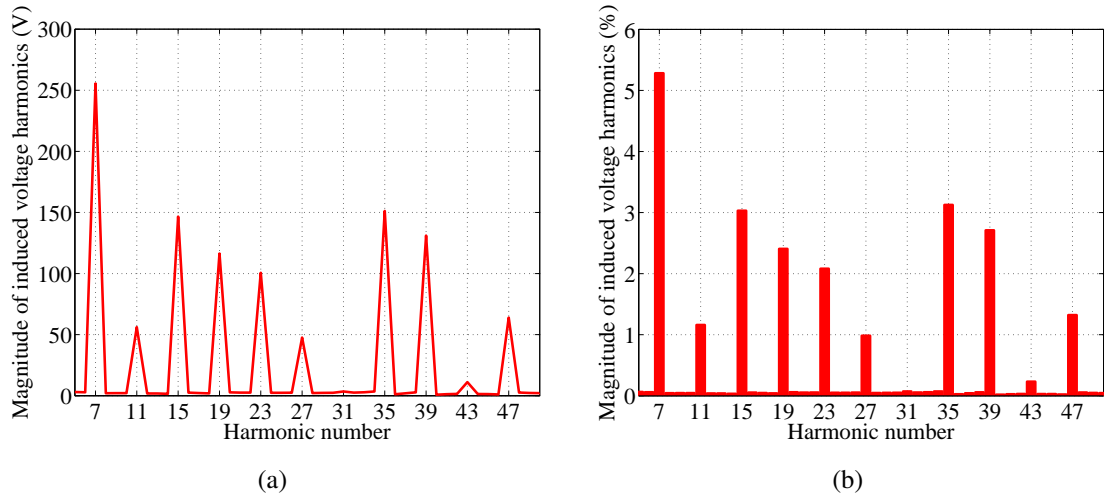
Figure 5.17: Harmonics amplitude of the induced voltage for the IPMSG; (a) in Volt, (b) in percentage of the fundamental.

The total harmonic distortion of the induced voltage for this IPMSG is 8.27%, which is higher compared to THD of the SPMSG.

Figure 5.18 shows the flux density at full load for this machine.
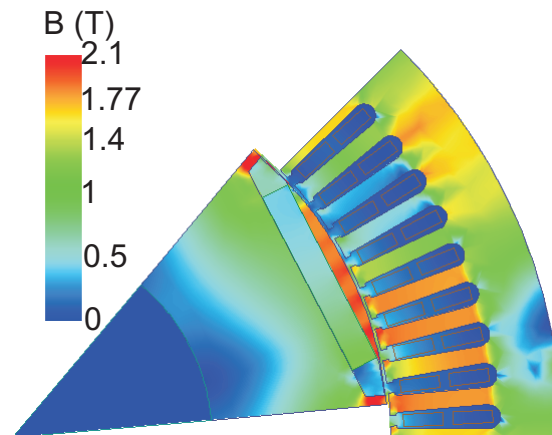
Figure 5.18: Flux density for IPMSG at full load.

The cogging torque is shown in Fig. 5.19. The amplitude of the cogging torque is 750 Nm which is above 3 times higher than for the SPMSG.
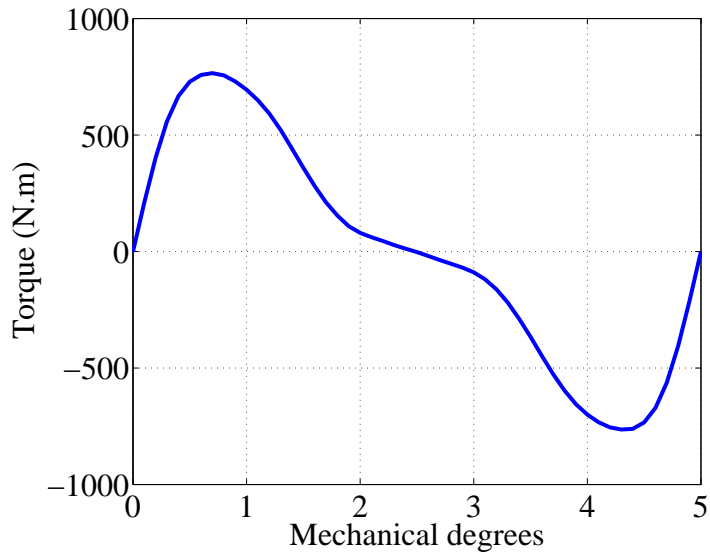
Figure 5.19: Cogging torque.

5.5 Design of a synchronous reluctance generator

A Synchronous Reluctance Generator (SynRG) with exactly the same size as the IPMSG is designed in Maxwell 2D. The shape of the barriers follows the shape of the flux lines for a solid rotor to optimize the performance of the machine. The machine has 4 barriers and one cut off barrier. The number of barriers are selected to decrease the torque ripple. The size of the barriers are given in Fig. 5.20.
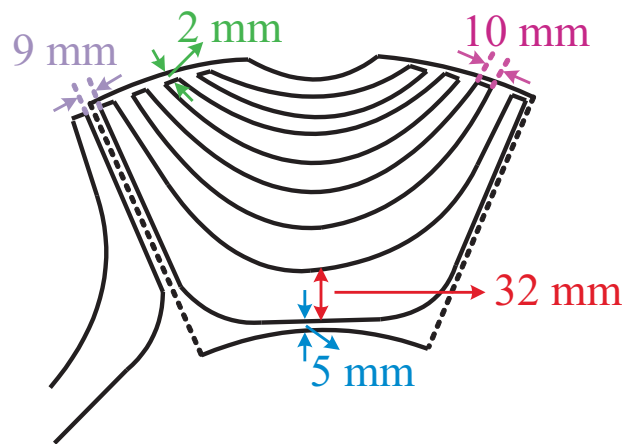
Figure 5.20: Rotor of SynRG.

The active material of the SynRG is given in Table 5.15 which shows that the SynRG has 80% weight of the IPMSG.

Table 5.15: Active material weight of the SynRG

Parameter	Value
Stator core steel weight	2397 kg
Rotor core steel weight	1050 kg
Copper weight	1024 kg
Total active material weight	4471 kg

5.5.1 Torque, induced voltage and flux density

Applying the sinusoidal currents

$$
\begin{aligned}
i_a &= \sqrt{2}I_{rms}\cos\left(2\pi ft + \theta\right) \\
i_b &= \sqrt{2}I_{rms}\cos\left(2\pi ft + \theta - 120°\right) \\
i_c &= \sqrt{2}I_{rms}\cos\left(2\pi ft + \theta - 240°\right)
\end{aligned}
\tag{5.28}
$$

to the stator winding, the full load torque and induced voltages can be obtained in Maxwell. In (5.28), $I_{rms} = 555\ A$ which is the same current value as for the IPMSG at full load, $\theta = -68°$ and $f = 50\ Hz$.

Figure 5.21 shows the torque waveform as a function of time for one period for the designed SynRG. The average torque is 47 km which is 74% of that of the maximum IPMSG torque (yielding a power of 3.7 MW). The peak to peak torque ripple is about 9 kNm which is 19% of the rated torque.
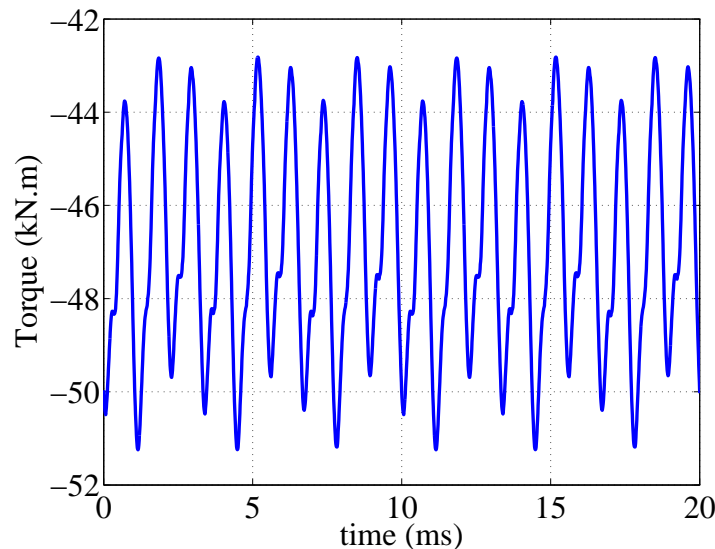
Figure 5.21: Torque waveform for SynRG during one period.

The 3-phase induced voltages of this SynRG are shown in Fig. 5.22. As can be seen the induced voltages are not purely sinusoidal. Using FFT the peak phase value of the

induced voltages at full load are 4.9 kV. The FFT of different harmonics are shown in Fig. 5.23.
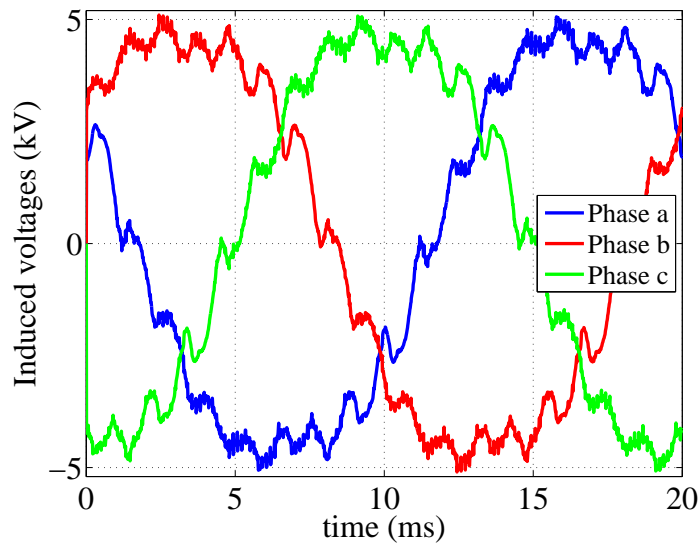

Figure 5.22: Induced voltage waveforms for SynRG at full load during one period.
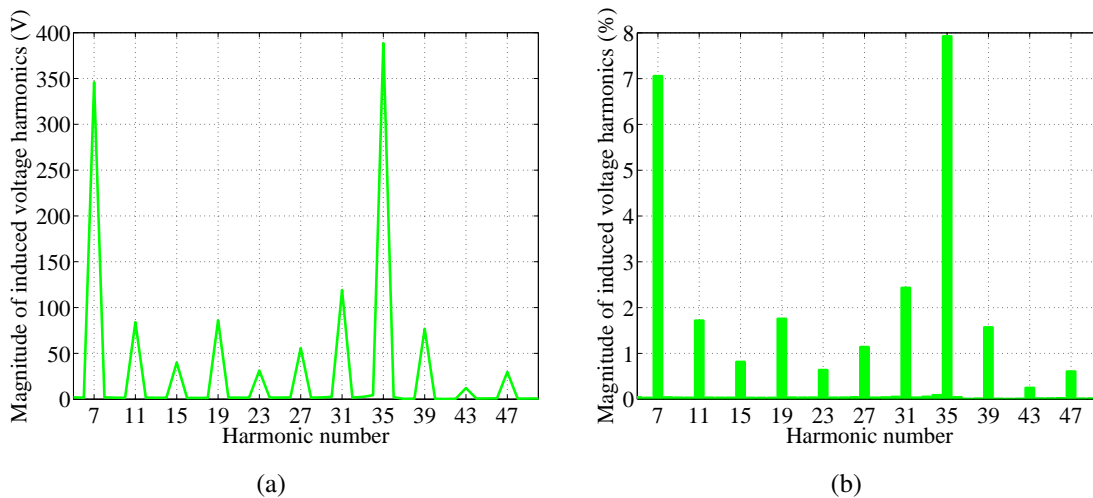

Figure 5.23: Harmonics amplitude of the induced voltage for the SynRG; (a) in Volt, (b) in percentage of the fundamental.

The total harmonic distortion of the induced voltage for this SynRG is 11.39%.

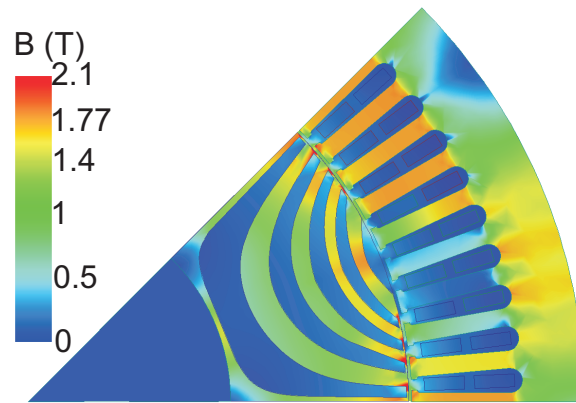Figure 5.24 shows the flux density at full load for this machine.

Figure 5.24: Flux density for SynRG at full load.

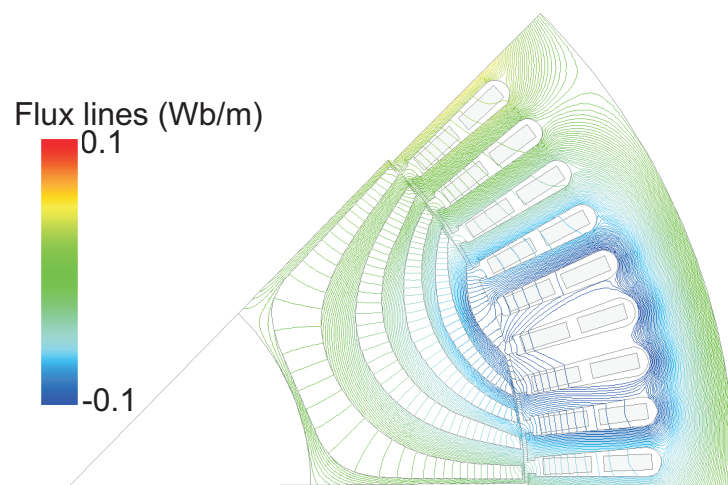Figure 5.25 shows the flux lines at full load for this machine.

Figure 5.25: Flux lines for SynRG at full load.

5.6 Torque reduction

As it was seen in Section 5.4.1 and 5.5.1, the IPMSG and the SynRG have high torque ripples. There are different possibilities to reduce the torque ripple of a machine. A common method is to skew the stator slots or the rotor [64]. The combination of pole and slot numbers in permanent magnet machines has also a significant effect on the cogging torque [58] and [62]. To reduce the cogging torque of the machine designed in Section 5.4 the number of slots can be increased. However, if the number of slots are increased up to 96 which gives $q=4$, then the size of the slots will be very small. To avoid very small slots, a slot number between 72 and 96, e.g. 90 slots can be selected. In [65], it is shown that not all combinations of slots and pole numbers are feasible. The winding is feasible if

$$\frac{Q}{mGCD\left(Q,p\right)} \tag{5.29}$$

is an integer number, where $GCD\left(Q,p\right)$ is the Greater Common Divisor between number of slots and pole pairs. According to (5.29), 78, 84 and 90 slot numbers give a feasible winding. Here, a slot number of 90 is selected. Selecting 90 slots, the number of slots per pole per phase (q) becomes 3.75. If the number of slots per pole per phase is not an integer then we will have a fractional slot winding machine which has some benefits such as a possibility of reducing torque ripple and cogging torque and flux weakening capability [66]. Furthermore, harmonics in the back-emf can be reduced [47] and [67].

5.6.1 Skewing

Skewing of the IPMSG stator is modeled in Maxwell 3D, in order to investigate any difference in output torque and torque ripple between the skewed and the non-skewed designs. The stator lamination as well as the stator coils are skewed one slot pitch, yielding a skew angle, α_{skew}, of 5 mechanical degrees (for a 72-slot machine). See Fig. 5.26 which shows half the stator with the $5\,^{\circ}$ skew.
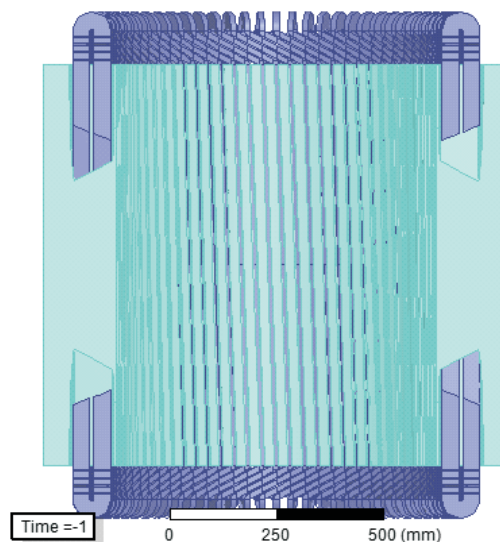

Figure 5.26: Half a 72-slot stator with a $5\,^{\circ}$ (one slot-pitch) skew.

In order to solve this model in Maxwell, with a reasonably good mesh density, the model of one pole-pitch is divided in to five parts (excluding the end windings) in the length-direction, see Fig. 5.27. Each part has a skew angle of α_{skew}/n degrees. To position the rotor in the correct position, the rotor for each modeled part, except for the first part, is rotated $-(k-1)(\alpha_{skew}/n)$ degrees, where α_{skew} is the skew angle, n is the number of subdivisions, and $k = 2, 3, 4, 5$ is the number of the part. Thus, for the machine in

question, the model of part 1 does not have its rotor rotated, whereas the part 2 rotor is rotated -1 °, and -2 °, -3 °, and -4 ° for part 3, 4 and 5.
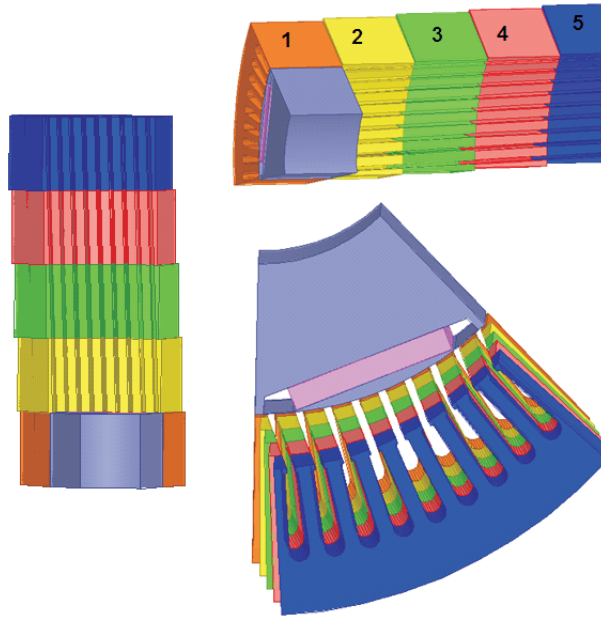

Figure 5.27: Five parts of one pole-pitch of a 72-slot stator with a 5 ° (one slot-pitch) skew.

The solutions for each part for torque, T_n, and phase flux linkages, ψ_{An}, ψ_{Bn} and ψ_{Cn} are summed up, yielding the total torque and phase flux linkages

$$T = \sum_{n=1}^{5} T_n \tag{5.30}$$

and

$$\psi_A = \sum_{n=1}^{5} \psi_{An} \qquad \psi_B = \sum_{n=1}^{5} \psi_{Bn} \qquad \psi_C = \sum_{n=1}^{5} \psi_{Cn} \tag{5.31}$$

Those values are then compared with the torque and flux linkages from the non-skewed model. For this purpose a 3D model of the IPMSG in Section 5.4 is created. The results can be seen in Fig. 5.28 and Fig. 5.29.
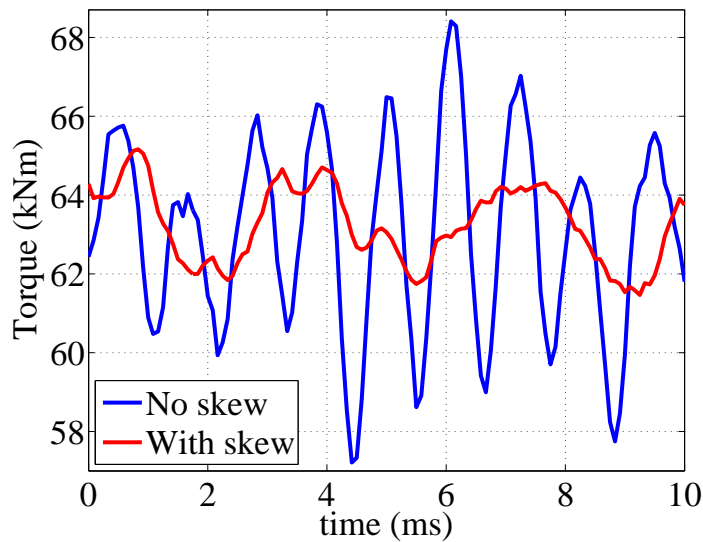
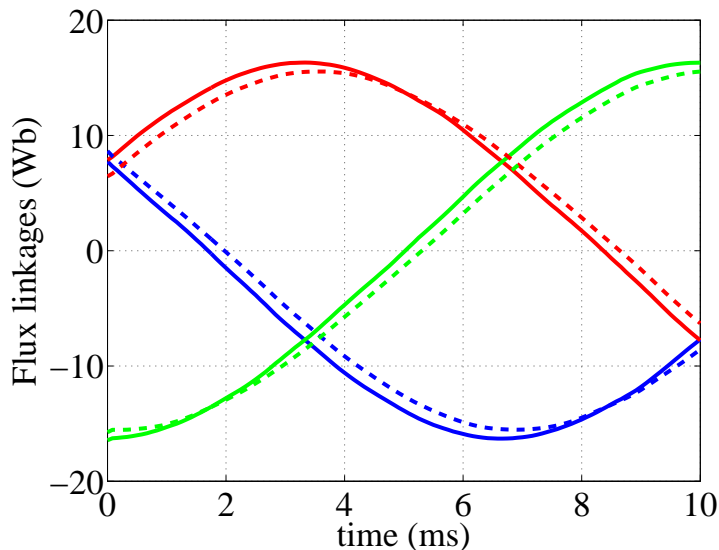Figure 5.28: Torque for the skewed and non-skewed IPMSG.

Figure 5.29: Phase flux linkages for the skewed and non-skewed IPMSG. Phase A blue, Phase B red, Phace C green. Solid lines without skew and dashed lines with skew.

It is clearly seen in Fig. 5.28 that the torque ripple is less for the skewed case with both a lower value (3 kNm compared to 11 kNm for the non-skewed case) and a lower frequency. When comparing mean values of torque, the results are nearly identical with a value of 63.04 kNm and 63.25 kNm for the non-skewed and the skewed machines respectively (yielding a 0.3% difference). According to the flux linkage comparison, as seen in Fig. 5.29, the flux linkages for the non-skewed case is slightly higher than for the skewed case (a difference of 6%), which should give a slightly higher torque for the non-skewed

case.

Likewise, the skewing factor, calculated from (2.38), is for the fundamental 0.995, which should give a slightly higher torque for the non-skewed case for which the skewing factor is unity.

However, the difference is so small, so the torque calculations from the 3D FEM model of the machine cannot be expected to show this. The accuracy of the torque calculations could be improved with a denser mesh but already with the meshed used the solution time is very long (over two days for each part). The slot harmonics are [34]

$$\pm 2mqc + 1 \tag{5.32}$$

where $c = 1, 2$. For the IPMSG with 72 slots, the slot harmonics are -17, 19, -35, and 37. The skewing factors for those harmonics and for the fundamental are shown in Table 5.16. The values are calculated from (2.38) which could also be expressed as

$$k_{sqv} = \frac{\sin v\alpha_{skew}/2}{v\alpha_{skew}/2} \tag{5.33}$$

where α_{skew} is the skew angle in electrical radians. As can be seen in Table 5.16, the fundamental skew factor is practically unity whereas the skew factors for the slot harmonics are quite low.

Table 5.16: Skew factor for the fundamental and for the slot harmonics.

Harmonic	1	17	19	35	37
Skew factor	0.995	0.058	0.052	0.028	0.027

5.6.2 Fractional slot winding interior mounted permanent magnet synchronous generator

The interior mounted permanent magnet synchronous generator fractional slot winding (IPMSGFS) with 90 slots was designed with exactly the same rotor as the IPMSG in Section 5.4 and the same current density and almost the same electric loading. The winding arrangement is done according to [47]. In (2.44) the number of slots per pole per phase, q, was given. In [47], it is shown that q, can also be expressed as a fraction *z/n*, thus

$$q = \frac{Q}{2pm} = \frac{z}{n} \tag{5.34}$$

where z and n should be reduced to their lowest terms. For this machine which has 90 slots and 4 pole pairs, $n = 4$ and $z = 15$. If the winding is a double-layer winding (which is often the case for fractional slot windings) then the coil sides in one layer is first

arranged, and then the locations of the coil sides in the other layer is obtained with a shift corresponding to the coil pitch.

The winding is arranged so that the number of slots varies from phase belt to phase belt and so that there is a balance, yielding identical induced voltages from the three phase windings.

When arranging the coil sides, each phase should cover an electrical angle, β, of 60° electrical degrees, according to

$$
\begin{aligned}
0 \le \beta_A < 60 \\
60 \le \beta_B < 120 \\
120 \le \beta_C < 180
\end{aligned}
\tag{5.35}
$$

The slot angle in electrical degrees is calculated as

$$
\alpha_s = p \frac{2\pi}{Q}
\tag{5.36}
$$

For this machine, according to (5.36) the slot angle in electrical degrees is 16°. Therefore, according to (5.35) and considering a slot angle of 16° in electrical degrees, the first 4 slots can be used for phase A(+), the following 4 slots for phase C(-), and the next 4 slots for phase B(+), but then 3 slots for phase A(-), where + and - shows the direction of the phase belts.

The coil pitch of the winding, y, expressed in number of slots, is chosen so that

$$
yn \approx mz
\tag{5.37}
$$

where n and z are calculated according to (5.34). In this machine, the coil pitch can be 11 or 12, as $mz = 45$ and $n = 4$ and the best choice is thus 11.

Consequently, the locations of the coil sides in the upper layer are obtained by copying and shifting the lower layer, corresponding to the coil pitch which is 11 in this machine.

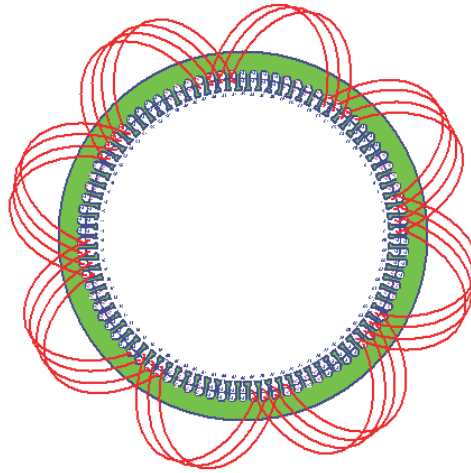The phase A winding distribution for this IPMSGFS is shown in Fig. 5.30.

Figure 5.30: Phase A coil side distribution for a fractional slot winding for an 8-pole, 90-slot machine.

As the number of slots in the IPMSGFS has increased to 90 compared to 72 in the IPMSG, the stator slot size will be smaller. Stator slot size values are shown in Table 5.17.

Table 5.17: Stator slot size for the IPMSGFS

Parameter	Value
Hs0	6 mm
Hs1	2 mm
Hs2	90 mm
Bs0	8.32 mm
Bs1	12.8 mm
Bs2	19.2 mm
Rs	12 mm

To keep the current density value for this machine the same as the current density in the IPMSG the number of conductors in the slot needs to be changed. The winding data of the IPMSGFS is given in Table 5.18.

Table 5.18: Winding data for the IPMSGFS

Symbol	Parameter	Value
$2N_c$	Number of conductors per slot	12
N_c	Number of conductors per slot per phase	6
y	Coil pitch	11
a	Number of parallel branches	2
SF_g	Slot fill factor	50%

The parameters of the machine are given in Table 5.19. As can be seen, the fundamental winding factor for the IPMSGFS (0.955) is slightly higher than the fundamental winding factor of the IPMSG (0.9452).

Table 5.19: IPMSGFS parameters

Symbol	Parameter	Value
J	Current density	$3.8\ A/m^2$
A_c	Electric loading	$116\ kA/m$
k_w	winding factor	0.955

The active material weight for the IPMSGFS is given in Table 5.20. The copper weight is calculated assuming that the end winding length is 0.626 m which is taken from (2.37). The values of the weight given in Table 5.20 are practically the same as for the IPMSG, with weights as given in Table 5.10.

Table 5.20: Active material weight

Parameter	Value
Stator core steel weight	2419 kg
Rotor core steel weight	1812 kg
Copper weight	1006 kg
Permanent weight	312 kg
Total active material weight	5549 kg

The torque at full load with $I_{rms} = 508.6\ A$ and $\theta = -124°$ is shown in Fig. 5.31 which shows the torque waveform as a function of time for one period for the designed IPMSGFS. As can be seen the torque ripple has decreased substantially while the average torque only has dropped down with less than 1% to 63.4 kNm.
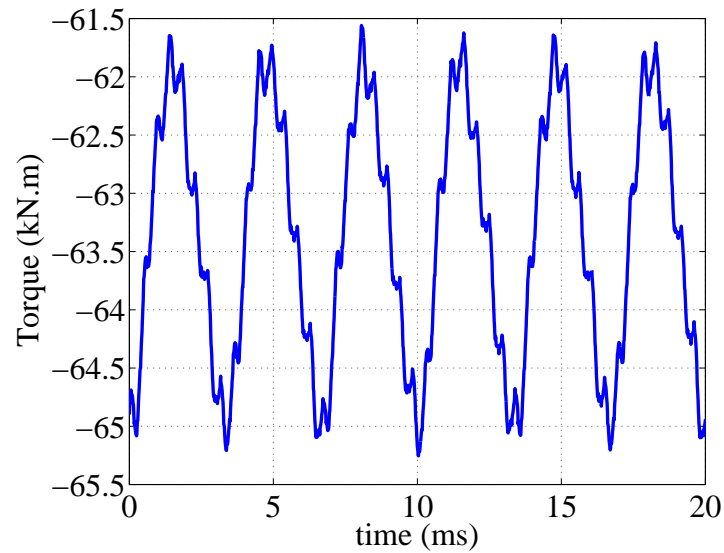
Figure 5.31: Torque waveform for IPMSGFS during one period.

The 3-phase induced voltages of this IPMSGFS are shown in Fig. 5.32 and the magnitude of the induced voltage harmonics are shown in Fig. 5.33. The peak phase value of the induced voltages at full load are found to be 5.2 kV. The THD of the induced voltage for this IPMSGFS is 7.26%, which is lower compared to the value of the THD of the induced voltage in the IPMSG (8.27%).
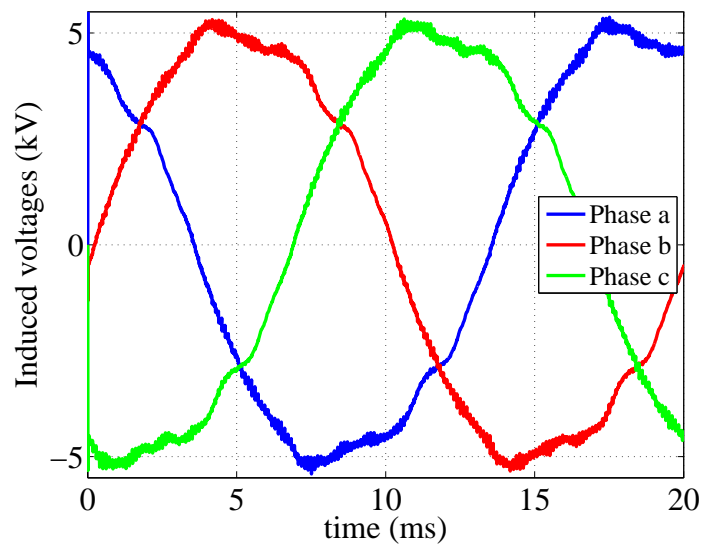

Figure 5.32: Induced voltage waveforms for IPMSGFS at full load during one period.
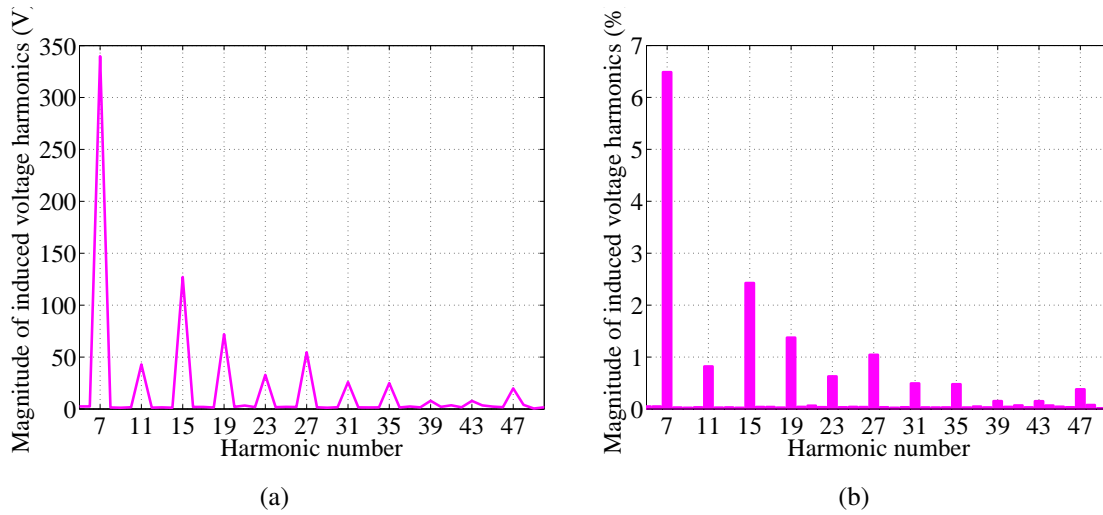
Figure 5.33: Harmonics amplitude of the induced voltage for the IPMSGFS; (a) in Volt, (b) in percentage of the fundamental.

The cogging torque for the IPMSGFS in one period is shown in Fig. 5.34. The highest amplitude of the cogging torque is 40 Nm.
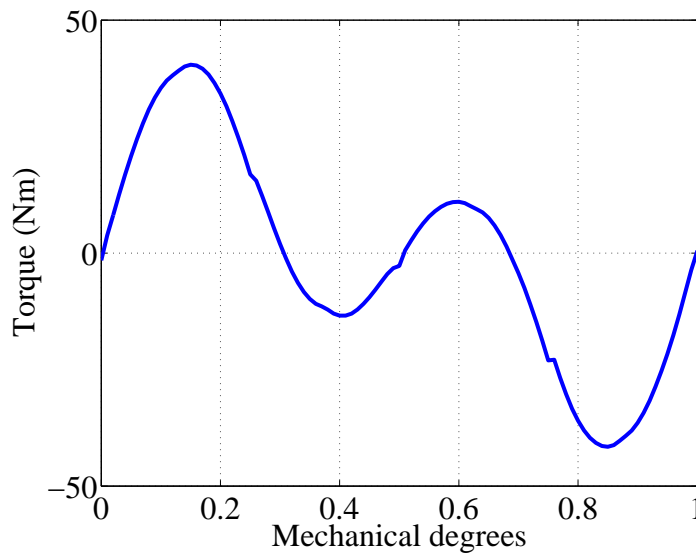
Figure 5.34: Cogging torque for IPMSGFS during one period.

According to (5.26), one period of the cogging torque is 4 mechanical degrees (because of 90 slots), since that equation gives a cogging torque period of one slot pitch. However, it seems that this is not valid for a fractional slot machine. In the integer slot (72 slots) machine the symmetry section equals one pole pitch while in the case with the fractional slot machine (90 slots), we need to model half a machine (4 pole-pitches) to get a

symmetric part of the winding. Therefore, it is suggested that for fractional slot machines the cogging torque frequency should be

$$f_{cogging} = 2mqfn_{ps} \tag{5.38}$$

where n_{ps} is the number of pole pitches per symmetry section. The reason to the higher cogging frequency (and much lower amplitude) would be that for fractional slot windings the magnet edges of the four poles are all in different places relative to the slot openings, so they will cause maximum cogging torque at different rotor positions.

5.6.3   Fractional slot winding synchronous reluctance generator

To design this machine, the stator of the IPMSGFS in the previous section is kept and the rotor is replaced by the rotor in Section 5.5.

The torque at full load with $I_{rms} = 508.6\ A$ and $\theta = -67°$ is shown in Fig. 5.35. The figure shows the torque waveform as a function of time for one period for the designed SynRGFS. As can be seen, the torque ripple has decreased, from 9 kNm to less than 2 kNm. The average torque is 46.6 kNm which shows that the average torque has decreased 0.85% compared to the 72 slot synchronous reluctance machine in Section 5.5.
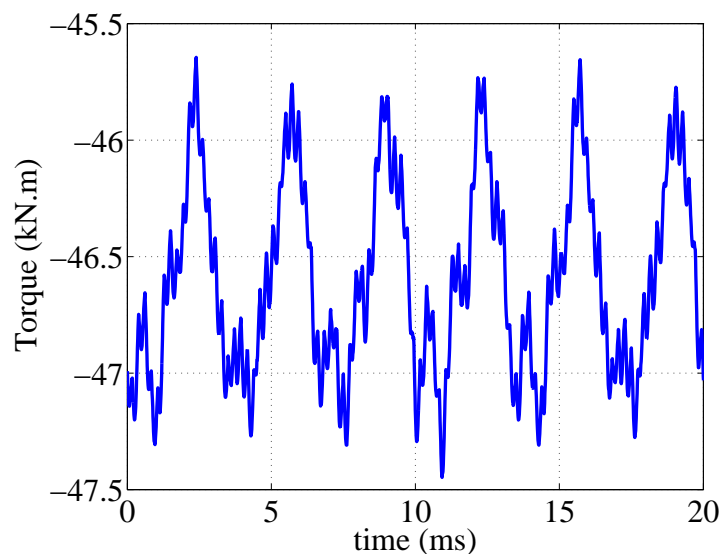

Figure 5.35: Torque waveform for SynRGFS during one period.

The 3-phase induced voltages of this SynRGFS are shown in Fig. 5.36. As can be seen the induced voltages have less harmonics compared to the induced voltages in section 5.5. Using FFT the peak phase value of the induced voltages at full load are 5.3 kV. The FFT of the different harmonics are shown in Fig. 5.37.
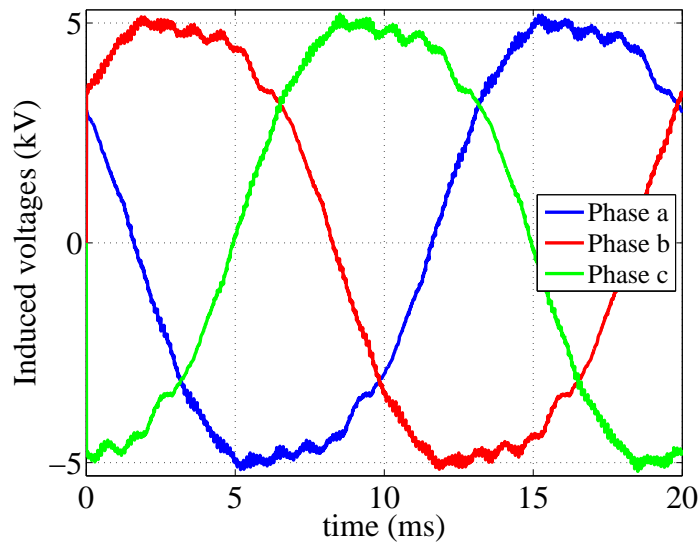
Figure 5.36: Induced voltage waveforms for SynRGFS at full load during one period.
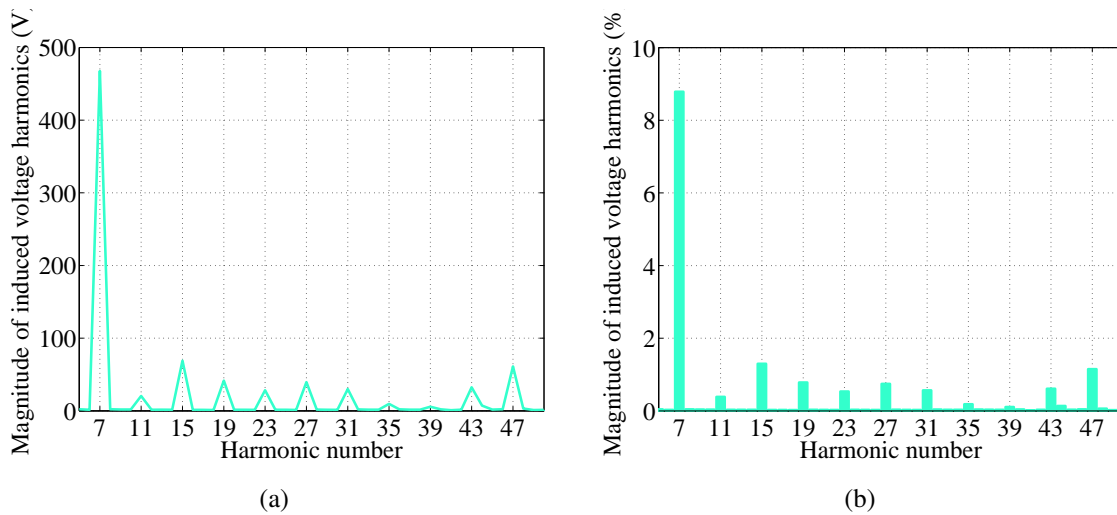

Figure 5.37: Harmonics amplitude of the induced voltage for the SynRGFS; (a) in Volt, (b) in percentage of the fundamental.

The total harmonic distortion of the induced voltage for this SynRGFS is 9.09%. This value is lower compared to the value of the THD of the induced voltage in the SynRG which was 11.39%.

5.7   Design of an active rectifier

The power electronic converter used is a 2-level traditional (6-pulse) transistor converter. Each of these 6 transistors consists of several series and parallel modules (as shown in

Fig. 5.38) to obtain the required voltage and current rating. Three IGBT modules of various blocking voltage ratings are considered to be used in the converter in this investigation. In Section 5.9, this will be explained more.
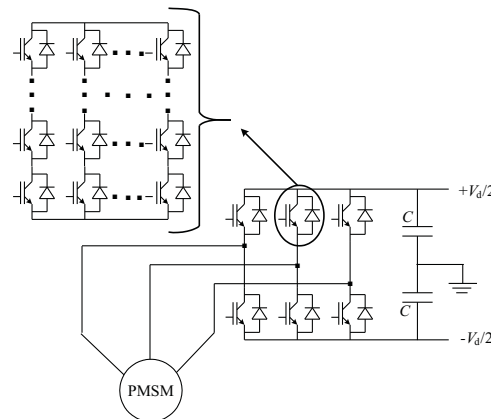

Figure 5.38: Schematic view of the system with active rectifier.

5.8 DC-link voltage selection

If we are using an active rectifier and we are able to control the machine voltage it is important to choose a proper voltage for the machine, since the machine and converter losses are dependent on this voltage. To investigate what voltage gives less losses and more annual efficiency of the wind turbine, three voltages are considered:

1. The minimum voltage at which the MTPA is possible for the whole operation region.

2. The minimum voltage which gives the desired torque.

3. A voltage between voltage 1 and 2.

In order to determine the needed dc-link voltage, the following expression has been used

$$V_{dc} = \frac{2V_{ac}}{0.95} \tag{5.39}$$

where V_{ac} is the peak line to neutral voltage of the machine. The constant 0.95 in (5.39) has been used to consider semiconductor losses, control margin and blanking time of the transistors.

After the dc-link voltage is selected, the number of IGBT modules in series to obtain the required voltage can be calculated as

$$n_{series} = \frac{V_{dc}}{V_{ref}} \tag{5.40}$$

where V_{ref} is the module reference voltage (voltage level for which the switching losses are given in the data sheet).

5.9 IGBT module selection

There is a variety of IGBT modules from low rated voltage (1.7 kV) to high rated voltage (6.5 kV) that can be used for the converter of a wind turbine system. However, it should be mentioned that an IGBT module cannot be operated at its rated voltage, instead there is a reference voltage of about half of the rated voltage that is suitable for an IGBT module. If the generating system of a wind turbine uses a low voltage generator (e.g. 690 V), then it is sufficient to use 1.7 kV IGBT components. An example is the Gamesa G10X 4.5 MW turbine which is a medium rotor speed permanent magnet generator [23]. There is, however, an interest to increase this voltage since a medium voltage drive train can be more convenient to install, due to lower current levels, leading to less extensive cabling. It can then offer lower copper losses than the same rated low voltage set-up [24]. According to [25] and [26] the rated voltage of the IGBTs typically increases with increasing dc-link voltage for synchronous type generators. The off-shore Areva Multibrid M5000 wind turbine [27], which is a 5 MW permanent magnet synchronous generator with rated voltage of 3.3 kV uses the ABB converter platform PCS 6000 Wind since the end of 2009 [24] [28]. This medium voltage converter has the voltage levels of 3.3 kV and 4.16 kV [29].

In this work it is important to investigate which voltage module should be used, since the generator designed in Section 5.3 is a medium voltage generator. We need to investigate if it is beneficial to use modules of higher voltage rating, still a couple in series, or if it is better to use many of lower voltage modules.

From an on-state loss point of view, it seems beneficial to use a module of higher voltage. However, we also need to study the switching losses and the resulting total energy efficiency.

To investigate this issue, a 5 MW surface permanent magnet machine with the data given in Table 5.21 is considered as the generator. It is considered that the machine works in the linear region. The rated voltage of the machine is 5.8 kV which gives operation at MTPA up to about 2/3 of the rated power without using any field weakening. For the active rectifier converter, three different modules has been investigated [68], [69] and [70]. The first module has a high rated voltage (6500 V/750 A), the second module is a medium voltage module (3300 kV/1500 A) and the last module has a fairly low voltage (1700 V/2400 A). The operating temperature of the IGBTs and diodes is assumed to be $125\,°C$. It is assumed that the rated RMS current is equal to half the rated value of

the IGBT module, and that there is sufficient heat transfer through water cooling of the converter for these selections. The converter losses are calculated according to (3.3), (3.4), (3.8) and (3.9).

Table 5.21: Data for the generator used for the IGBT module investigation

Parameter	Value
Rated Output Power	5000 kW
Number of Poles	8
Frequency	50 Hz
Number of Stator Slots	24
Armature Phase Resistance	0.0375 Ω
D-Axis main Reactance	2.93 Ω
Q-Axis main Reactance	2.93 Ω
Armature leakage Reactance	1.9 Ω
Rated voltage	5.8 kV
Armature Current Density	5.5 A/mm^2
Iron-Core Loss at rated operation	9883.42 W
Armature Copper Loss at rated operation	62061.4 W
Power factor	0.81
Rated speed	750 rpm

Using (5.39), the related dc-link voltage of a 5.8 kV generator voltage is 10 kV. To broaden the investigation, in addition to the 10 kV dc-link voltage, another dc-link voltage (10.7 kV) which gives less losses for the total system compared to 10 kV dc-link voltage is also considered.

To get the desired voltage and current, a non-integer (fractional) number of series and parallel of the IGBT-modules is used in order to be as accurate as possible. The number of series and parallel modules are:

For 10 kV dc-link voltage,

- 2.8 series and 1.6 parallel modules for 6.5 kV/750 A.

- 5.5 series and 0.8 parallel modules for 3.3 kV/1500 A.

- 11.1 series and 0.5 parallel modules for 1.7 kV/2400 A.

For 10.7 kV dc-link voltage,

- 3 series and 1.5 parallel modules for 6.5 kV/750 A.

- 6 series and 0.8 parallel modules for 3.3 kV/1500 A.

- 12 series and 0.5 parallel modules for 1.7 kV/2400 A.

The results are shown in Chapter 6.

5.10 Design of a diode rectifier

In this section a diode (passive) rectifier is described. In order to implement the system, the SIMPLORER software is used. SIMPLORER is a simulation program used to simulate electric circuits and enables a quick and accurate design of complex power electronic and electrically controlled systems.

A diode rectifier as shown in Fig. 5.39 is considered in Simplorer. The parameters of a surface permanent magnet generator with the data given in Table 5.21 is considered for the alternative voltages, resistances and inductances. It is assumed that the diode rectifier is connected to a DC voltage source, i.e. the dc-link voltage is constant for a constant wind speed. The voltage drop over the diode is ignored.

By changing the value of the DC voltage source (dc-link voltage) the transmitted power can be taken from Simplorer. The simulation shows that the transmitted electrical power is dependent upon DC source voltage.

Here only an example will be shown, for full result coverage, please see [71].
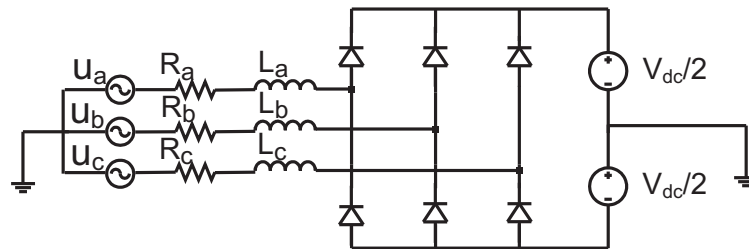
Figure 5.39: The SPMSG conncted to the dc-link voltage through a diode rectifier.

Chapter 6

Results & Analysis

In this chapter, it is first investigated, from the loss point of view, if it is beneficial to use higher voltage rating IGBT modules or lower voltage rating IGBT modules for an active rectifier in a wind turbine that uses a medium voltage generator and an IGBT active rectifier. The results of this part is used in the next sections. Then the machine and converter losses as well as the annual energy efficiency of a wind turbine comprising of a SPMSG and an IGBT active rectifier for three different dc-link voltages are shown. Next a comparison between a wind turbine consisting of a SPMSG and a wind turbine consisting of an IPMSG is presented. The SPMSG and the IPMSG have the same size. Finally in the last sections, the machine and converter losses as well as annual energy efficiency for a wind turbine using a SynRG is presented and the machine losses and power factor of the SynRG is compared to an IPMSG with the same size.

6.1   IGBT module selection

As was mentioned in Section 5.9, when the generator of a wind turbine is a medium or high voltage generator it is important to know whether it is beneficial that the converter is composed of higher voltage IGBT modules or if a converter consisting of low voltage module is more advantageous. To investigate this issue, a 5 MW surface permanent magnet generator with the data given in Table 5.21 is considered. For the active rectifier, three different modules have been investigated. Two higher voltage modules (6.5 kV and 3.3 kV) and one lower voltage module (1.7 kV). It is assumed that the generator works in the linear region. Two dc-link voltages (10 kV and 10.7 kV) are studied. The converter and machine losses as well as the annual energy efficiency of the system are investigated and compared for different module voltage levels.

6.1.1 Converter losses

The on-state (conduction) and switching losses of the converter built up with the different modules for the two used dc-link voltages are shown in Fig. 6.1 to Fig. 6.3. To calculate the converter losses (3.3), (3.4), (3.8) and (3.9) are used. The various modules are composed to complete phase legs that have the same total voltage withstand ability as well as current ability. In order to have a high accuracy, the phase legs were composed using non-integer values of the modules. The number of series and parallel modules are given in Section 5.9. The switching frequency is 0.5 kHz, since this is thought to be the lowest switching frequency that can be used for this 50 Hz machine.
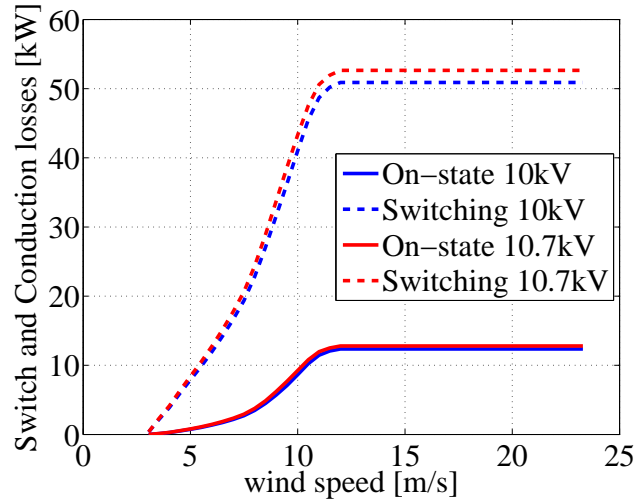
Figure 6.1: On-state and switching losses for 6500 V/750 A module with F_{sw}=0.5 kHz.
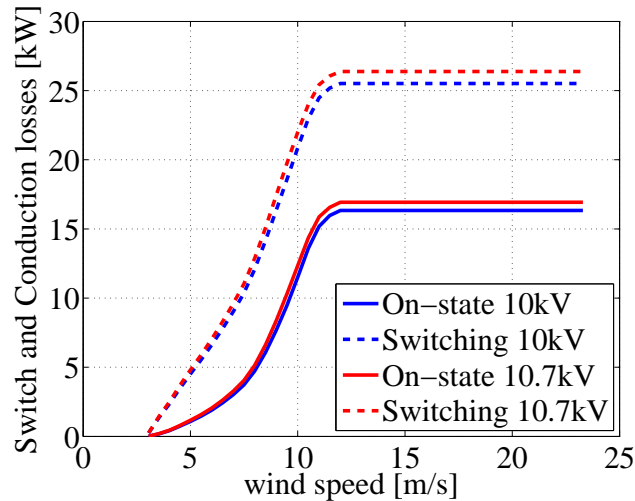
Figure 6.2: On-state and switching losses for 3300 V/1500 A module with F_{sw}=0.5 kHz.
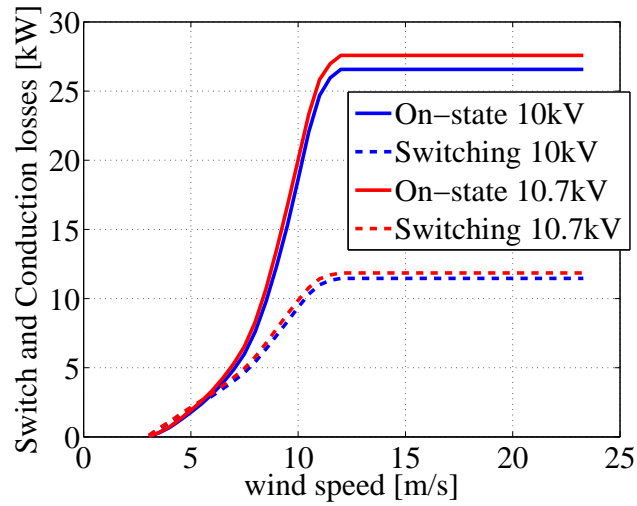
Figure 6.3: On-state and switching losses for 1700 V/2400 A module with F_{sw}=0.5 kHz.

As can be seen in Fig. 6.1 to Fig. 6.3 there is a very strong trend that the switching losses decreases when the phase legs consisting of modules having a lower voltage rating was used. For the 6500 V module the switching losses already at this low switching frequency of 500 Hz, becomes very large. It can also be seen from Fig. 6.1 to Fig. 6.3 that on-state losses increase with a decrease in module voltage rating. In order to compare the converter losses when using the three types of modules, the total converter losses for 10.7 kV is shown in Fig. 6.4. Undoubtedly, the module with the lowest voltage rating is the most favorable one.
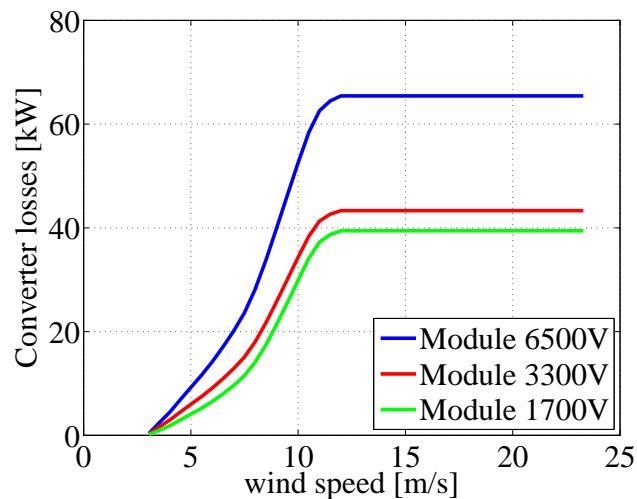
Figure 6.4: Total converter loss for different modules with F_{sw}=0.5 kHz for V_{dc}=10.7 kV.

For the low voltage module (1700 V/2400 A) which has the lowest total losses, higher switching frequencies are also studied, as an example if it is needed to use a higher switch-

ing frequency. In Fig. 6.5 the resulting losses can be observed.
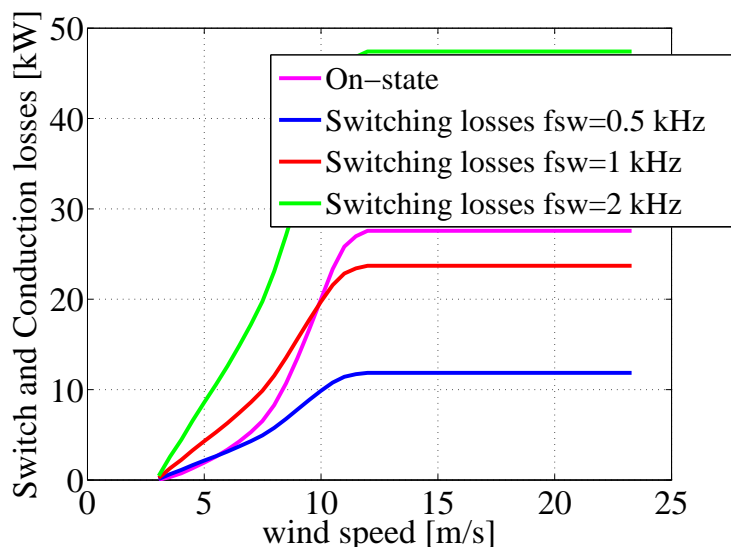
Figure 6.5: On-state and switching losses for V_{dc}=10.7 kV using 1700 V/2400 A module with F_{sw}=0.5, 1 and 2 kHz.

It can be observed from Fig. 6.5, that the switching losses are lower than the on-state losses up to a switching frequency of about 1 kHz. Above that frequency the switching losses are higher than the on-state losses, even for this fairly low voltage module.

6.1.2 Machine losses

As previously mentioned, iron and copper losses have been considered for the machine losses. To calculate the iron losses for different wind speeds, (2.31) is used. In this equation, *k* which is extracted from the iron losses at rated speed, is found to be 0.1. The copper losses are calculated according to (2.28).

The machine losses are shown in Fig. 6.6 and Fig. 6.7. From Fig. 6.7, it can be observed that the machine losses go down with increasing voltage. That is because the current decreases by increasing voltage and hence the copper losses decreases which can also be seen in Fig. 6.6. As can be seen in Fig. 6.6, the iron losses are the same for both dc-link voltages, since here it is assumed that iron losses are entirely dependent on the rotor speed.
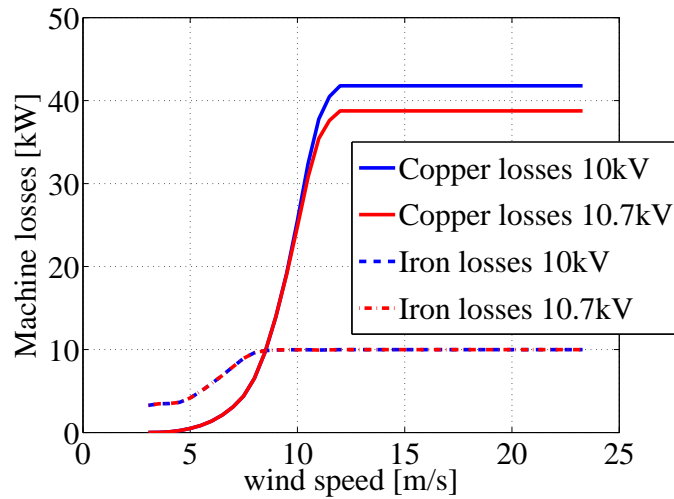
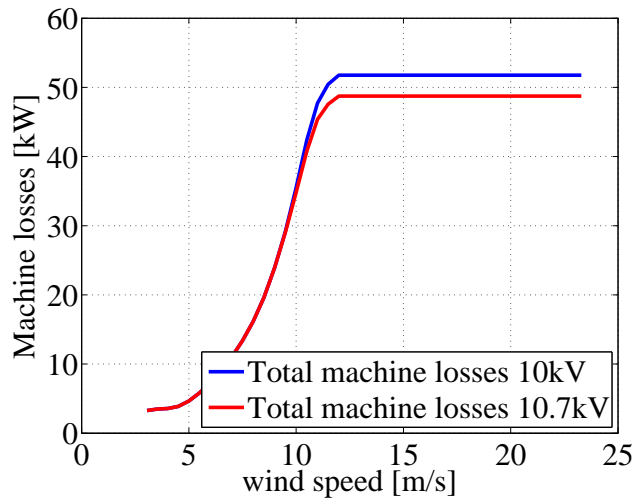Figure 6.6: Copper and iron losses for V_{dc}=10 kV and V_{dc}=10.7 kV.

Figure 6.7: Machine losses for V_{dc}=10 kV and V_{dc}=10.7 kV.

6.1.3 Annual energy efficiency

Figure 6.8 and Fig. 6.9 show the comparison of the system energy efficiency using the three investigated modules for the two different dc-link voltages at 0.5 kHz switching frequency. To plot the annual energy efficiency of the system (4.10) is used. As can be seen in the figures, the 1.7 kV module has higher energy efficiency for both of the voltages. Figure 6.10 shows that the results are the same for a higher switching frequency. This means that the 1.7 kV module equipped converter has the highest annual energy efficiency.
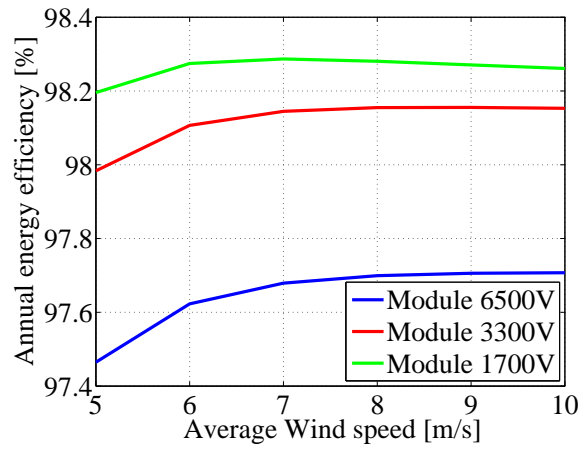
Figure 6.8: Annual energy efficiency for 10 kV dc-link voltage with F_{sw}=0.5 kHz.
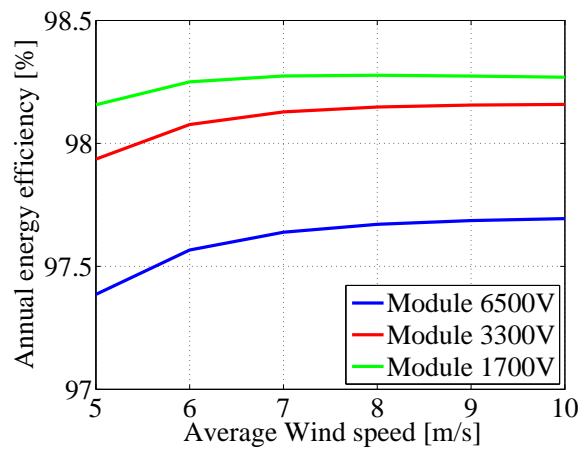
Figure 6.9: Annual energy efficiency for 10.7 kV dc-link voltage with F_{sw}=0.5 kHz.
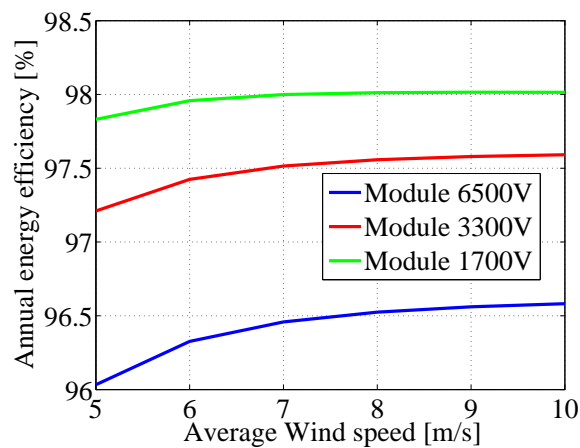

Figure 6.10: Annual energy efficiency for 10.7 kV dc-link voltage with F_{sw}=1 kHz.

6.1.4 Conclusion

It can be concluded that the module with the lowest voltage rating (1.7 kV) gives the best results, both regarding annual efficiency of the system as well as regarding losses at various wind speeds. The dominating factor that makes the 1.7 kV module so beneficial, although it gave the highest conduction losses, is the fact that the switching losses for the converter composed with the high voltage modules had very high switching losses.

6.2 5 MW SPMSG with an IGBT active rectifier

In this section the machine and converter losses as well as annual energy efficiency of the system for a 5 MW wind turbine consisting of a SPMSG designed in Section 5.3 and a 2-level IGBT converter are presented. IGBT modules of a low blocking voltage rating (1.7 kV) are considered to be used in the converter, since it was concluded in Section 6.1 that from the loss point of view this module is the best to use. The results are shown considering both a machine with iron that does not go into saturation, and a non-linear (saturable iron) machine. Three dc-link voltages are studied to find the effect of the dc-link voltage on the losses and efficiency.

6.2.1 Non-saturable machine

Here we are using non-saturable iron. The calculations are done considering $L_d = L_q = 14.5$ mH (taken from Table 5.8 at the lowest wind speed) and the flux linkage $\psi_m = 13.3$ Wb which is the magnet flux at no-load.

6.2.1.1 Operation of the generator

As was mentioned in Section 2.2.5.1, as long as the rotor speed is low and the current is low, there is no problem to operate the generator in MTPA to achieve the desired torques. This means that for all the 3 voltage limits that is considered here ($V_{LLrms} = 4.65\ kV$, $V_{LLrms} = 5.76\ kV$ and $V_{LLrms} = 6.86\ kV$), MTPA operation is possible. This can be seen in Fig. 6.11 where the rotor speed is the lowest operational speed of this turbine. The calculations are done according to (2.18) and (2.19). The colored lines are various torque levels as functions of i_{sd} and i_{sq}. The black curves shows the voltage limits. The inner curve is for the machine voltage $V_{LLrms} = 4.65\ kV$, the outer curve is for the machine voltage $V_{LLrms} = 6.86\ kV$ and the curve in the middle is for the machine voltage $V_{LLrms} = 5.76\ kV$. As can be seen, even with the lowest voltage limit, MTPA operation is possible in the whole operating region, since the MTPA line (green line) is within the voltage limit.
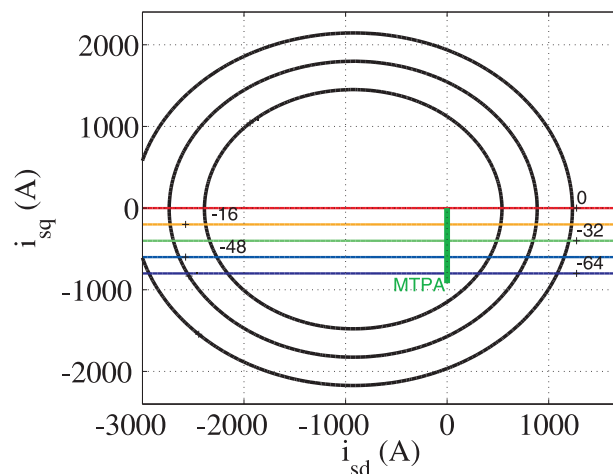
Figure 6.11: Three considered voltage limits, MTPA line and different torques for the linear SPMSG at lowest rotor speed.

As the rotor speed increases, the voltage required to get MTPA is not sufficient from the converter and we need to use field weakening. Figure 6.12 and Fig. 6.13 shows the 3 voltage limits, different torques as well as the MTPA line for this machine at the rated speed. The blue curve ($V_{LLrms} = 4.65\ kV$) is the minimum voltage which gives the desired torque, the red curve ($V_{LLrms} = 6.86\ kV$) is the voltage in which the operation in MTPA is always possible and the black curve ($V_{LLrms} = 5.76\ kV$) is a voltage between the first and second voltages. As can be seen in Fig. 6.13, in this case due to the higher speed compared to Fig. 6.11, for the machine voltage $V_{LLrms} = 5.76\ kV$, it is not possible to work in MTPA operation for the whole operating region. Then we have to follow the yellow line in Fig. 6.13 in order to obtain the desired torque and we now use more current to obtain the desired torque compared to the MTPA case.
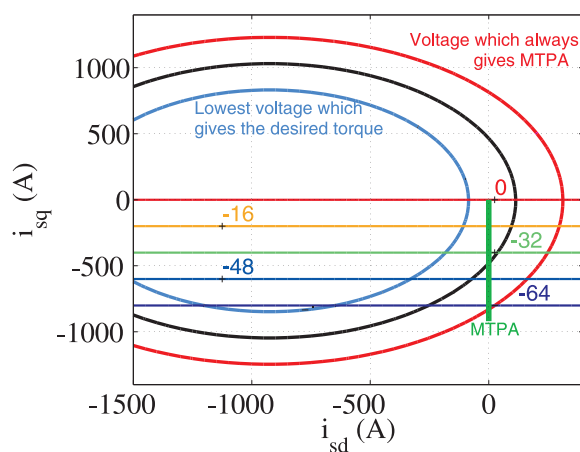

Figure 6.12: Three considered voltage limits, MTPA line and different torques for the linear SPMSG at rated speed.
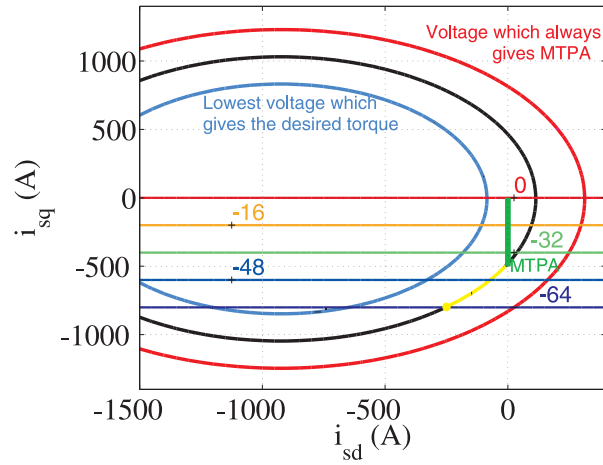
Figure 6.13: Three considered voltage limits, MTPA line and different torques for the linear SPMSG at rated speed. The MTPA operation for the voltage limit in black is not possible for all operating points. The yellow curve shows the field weakening region.

6.2.1.2   DC-link voltage

According to (5.39) the dc-link voltages corresponding to the 3 considered machine voltages ($V_{LLrms} = 4.65\ kV$, $V_{LLrms} = 5.76\ kV$ and $V_{LLrms} = 6.86\ kV$) are 8 kV, 10 kV and 11.8 kV, respectively.

6.2.1.3   Machine losses

As was mentioned in Section 2.4, for the machine losses, copper and iron losses are considered. To calculate the copper loss (2.28) and for the iron loss (2.31) are used where k is 0.13. Figure 6.14 shows the copper and iron losses of the machine for different voltages. As can be seen in the figure, the iron losses are the same for all three different voltages, since as mentioned before, the iron loss is here put to be purely speed dependent. However, the copper losses at higher load decreases with increasing voltage. This is as expected at high power levels, since this is the penalty for the field weakening current at lower available converter voltages.

The total machine losses (sum of copper and iron losses) are shown in Fig. 6.15. As can be seen in the figure, the total machine losses corresponding to the dc-link voltage 8 kV is higher, since the iron losses are the same and the copper losses for the dc-link voltage 8 kV is higher.

6.2.1.4   Converter losses

In Section 6.1 it was shown that from the loss point of view the 1700 V/2400 A IGBT module gives the best results. Therefore, this module is used to build up the converter. To obtain the required voltage and current, a number of series and parallel modules is
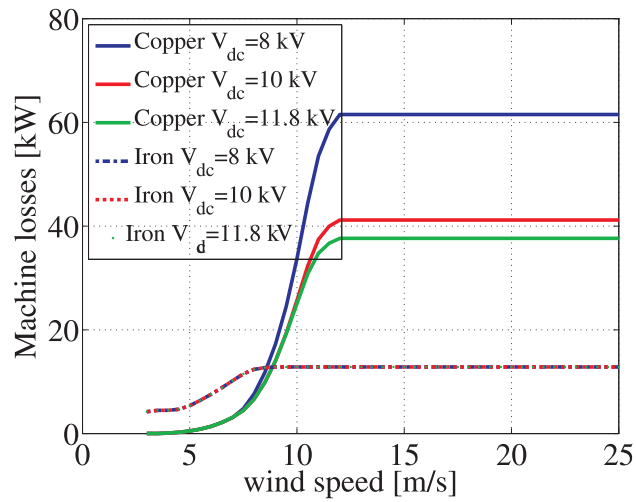
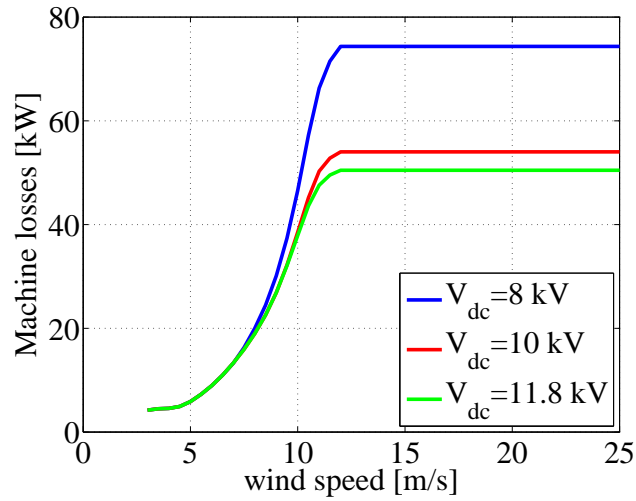Figure 6.14: Machine losses of the SPMSG using a non-saturable iron for different voltages.

Figure 6.15: Total machine losses of the SPMSG using a non-saturable iron for different voltages.

needed. To be as accurate as possible a non-integer (fractional) number of series and parallel modules is used. The number of parallel modules can be obtained from (3.7) and the number of modules in series from (5.40) where V_{ref} for the investigated module is 900 V and the dc-link voltages are given in 6.2.1.2.

To achieve an 8 kV dc-link voltage, the number of series modules are 9 and the number of parallel modules are 0.6. To achieve a 10 kV dc-link voltage, the number of series modules are 11 and the number of parallel modules are 0.5 and to achieve an 11.8 kV dc-link voltage, the number of series modules are 13.1 and the number of parallel modules are 0.47.

The investigated converter losses consist of conduction (on-state) losses for the IGBT and diode as well as switching losses, as was mentioned in section 3.2.1. Figure 6.16 shows the conduction and switching losses for different dc-link voltages using a 500 Hz switching frequency. As can be seen, both the on-state and the switching losses are higher for a higher dc-link voltage.
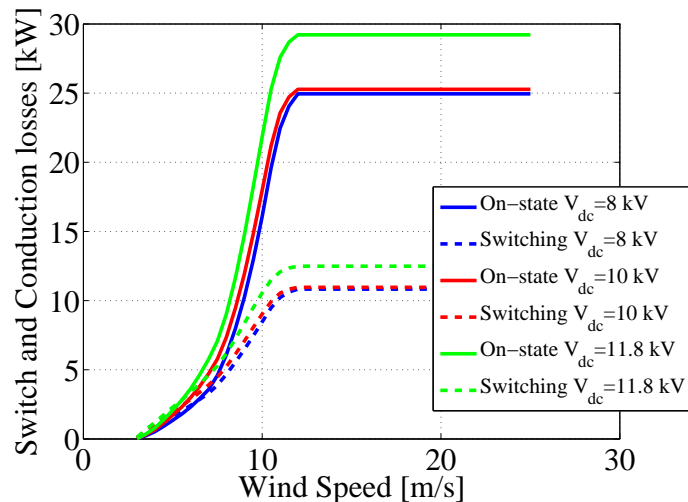

Figure 6.16: Conduction and switching losses for different dc-link voltages for a wind turbine consisting of a SPMSG with non-saturable iron, switching frequency=500 Hz.

Figure 6.17 shows the converter losses for a switching frequency of 2 kHz if a higher switching frequency is needed. As can be seen from the figure, the switching losses increases by increasing the switching frequency, which is as expected. From Fig. 6.16 and Fig. 6.17 it can be observed that if the switching frequency is 500 Hz, the dominant converter loss is the conduction loss while for a switching frequency of 2 kHz the switching loss is higher compared to the conduction loss.
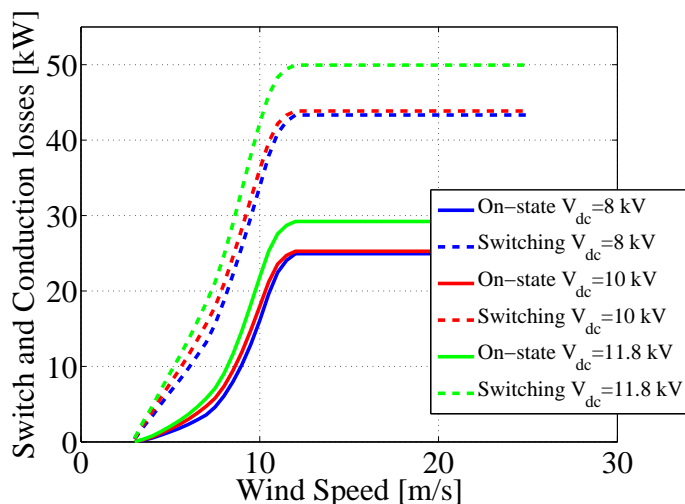
Figure 6.17: Conduction and switching losses for different dc-link voltages for a wind turbine consisting of a SPMSG with non-saturable iron, switching frequency=2 kHz.

The total converter losses (sum of conduction and switching losses) for a switching frequency of 500 Hz and 2 kHz are shown in Fig. 6.18 and Fig. 6.19, respectively. As can be seen in Fig. 6.15, Fig. 6.18 and Fig. 6.19, if the switching frequency is 500 Hz, the share of the machine losses of the total losses is higher than the converter losses for all the dc-link voltages. However, as the dc-link voltage increases, the difference between the machine and converter losses decreases, since the copper losses decrease. For a switching frequency of 2 kHz, the share of the machine and converter losses for the lowest dc-link voltage is almost the same (machine losses are still a bit higher compared to converter losses), while for higher dc-link voltages, converter losses are higher compared to the machine losses.
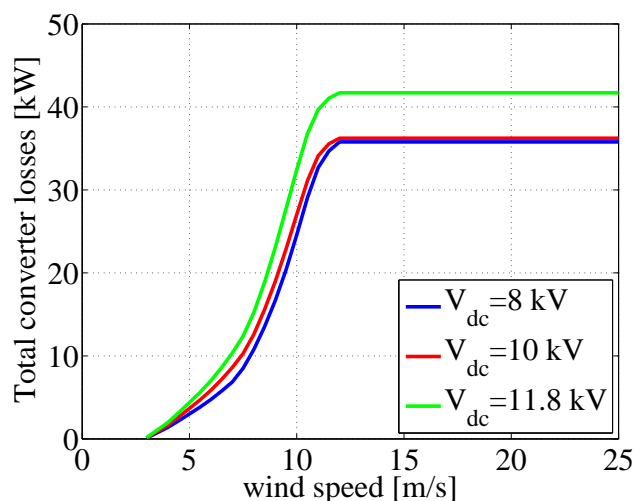

Figure 6.18: Total converter losses for different dc-link voltages for a wind turbine consisting of a SPMSG with non-saturable iron, switching frequency=500 Hz.
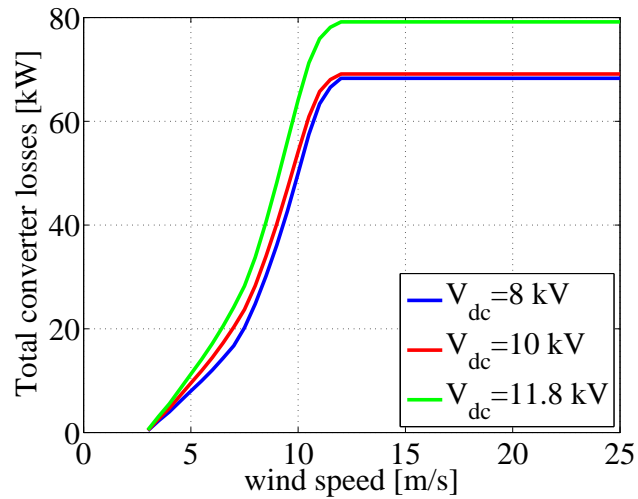
Figure 6.19: Total converter losses for different dc-link voltages for a wind turbine consisting of a SPMSG with non-saturable iron, switching frequency=2 kHz.

6.2.1.5 Total losses

Figure 6.20 and Fig. 6.21 show machine and converter losses for different dc-link voltages using 500 Hz and 2 kHz switching frequency. From these figures the share of machine and converter losses which was discussed in the previous section can also be observed.
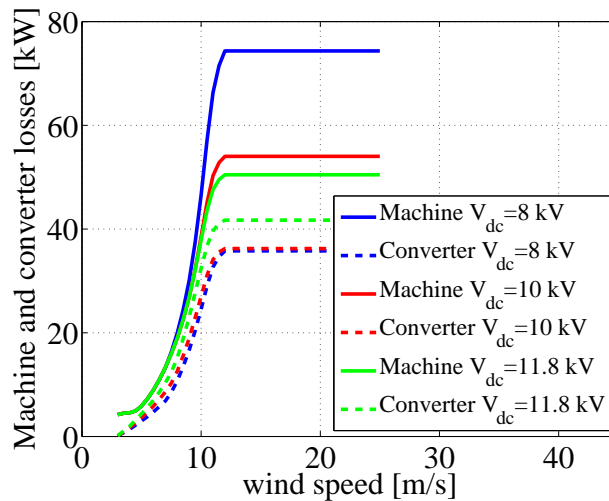

Figure 6.20: Machine and converter losses for different dc-link voltages for a wind turbine consisting of a SPMSG with non-saturable iron, switching frequency=500 Hz.
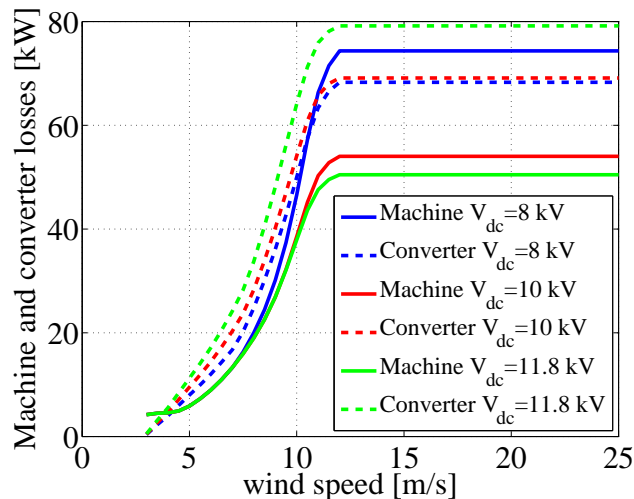
Figure 6.21: Machine and converter losses for different dc-link voltages for a wind turbine consisting of a SPMSG with non-saturable iron, switching frequency=2 kHz.

The total losses (sum of the machine and converter losses) for switching frequencies of 500 Hz and 2 kHz are shown in Fig. 6.22 and Fig. 6.23. As can be seen from the figures, the dc-link voltage 10 kV has the lowest total losses for both switching frequencies at rated wind speed and higher.
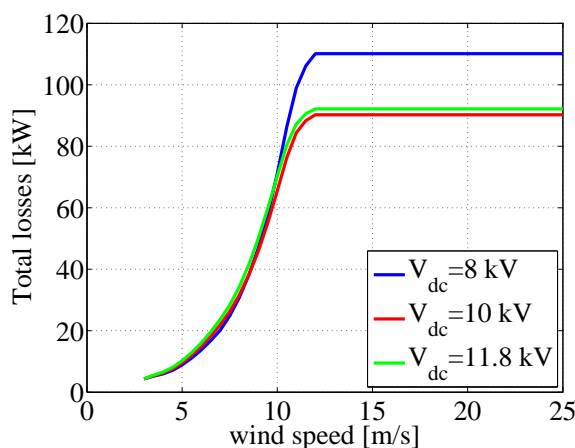

Figure 6.22: Total losses for different dc-link voltages for a wind turbine consisting of a SPMSG with non-saturable iron, switching frequency=500 Hz.

6.2.1.6 Annual energy efficiency

In order to calculate the annual energy efficiency of the drive system (4.10) is used. The annual energy efficiency is shown in Fig. 6.24 considering a switching frequency of 500 Hz.
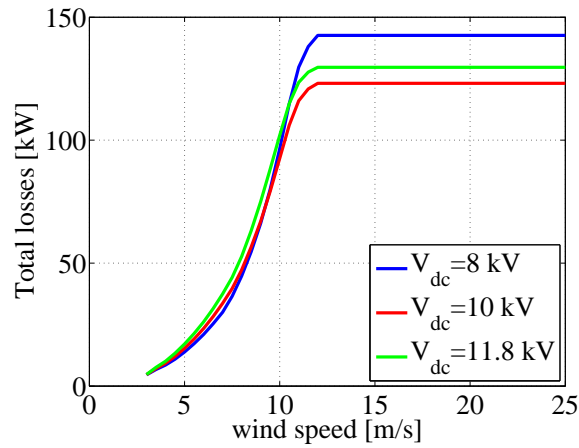
Figure 6.23: Total losses for different dc-link voltages for a wind turbine consisting of a SPMSG with non-saturable iron, switching frequency=2 kHz.
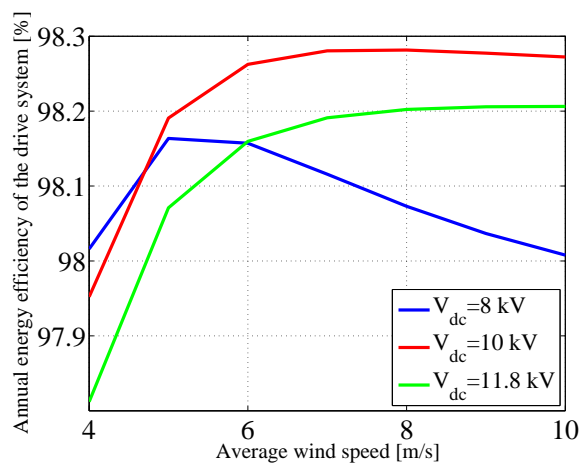

Figure 6.24: Annual energy efficiency of the drive system for different dc-link voltages for a wind turbine consisting of a SPMSG with non-saturable iron, switching frequency=500 Hz.

Figure 6.24 shows that the dc-link voltage of 10 kV gives the highest annual energy efficiency of the system if the average wind speed is higher than 4.7 m/s. If the average wind speed of a site is higher than 6 m/s then the lowest annual efficiency belongs to a dc-link voltage of 8 kV. However, for an average wind speed lower than 6 m/s the dc-link voltage of 11.8 kV gives the lowest annual energy efficiency.

6.2.2 Machine with saturable iron

As was mentioned in Section 5.3.9.3 the d- and q- axis inductances and Ψ_m at the rated speed becomes lower than the values used in section 6.2.1 because of the saturation. In this section the saturated values of L_d, L_q and Ψ_m for the SPMSG from Table 5.8 is used

for the calculation.

6.2.2.1 Operation of the generator

As in Section 6.2.1.1, three voltage limits are considered. The minimum voltage ($V_{LLrms} = 4.1\ kV$) which gives the desired torque (63.7 kN.m) at rated wind speed, the voltage in which the operation using MTPA is always possible ($V_{LLrms} = 6.14\ kV$) and a voltage in between ($V_{LLrms} = 5.12\ kV$). These voltages are lower compared to the linear machine case. This is because voltage is proportional to flux linkage and when the machine goes into saturation, the flux linkage decreases (it can also be seen in Table 5.8). Therefore, the voltage is lower when a machine gets saturated. Figure 6.25 shows these three voltages, the MTPA line and the rated torque of the generator at rated speed.
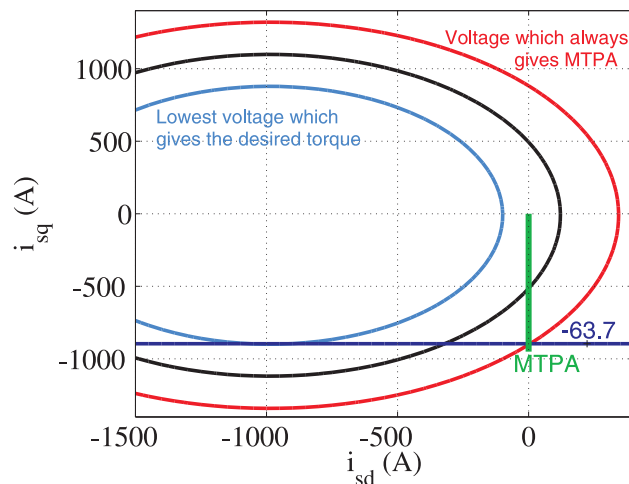

Figure 6.25: Three considered voltage limits, MTPA line and different torques for the non-linear SPMSG at rated speed.

As was shown before, for the lowest and medium voltages, field weakening is necessary after a specific wind speed. When $V_{LLrms} = 4.1\ kV$, the MTPA operation is possible up to the wind speed of roughly 6.2 m/s and for $V_{LLrms} = 5.12\ kV$ up to 7.7 m/s. For voltage $V_{LLrms} = 5.12\ kV$, this is shown in Fig. 6.26. The field weakening region is shown with the yellow line.
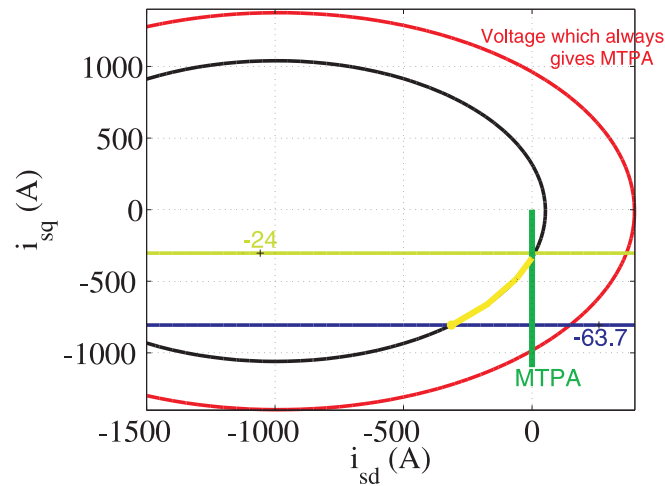
Figure 6.26: Two of the voltage limits and the MTPA line for the non-linear SPMSG at a wind speed of 7.7 ms. The MTPA operation for the voltage limit in black is not possible for all operating points. The yellow line shows the filed weakening path.

6.2.2.2 DC-link voltage

According to (5.39) the dc-link voltages corresponding to the 3 considered machine voltages ($V_{LLrms} = 4.1 \ kV$, $V_{LLrms} = 5.12 \ kV$ and $V_{LLrms} = 6.14 \ kV$) are 7 kV, 8.8 kV and 10.56 kV, respectively.

6.2.2.3 Machine losses

To calculate the copper loss (2.28) is used and the value of iron loss is taken from Maxwell for each operating point.

Figure 6.27 shows the copper and iron losses of the machine for different voltages. As can be seen in the figure, the iron losses increase as the the the dc-link voltage increases. That is because flux is proportional to voltage and iron loss is proportional to flux. Therefore, as for higher dc-link voltages the flux increases, the iron losses increase as well. However, the copper losses increases dramatically for the lowest dc-link voltage, since due to field weakening at lower dc-link voltage, the current is high.
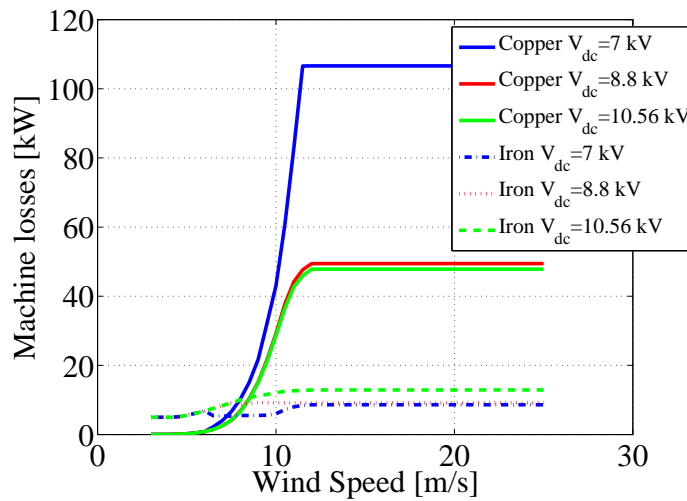
Figure 6.27: Machine losses of the SPMSG using a saturable iron for different voltages.

The total machine losses (sum of the copper and iron losses) are shown in Fig. 6.28. It can be seen that even though the copper losses of $V_{dc} = 8.8 \ kV$ is higher than when $V_{dc} = 10.56 \ kV$, because of the lower iron losses for this dc-link voltage the total machine losses for $V_{dc} = 8.8 \ kV$ is slightly lower than the total machine loss for $V_{dc} = 10.56 \ kV$.
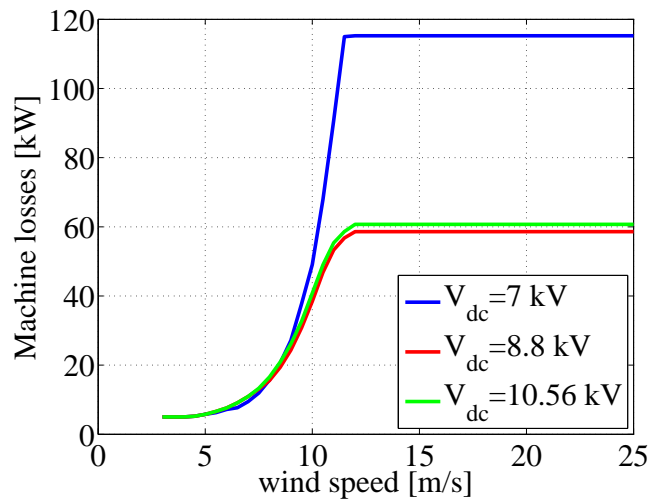

Figure 6.28: Total machine losses of the SPMSG using a saturable iron for different voltages.

6.2.2.4 Converter losses

In the same way as for the linear machine, the 1700 V/2400 A IGBT module is selected to build up the converter. To obtain the required voltage and current ratings, a number of series and parallel modules are needed. This time an integer number of series and parallel modules are used. The number of series and parallel modules for different voltages are:

For $V_{dc} = 7 \ kV$, 8 number of series and 1 number of parallel modules are used. For $V_{dc} = 8.8 \ kV$, 10 number of series and 1 number of parallel modules and for $V_{dc} = 10.56 \ kV$, 12 number of series and 1 number of parallel modules are used.

Figure 6.29 shows the conduction and switching losses for different dc-link voltages using 500 Hz switching frequency. Figure 6.30 shows the converter losses for a switching frequency of 2 kHz, in case a higher switching frequency is needed. As can be seen from the figure, the switching losses increase when the switching frequency goes up.
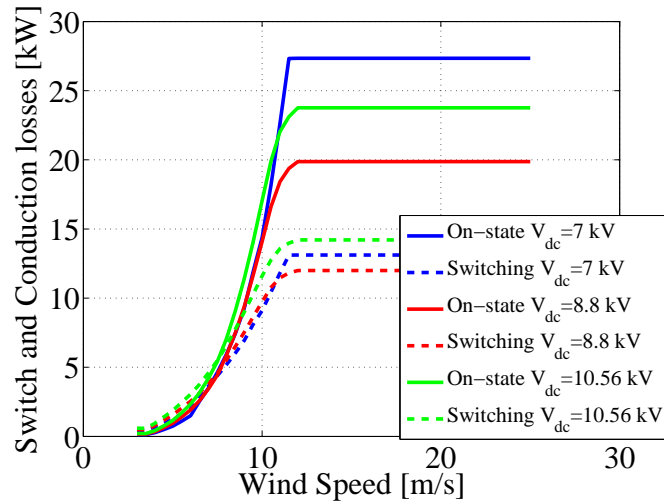

Figure 6.29: Conduction and switching losses of the wind turbine consisting of the SPMSG using a saturable iron for different dc-link voltages, switching frequency=500 Hz.
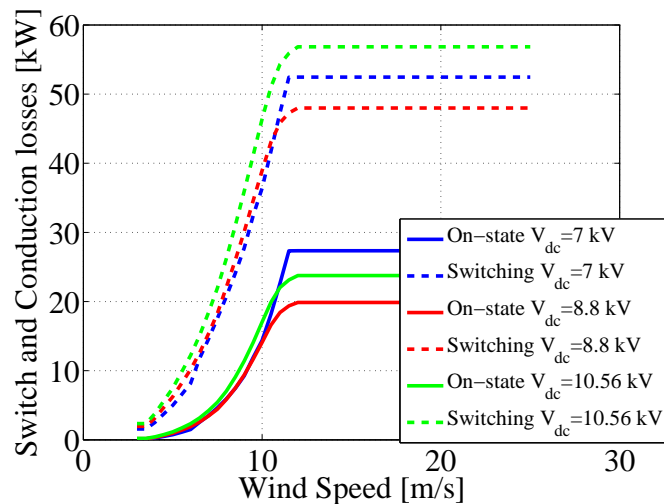

Figure 6.30: Conduction and switching losses of the wind turbine consisting of the SPMSG using a saturable iron for different dc-link voltages, switching frequency=2 kHz.

The total converter losses (sum of the conduction and switching losses) for a switching

frequency of 500 Hz and 2 kHz are shown in Fig. 6.31 and Fig. 6.32, respectively. As can be seen from the figures, the dc-link voltage of 8.8 kV has lower converter losses at the rated wind speed and higher for both the switching frequencies.
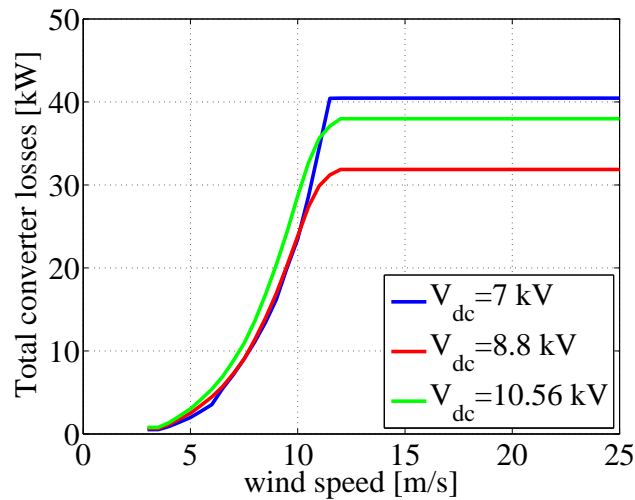

Figure 6.31: Total converter losses of the wind turbine consisting of the SPMSG using a saturable iron for different dc-link voltages, switching frequency=500 Hz.

Figure 6.32: Total converter losses of the wind turbine consisting of the SPMSG using a saturable iron for different dc-link voltages, switching frequency=2 kHz.

6.2.2.5 Total losses

The total losses (sum of machine and converter losses) for switching frequencies of 500 Hz and 2 kHz are shown in Fig. 6.33 and Fig. 6.34. As can be seen from the figures, the dc-link voltage of 8.8 kV has the lowest total losses for both switching frequencies at

rated wind speed and higher. This result was the same for the SPMSG with non-saturable iron. The losses for the dc-link voltage of 7 kV is distinctly higher than for the other two dc-link voltages. The reason is that for this voltage the current is very high due to field weakening.

Figure 6.33: Total losses of the wind turbine consisting of the SPMSG using a saturable iron for different dc-link voltages, switching frequency=500 Hz.
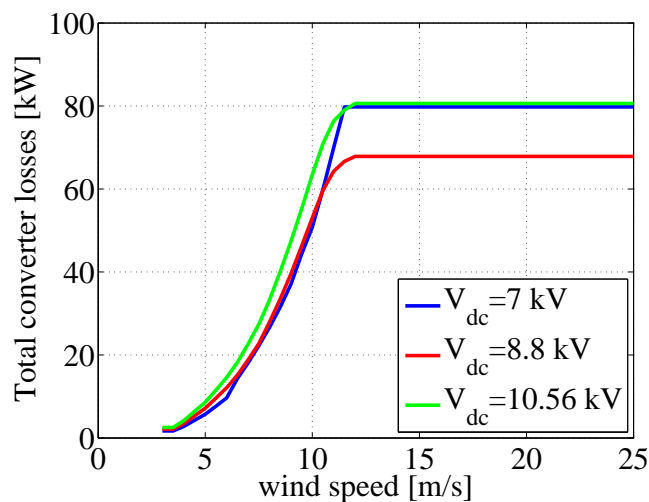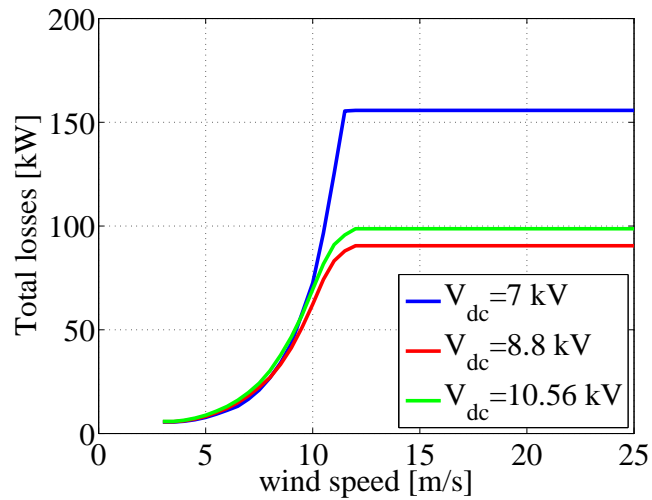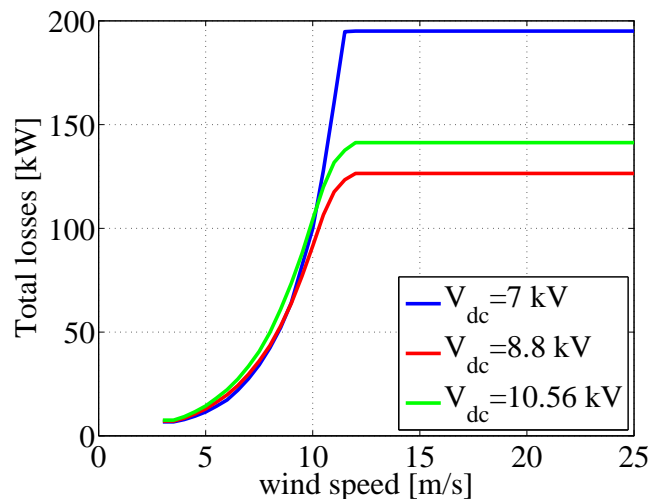

Figure 6.34: Total losses of the wind turbine consisting of the SPMSG using a saturable iron for different dc-link voltages, switching frequency=2 kHz.

6.2.2.6 Annual energy efficiency

The annual energy efficiency of the drive system is calculated using (4.10). The annual energy efficiency is shown in Fig. 6.35 and Fig. 6.36 considering a switching frequency of 500 Hz and 2 kHz.
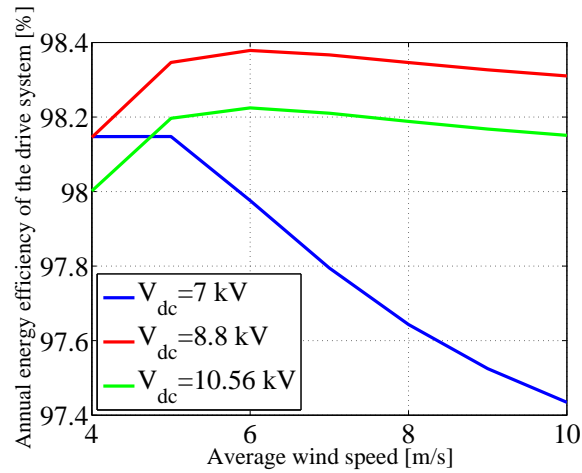
Figure 6.35: Annual energy efficiency of the drive system for the wind turbine consisting of the SPMSG using a saturable iron for different dc-link voltages, switching frequency=500 Hz.
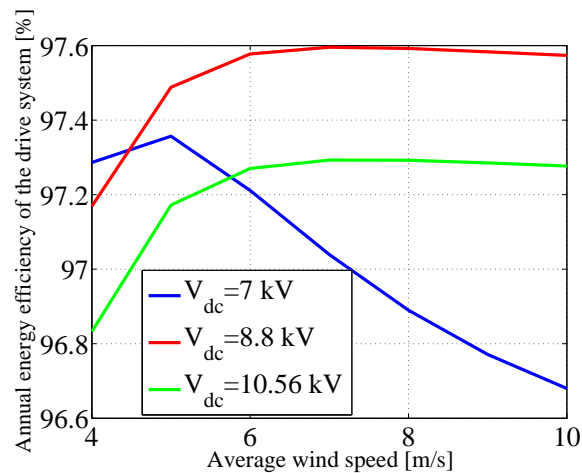
Figure 6.36: Annual energy efficiency of the drive system for the wind turbine consisting of the SPMSG using a saturable iron for different dc-link voltages, switching frequency=2 kHz.

The results of the annual energy efficiency for the SPMSG with saturated iron is similar to the results of the annual energy efficiency with non-saturated iron. As can be seen from the figures above, the dc-link voltage of 8.8 kV has the highest annual energy efficiency for most the average wind speeds independent of the switching frequency. Moreover, when the average wind speed is low the highest voltage has the lowest annual energy efficiency and for higher average wind speed the lowest dc-link voltage has the lowest annual energy efficiency.

6.2.3 Conclusion

The results of the SPMSG with non-saturated iron is similar to the results of the SPMSG with saturated iron. The dc-link voltage affects the annual energy efficiency of the system. To select the dc-link voltage which gives the highest annual energy efficiency the average wind speed must be considered. For the average wind speed higher than 4.7 m/s, a voltage between the voltage which always gives MTPA and the lowest voltage which gives the desired torque gives the highest annual energy efficiency. If the average wind speed is lower than 4-4.7 m/s (depending on the switching frequency of the converter), the lowest voltage which gives the desired torque gives the highest annual energy efficiency.

6.3 5 MW SPMSG with a diode rectifier

In this section, it is shown how much power that can be transferred if a SPMSG is connected to a diode rectifier instead of an IGBT active rectifier. To investigate this issue, as was explained in Section 5.10, a SPMSG is connected to a DC voltage source (it is assumed that the dc-link voltage is constant for a constant wind speed) through an ideal diode rectifier (the voltage drop through the diode is neglected). Simplorer is used for this simulation.

6.3.1 Power transferred versus dc-link voltage

The simulation shows that the electrical power is dependent on the dc-link voltage. The relation between the power and dc-link voltage is shown in Fig. 6.37. As can be seen, the maximum transmitted power is at dc-link voltage 4100 V where the output power of the generator is only about half of the generator power.
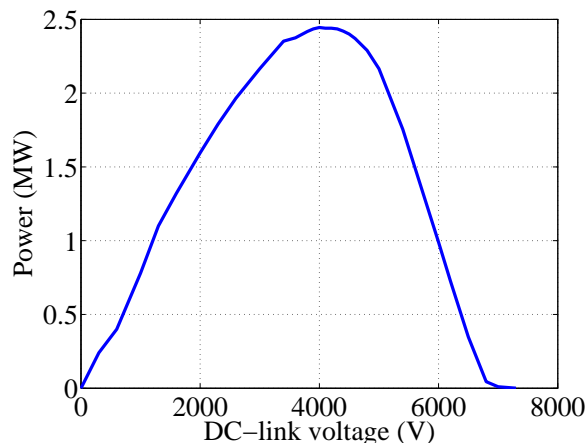

Figure 6.37: Output power of the diode-rectifier-equipped SPMSG as function of dc-link voltage, at maximum rotor speed.

The extraction of 5 MW power from this generator connected to the diode rectifier is not possible. Therefore, the series and shunt capacitor compensation is needed. The possibilities in this respect are explored in [71].

6.4   Performance comparison of the SPMSG and IPMSG

Here a performance comparison of the SPMSG and the IPMSG is presented. As was mentioned in Section 5.4, the same amount of magnets and copper and almost the same amount of iron has been used for these two machines. The machines are considered to be working in the linear region. It is assumed that the results of this comparison with non-saturable iron will yield similar results as a comparison with saturable iron, since it was shown in Section 6.2 that the results from the saturable and non-saturable SPMSG are similar. Two different rated voltages have been used. The first voltage is the voltage that gives MTPA operation for the whole operation region of the SPMSG which is $V_{LLrms} = 6.86\ kV$, and the second voltage, $V_{LLrms} = 4.65\ kV$, is just a bit higher than the lowest possible voltage for which the desired torque is reachable for both machines. The reason that the voltage which gives MTPA operation of the SPMSG is selected is that the voltage which gives MTPA operation for the IPMSG is higher and with that voltage there is no problem for the SPMSG to operate in MTPA. The SPMSG used in this section is the same machine which was designed in Section 5.3 with a non-saturable iron (the same machine that was used in Section 6.2.1) with $L_d = L_q = 14.5$ mH and the flux linkage $\psi_m = 13.3$ Wb. The IPMSG is the machine that was designed in Section 5.4 with a non-saturable iron with parameters $L_d = 17$ mH, $L_q = 54$ mH (taken from RMxprt given in Table 5.12) and $\psi_m = 13.9$ Wb which is the magnet flux at no-load.

6.4.1   Operation of the generator

Figures 6.38 and 6.39 demonstrate the resulting operational characteristics for the rated speed as a function of currents in d- and q-axis, using the different voltages and resulting current levels as well as torque lines. Voltage limit, $V_{LLrms} = 4.65kV$ is shown in blue (the inner curve) and $V_{LLrms} = 6.86kV$ (the outer curve) is in red.

A key conclusion is, as can be seen from Fig. 6.38 and Fig. 6.39, that the SPMSG needs higher current for the same voltages. The consequence is higher copper losses for the SPMSG.

6.4.2   DC-link voltage

According to (5.39) the dc-link voltages corresponding to the selected generator voltages ($V_{LLrms} = 4.65kV$ and $V_{LLrms} = 6.86kV$) are 8 and 11.8 kV.

Figure 6.38: Colored curves, various torque levels as function of i_{sd} and i_{sq}, as well as two lines showing the two voltage limits for SPMSG. The inner line is for machine voltage $V_{LLrms} = 4.65\ kV$ and the outer line is for the voltage $V_{LLrms} = 6.86\ kV$. The green line is the MTPA line. This figure is drawn from the calculations which are done for the rated operational rotor speed for this wind turbine.
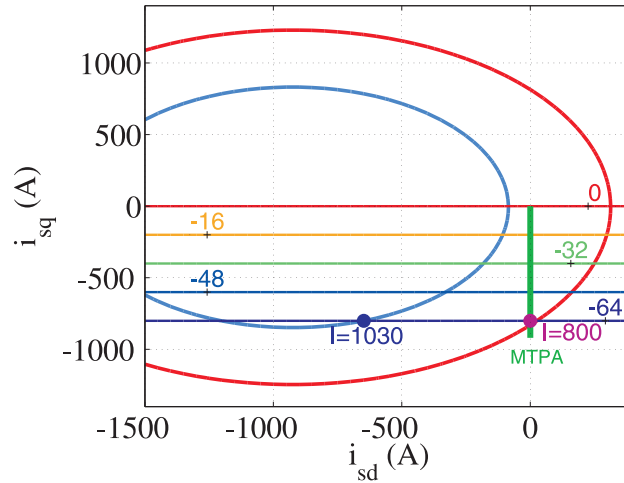

Figure 6.39: Colored curves, various torque levels as function of i_{sd} and i_{sq}, as well as two lines showing the two voltage limits for IPMSG. The inner curve is for machine voltage $V_{LLrms} = 4.65\ kV$ and the outer curve is for the voltage $V_{LLrms} = 6.86\ kV$. The green line is the MTPA line. This figure is drawn from the calculations which are done for the rated operational rotor speed for this wind turbine.
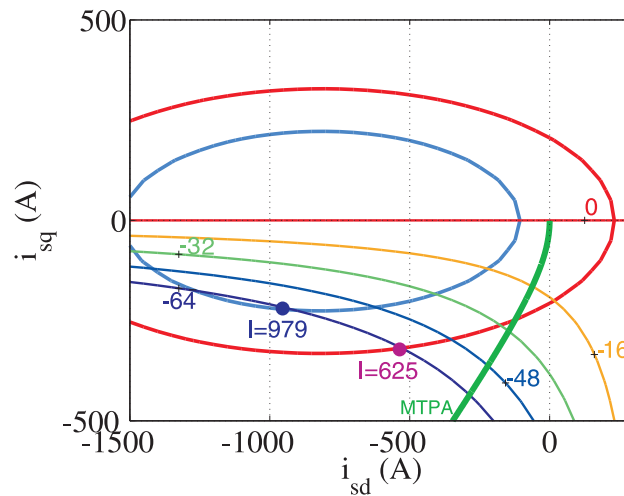
6.4.3 Machine losses

As mentioned in the previous section, the voltage $V_{LLrms} = 6.86\ kV$ is the voltage which gives MTPA operation in the whole operation region for the SPMSG. The peak value of the rated current for this voltage is, 800 A and 625 A for the SPMSG and IPMSG, respectively and the peak value of the rated current for the generator voltage $V_{LLrms} = 4.65\ kV$ is 1030 A for the SPMSG and 979 A for the IPMSG. The copper and iron losses are calculated according to (2.28) and (2.31) where k is 0.13 for the SPMSG and 0.132 for the IPMSG. Copper and iron losses for the lower voltage ($V_{LLrms} = 4.65\ kV$) are shown in Fig. 6.40 and the total machine losses (sum of copper and iron losses) for the maximum ac machine voltage ($V_{LLrms} = 6.86\ kV$) are shown in Fig. 6.41.
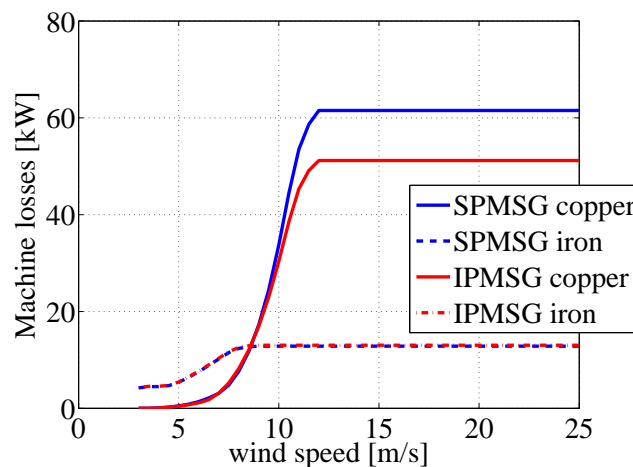

Figure 6.40: Machine losses for SPMSG and IPMSG for machine voltage $V_{LLrms} = 4.65\ kV$.

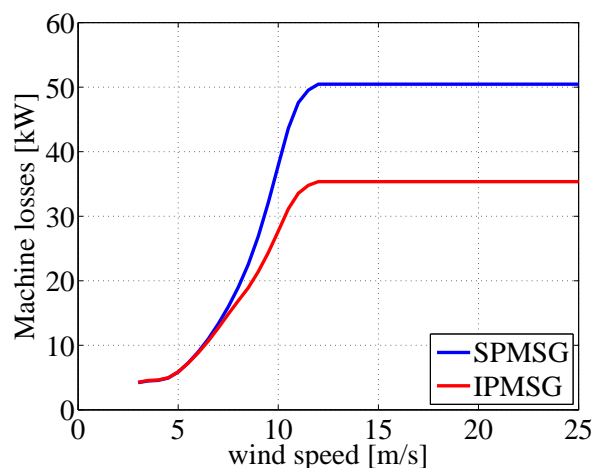Figure 6.41: Total machine losses for SPMSG and IPMSG for machine voltage $V_{LLrms} = 6.86\ kV$.

As expected, it can be seen in Fig. 6.41 that the IPMSG has lower machine losses, which is a consequence of the lower current needed for the same torque level.

6.4.4 Converter losses

The converter losses for the dc-link voltage of 11.8 kV are shown in Fig. 6.42 for a switching frequency of 500 Hz. Figure 6.42 shows that the converter losses when operating the IPMSG are lower, this is valid for both the conduction losses as well as the switching losses.
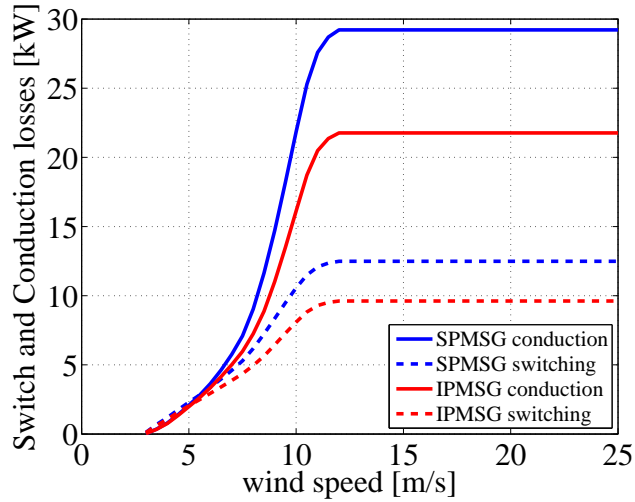
Figure 6.42: Converter losses for SPMSG and IPMSG for machine voltage $V_{LLrms} = 6.86\,kV$ corresponding to dc-link voltage 11.8 kV and switching frequency=0.5 kHz.

6.4.5 Total losses

The total losses (sum of machine and converter losses) are shown in Fig. 6.43, for both the SPMSG and the IPMSG, at the two investigated voltage levels. The better performance of the IPMSG is clearly seen for both the 11.8 kV and the 8 kV dc-link voltage case. The switching frequency is 500 Hz.

6.4.6 Power factor calculation

The voltage angle (Δ) is calculated as

$$\Delta = \tan^{-1}(\frac{u_{sq}}{u_{sd}}) \tag{6.1}$$

where u_{sd} and u_{sq} are taken from (2.18) and (2.19).

Figure 6.43: Total losses for both SPMSG and IPMSG for the switching frequency of 500 Hz.

For lower power levels (which are characterized by a low current and lower rotor speed as well) the current angle (θ) is calculated using the MTPA strategy. However, at a certain power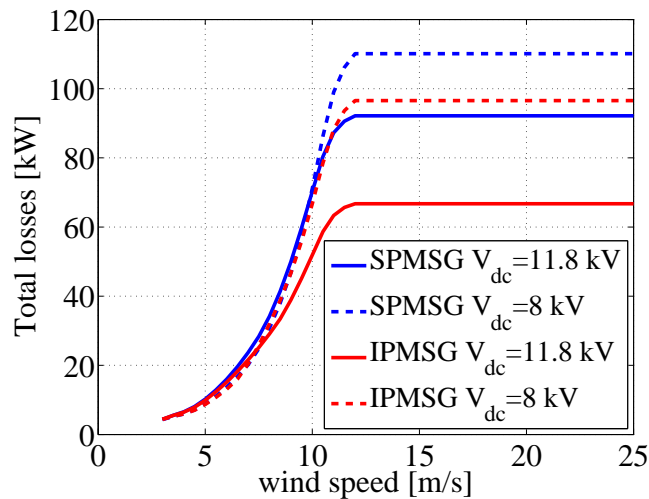 and speed point, the MTPA might not be reachable due to the converter voltage restriction unless a more negative d-axis current is used, which then makes the current angle more negative, until the rated operation of the machine can be reached. Then, the current angle is constant.

Finally the power factor angle (φ) is the difference of the voltage angle and the current angle (6.2) and the power factor is $cos\varphi$.

$$\varphi = \Delta - \theta \tag{6.2}$$

Figure 6.44 shows the voltage, current and power factor angles for the SPMSG. These angles are illustrated for the lower machine voltage which is $V_{LLrms} = 4.65\,kV$. As can be seen in the figure, the current angle is first $-90°$. This is due to the fact that at up to a wind speed of 7 m/s no flux weakening is needed due to a lower rotor speed, and thus a lower induced back-emf. In this region, the current follows the green line in Fig. 6.38. However, from a wind speed of 7 m/s and up, flux weakening is needed, since the machine reaches the rated speed. Consequently, the current angle decreases until the rated operation is achieved. The voltage angle on the other hand, decreases from the beginning, due to that the second term in (2.18) which increases as the speed and current of the generator go up as a function of wind speed.

The voltage, current and power factor angles for the IPMSG are shown in Fig. 6.45. In the same way as for the SPMSG, these angles are also plotted for the lower machine voltage which is $V_{LLrms} = 4.65\,kV$. From the figure it is obvious that the current angle decreases from the beginning due to the MTPA line for an IPMSG (Fig. 6.39). The voltage
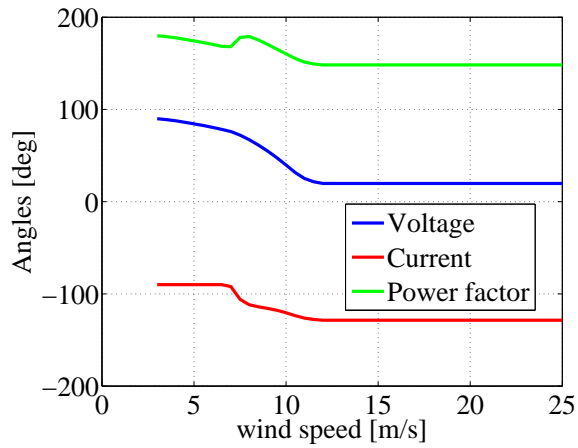
Figure 6.44: Voltage, current and power factor angle for the SPMSG considering $V_{LLrms} = 4.65\ kV$.

angle is decreasing as well, until the machine reaches full power.
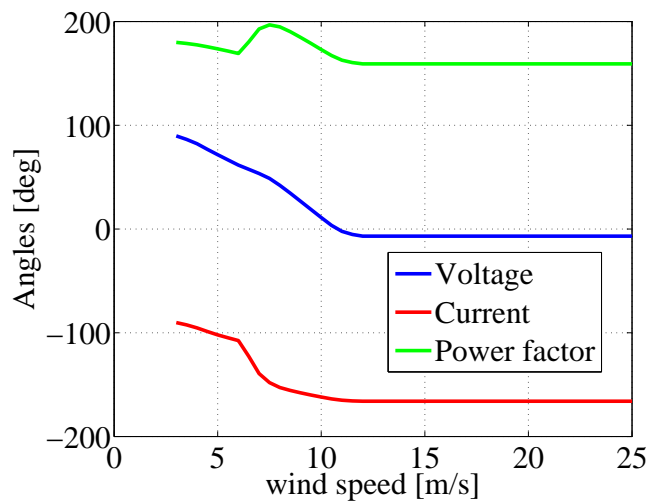
Figure 6.45: Voltage, current and power factor angle for the IPMSG considering $V_{LLrms} = 4.65\ kV$.

The power factor for the SPMSG and the IPMSG is shown in Fig. 6.46. As can be seen in the plot for the rated wind speed, the IPMSG has higher power factor. However, for low wind speeds the SPMSG has a slightly higher power factor regardless of the voltage selection. As can be noted from the figure, the dc-link voltage 11.8 kV with an IPMSG is of a good choice from the power factor point of view, since for a wind speed higher than 10.7 m/s, the power factor is better.

119
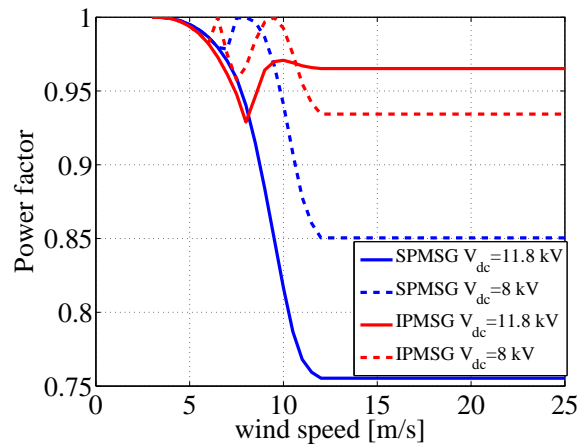
Figure 6.46: Power factor for both SPMSG and IPMSG.

6.4.7 Annual energy efficiency

The annual energy efficiency of the system for the SPMSG and the IPMSG using (4.10) for a switching frequency of 500 Hz and 2 kHz is shown in Fig. 6.47 and Fig. 6.48, respectively. As can be seen from the figures, the IPMSG with the higher voltage has the highest annual energy efficiency for nearly the whole range of the average wind speeds. The SPMSG and the IPMSG with lower voltage have almost the same average energy efficiency for lower average wind speed. However, as the average wind speed increases, the difference between the annual energy efficiency of these two wind turbines increase.

Figure 6.47: Annual energy efficiency of the system for both SPMSG and IPMSG considering two dc-link voltage levels, switching frequency=500 Hz.

Figure 6.48: Annual energy efficiency of the system for both SPMSG and IPMSG considering two dc-link voltage levels, switching frequency=2 kHz.

6.4.8 Conclusion

The results show that if the same amount of material and size is used for a SPMSG and an IPMSG, the annual energy efficiency of the system for the wind turbine with the IPMSG is higher. Also, the power factor at rated wind speed is better for the IPMSG.
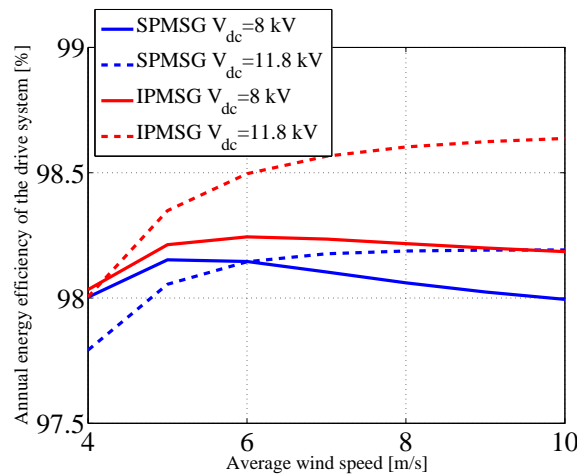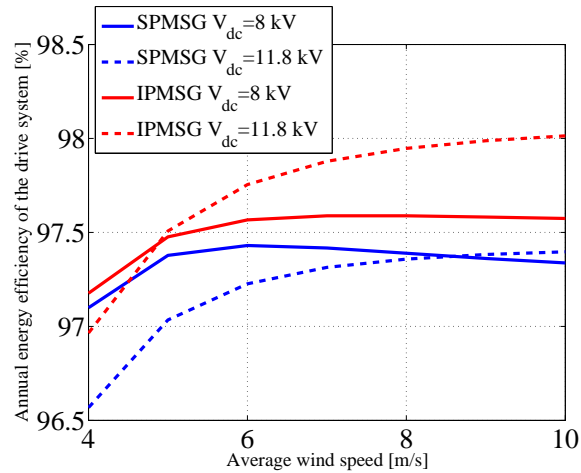
6.5 3.7 MW SynRG with active rectifier

As was mentioned in Section 5.5.1, using the same amount of material as the IPMSG for a SynRG, the SynRG gives 74% of the power of the IPMSG. The power of the IPMSG designed in Section 5.4 is 5 MW. Therefore, the SynRG which has the same physical size as the IPMSG has a power of 3.7 MW. If Fig. 5.3 (which shows the output power of a 5 MW wind turbine versus wind speed) is scaled by 0.74, then the power versus wind speed for a 3.7 MW wind turbine can be plotted as can be seen in Fig. 6.49.

As was described in Section 2.3.4, for unsaturated conditions, the maximum torque is achieved when $\theta = 45\,^\circ$ according to (2.24). Therefore, i_{sd} and i_{sq} are equal. However, when the machine comes into saturation, the MTPA angle will be higher than $\theta = 45\,^\circ$. This machine has saturable iron and for wind speeds higher than 4.5 m/s, it goes into saturation. Therefore, the current angle (θ) increases after a wind speed of 4.5 m/s. The relation of i_{sd} and i_{sq} for this SynRG is shown in Fig. 6.50.

6.5.1 Machine losses

The stator and rotor of this machine is made of the material which was shown in Section 5.3.1. This iron is saturable and hence the d- and q-inductances are different for each operating point. The iron losses for this machine is taken from Maxwell for different
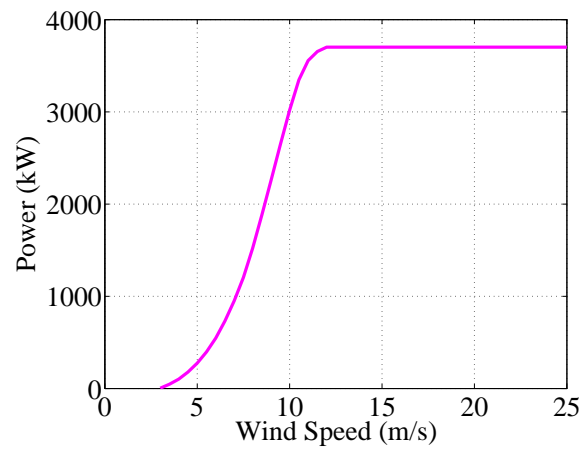
Figure 6.49: Power versus wind speed for the wind turbine consisting of the SynRM.
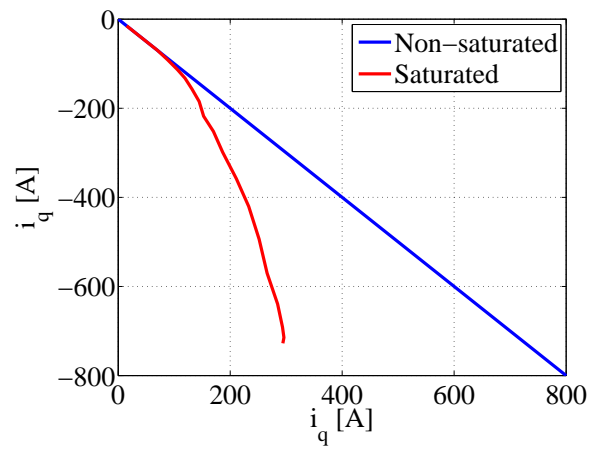
Figure 6.50: The d- and q-current for a SynRG with non-saturated and saturated iron.

operating points. The copper losses are calculated using (2.28) where R_s is the same as the value calculated in (5.15) which is 39.5 mΩ, as this machine has the same stator and winding as the SPMSG. The copper and iron losses for the SynRG with MTPA control strategy is shown in Fig. 6.51.
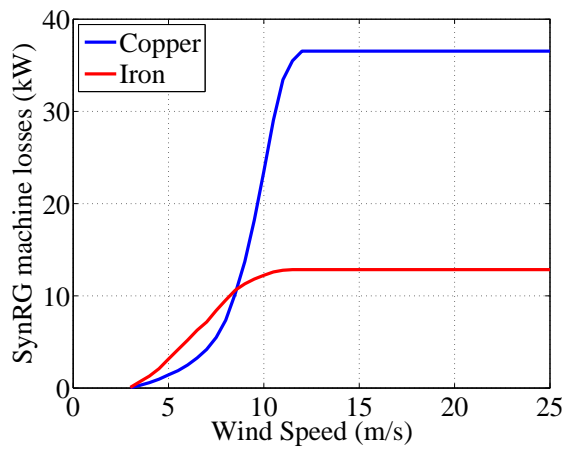
Figure 6.51: Machine losses for the SynRG.

6.5.2 Converter losses

The 1700 V/2400 A IGBT module is used in the converter. To obtain the required voltage and current, a number of series and parallel modules are needed. An integer number of series and parallel modules are used. 12 modules in series are needed to obtain the voltage and 1 module to achieve the current. The switch and conduction losses are shown in Fig. 6.52.
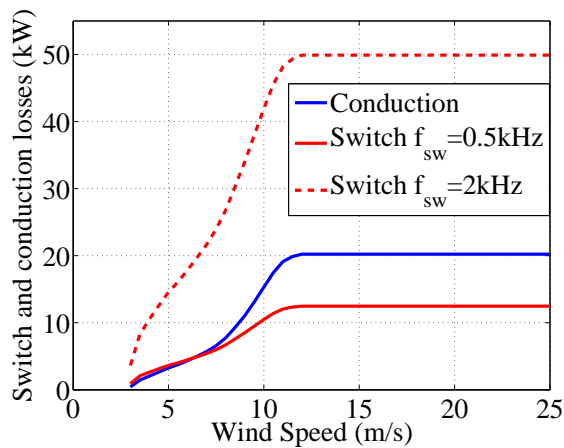
Figure 6.52: Converter losses for the the wind turbine with a SynRG.

As can be seen from the figure, if the switching frequency is low, the conduction losses

are dominant. However, if a higher switching frequency is used the switching losses are more than twice the conduction losses.

6.5.3 Annual energy efficiency

The annual energy efficiency of the system with the SynRG using (4.10) is shown in Fig. 6.53.
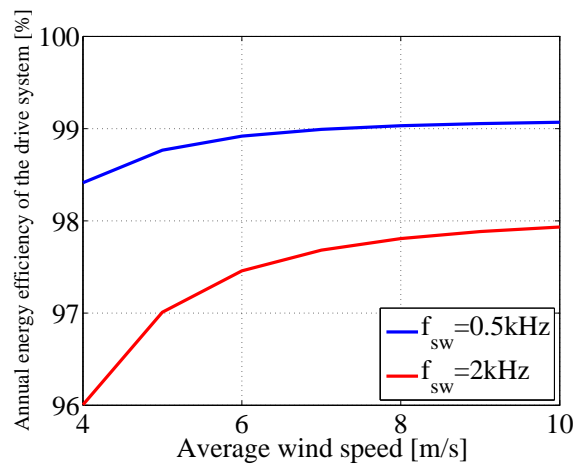
Figure 6.53: Annual energy efficiency for the 3.7 MW wind turbine consisting of a SynRG with two different switching frequencies.

6.6 Comparison of a SynRG and an IPMSG

In this section the machine losses and efficiency of the 5 MW IPMSG and the 3.7 MW SynRG for wind turbine application are shown. MTPA control strategy is used. Both machines have the same amount of material and a saturable iron.

6.6.1 Machine losses

Using MTPA strategy, the machine losses for IPMSG and SynRG are shown in Fig. 6.54 and Fig. 6.55, respectively.
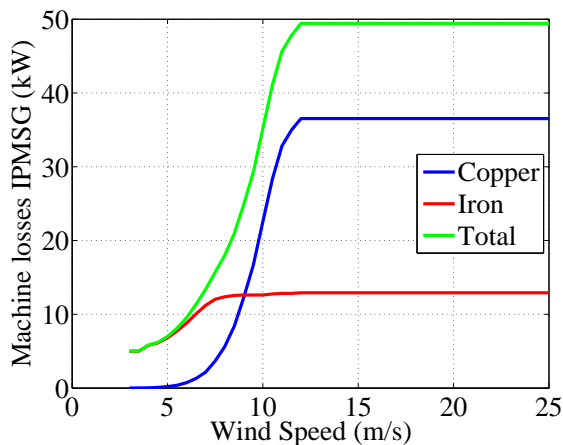
Figure 6.54: Machine losses for IPMSG.
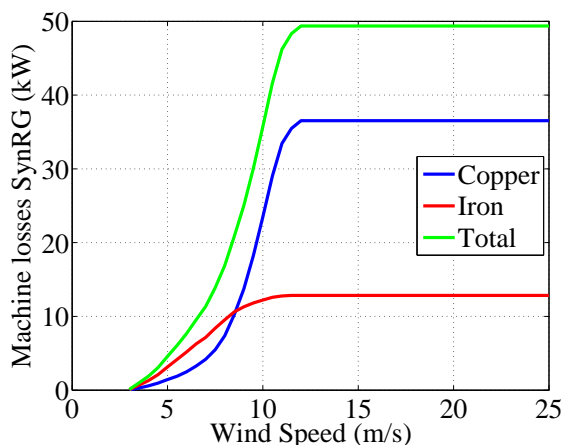
Figure 6.55: Machine losses for SynRG.

As can be seen in the figures, the total losses of the IPMSG and the SynRG at the rated wind speed and higher are equal. it should be kept in mind that the power level of the IPMSG is higher than that of the SynRG. However, the iron losses for the IPMSG at low speed (up to 8 m/s) is higher. This results in higher machine losses at lower wind speeds. The power factor of the machines are shown in Fig. 6.56. As can be seen, the SynRG has a lower power factor for all the operation points.
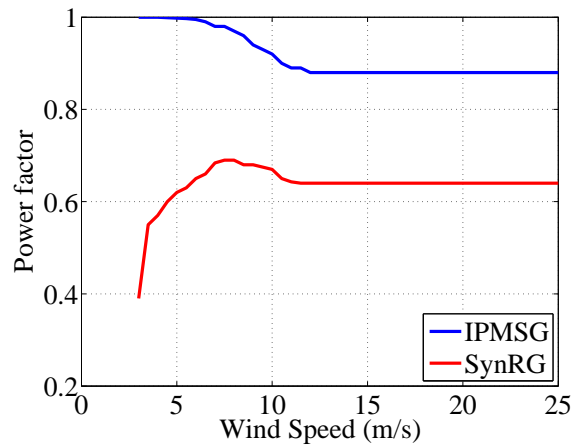
Figure 6.56: Power factor for the IPMSG and the SynRG.

6.6.2 Machine annual energy efficiency

The machine annual energy efficiency of the 5 MW IPMSG and 3.7 MW SynRG is shown in Fig. 6.57.
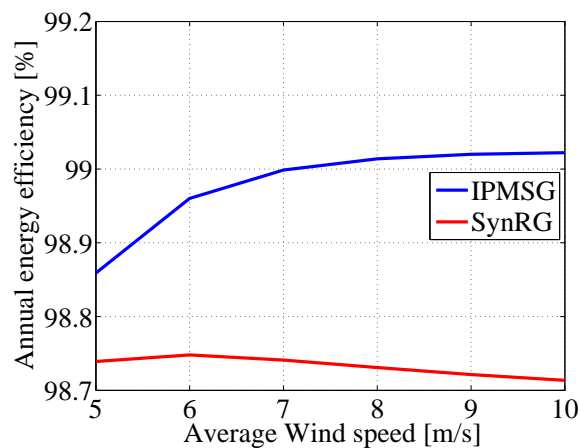
Figure 6.57: Machine annual energy efficiency for the IPMSG and SynRG.

6.6.3 Conclusion

The SynRG designed in this work with the same amount of the material as the IPMSG has 74% of the power of the IPMSG. The total losses of the two machines at the rated wind speed and higher are equal. However, the iron losses of the IPMSG at lower wind speeds (up to 8 m/s) is higher. Therefore, at lower wind speeds the IPMSG has higher losses.

Chapter 7

Conclusions and future work

7.1 Conclusions

In this thesis different generating systems are designed, analyzed and compared to find an energy-efficient generating system for offshore wind turbines.

The electromagnetic design (both with and without saturation effects) of the generators was performed with the use of a finite element program (Maxwell). Some of the machine parameters such as magnetizing and leakage inductances from the simulation are compared to analytical calculation methods for linear cases, showing a reasonable coherence.

It was shown that if a medium voltage generator and an active rectifier with IGBTs are used in the system, from the loss point of view it is best to use a low voltage rating IGBT module (1.7 kV) for the converter, even though more modules are needed to be used in series to achieve the required voltage. The reason that makes the 1.7 kV module beneficial compared to higher voltage modules (3.3 kV and 6.5 kV) is that although the converter composed with low voltage modules has the highest conduction losses, it has substantially lower switching losses.

Three different dc-link voltage levels for a 5 MW wind turbine consisting of a surface permanent magnet generator and an IGBT rectifier were investigated. The annual energy efficiency of the system for the three different voltages was studied. It was found that the efficiency is affected by the choice of the dc-link voltage and in selecting the dc-link voltage the average wind speed of the site should be considered. Furthermore, it was shown that among the three considered dc-link voltages, the dc-link voltage which gives the highest efficiency for the average wind speed of 5 m/s and higher, is the one in between the voltage which gives the maximum torque per ampere operation for the generator and the minimum voltage that gives the desired torque. Similar results were achieved, regarding the dc-link voltage selection, whether the core material of the surface permanent magnet generator was considered to be saturable or non-saturable.

The performance of two wind turbines with the same converter and consisting of per-

manent magnet synchronous generators with the same size and almost the same amount of active material with different placement of the magnets was studied. One generator has the magnets on the surface of the rotor (SPMSG) and the magnet of the other generator is placed inside the rotor (IPMSG). The results show that the power factor of the IPMSG is higher at the rated wind speed compared to the SPMSG. Moreover, the annual energy efficiency of the system comprising the IPMSG is higher.

An IPMSG is compared with a synchronous reluctance generator (SynRG) using the same geometrical dimensions for both generators. It was found that a SynRG can convert 74% of the power that an IPMSG can convert, while it has 80% of the IPMSG weight. The power factor of the IPMSG is higher for all the operating points.

Two methods to reduce the torque ripple of the IPMSG were studied. The first method is skewing the stator and the other method is a fractional slot interior permanent magnet generator (IPMSGFS). The results show that both methods reduce the torque ripple by about 70%, while the torque drop is negligible.

To make a general conclusion about the most energy efficient generating system for HVDC off-shore wind turbines, further investigations are needed as described in the next section about suggested future work. However, according to the investigations done in this work it is indicated that the most suitable system includes an IPMSG with a dc-link voltage between the voltage level that gives maximum torque per ampere operation for the whole operation region and the minimum dc-link voltage level which gives the required rated torque.

7.2   Future work

The speed of the generators that are investigated in this work is 750 rpm. Therefore the wind turbines using these generators need to be equipped with a gearbox. A valuable further effort is to include gearbox losses and weight and put these in relation to those using a generating system with a low speed generator (direct drive).

The number of poles in a generator is an important issue for the performance of the generating system, which can be investigated.

It would also be interesting to calculate permanent magnet loss, in order to see if then the generator topology comparison will give different results, as this will yield higher loss for the permanent magnet generators, compared to the SynRG.

It was shown that the SynRG perhaps could compete with the IPMSG as a wind turbine generator at low average wind speeds. A permanent magnet assisted synchronous reluctance generator can also be a good option for wind turbine applications which should be investigated.

Furthermore, thermal calculation of the generators is an important task. This could for example be used to verify if the assumption of the cooling system according to the current density and electric loading is appropriate. A life cycle cost analysis would be

another important task in order to compare the different systems more in details. Finally, to build a small scale experimental system, in order to verify simulations and investigate practical details, would be of great value.

References

[1] R. Li, S. Bozhko, G. Asher, J. Clare, L. Yao, and C. Sasse, "Grid frequency control design for offshore wind farms with naturally commutated HVDC link connection," in *Industrial Electronics, 2006 IEEE International Symposium on*, vol. 2, july 2006, pp. 1595 –1600.

[2] N. Kirby, L. Xu, M. Luckett, and W. Siepmann, "HVDC transmission for large offshore wind farms," *Power Engineering Journal*, vol. 16, no. 3, pp. 135 –141, june 2002.

[3] T. Ackermann, "Transmission systems for offshore wind farms," *Power Engineering Review, IEEE*, vol. 22, no. 12, pp. 23 –27, dec. 2002.

[4] A. Kiyoumarsi, P. Moallem, M. Hassanzadeh, and M. Moallem, *Finite Elements, Chapter 12, Application of the Finite Element Method in Design and Analysis of Permanent magnet Motors*.   WSEAS Press, August 2007.

[5] F. Libert and J. Soulard, "Design study of different direct-driven permanent-magnet motors for a low speed application," in *Proceedings of the Nordic Workshop on Power and Industrial Electronics (NORpie), Trondheim, Norway, June 2004*.

[6] P. Reddy, A. El-Refaie, K.-K. Huh, J. Tangudu, and T. Jahns, "Comparison of interior and surface pm machines equipped with fractional-slot concentrated windings for hybrid traction applications," in *Energy Conversion Congress and Exposition (ECCE), 2011 IEEE*, 2011, pp. 2252–2259.

[7] H. Haraguchi, S. Morimoto, and M. Sanada, "Suitable design of a pmsg for a large-scale wind power generator," in *Energy Conversion Congress and Exposition, 2009. ECCE 2009. IEEE*, 2009, pp. 2447–2452.

[8] J. Kostko, "Polyphase reaction synchronous motors," *J. Amer. Inst. Elec. Ing.*, vol. 42, pp. 1162–1168, Nov. 1923.

[9] T. Miller, A. Hutton, C. Cossar, and D. Staton, "Design of a synchronous reluctance motor drive," *Industry Applications, IEEE Transactions on*, vol. 27, no. 4, pp. 741 –749, jul/aug 1991.

References

[10] A. Vagati, G. Franceschini, I. Marongiu, and G. Troglia, "Design criteria of high performance synchronous reluctance motors," in *Industry Applications Society Annual Meeting, 1992., Conference Record of the 1992 IEEE*, oct 1992, pp. 66 –73 vol.1.

[11] T. Matsuo and T. Lipo, "Rotor design optimization of synchronous reluctance machine," *Energy Conversion, IEEE Transactions on*, vol. 9, no. 2, pp. 359 –365, jun 1994.

[12] M. Kamper and A. Volsdhenk, "Effect of rotor dimensions and cross magnetisation on Ld and Lq inductances of reluctance synchronous machine with cageless flux barrier rotor," *Electric Power Applications, IEE Proceedings -*, vol. 141, no. 4, pp. 213 –220, jul 1994.

[13] A. Vagati, A. Canova, M. Chiampi, M. Pastorelli, and M. Repetto, "Improvement of synchronous reluctance motor design through finite-element analysis," in *Industry Applications Conference, 1999. Thirty-Fourth IAS Annual Meeting. Conference Record of the 1999 IEEE*, vol. 2, 1999, pp. 862 –871 vol.2.

[14] A. Vagati, M. Pastorelli, and G. Franceschini, "High performance control of synchronous reluctance motor," in *Industry Applications Conference, 1996. Thirty-First IAS Annual Meeting, IAS '96., Conference Record of the 1996 IEEE*, vol. 1, oct 1996, pp. 295 –303 vol.1.

[15] A. Vagati, M. Pastorelli, G. Francheschini, and S. Petrache, "Design of low-torque-ripple synchronous reluctance motors," *Industry Applications, IEEE Transactions on*, vol. 34, no. 4, pp. 758 –765, jul/aug 1998.

[16] R. Moghaddam, "Synchronous reluctance machine (SynRM) in variable speed drives (VSD) applications," Ph.D Thesis, Royal Institute of Technology, School of Electrical Engineering, Stockholm, Sweden, May 2011.

[17] S. Kim, S.-K. Sul, K. Ide, and S. Morimoto, "Maximum efficiency operation of synchronous reluctance machine using signal injection," in *Power Electronics Conference (IPEC), 2010 International*, 2010, pp. 2000–2004.

[18] E. Schmidt, W. Brandl, and C. Grabner, "Design improvement of synchronous reluctance machines with internal rotor flux barriers for high-speed drives," in *Power Electronics Specialists Conference, 2002. pesc 02. 2002 IEEE 33rd Annual*, vol. 4, 2002, pp. 1949–1954.

[19] A. Mohamadein, Y. H. A. Rahim, and A. Al-khalaf, "Steady-state performance of self-excited reluctance generators," *Electric Power Applications, IEE Proceedings B*, vol. 137, no. 5, pp. 293–298, 1990.

132

[20] S. Guha and N. Kar, "Saturation modeling and stability analysis of synchronous reluctance generator," *Energy Conversion, IEEE Transactions on*, vol. 23, no. 3, pp. 814–823, 2008.

[21] S. Tokunaga and K. Kesamaru, "FEM simulation of novel small wind turbine generation system with synchronous reluctance generator," in *Electrical Machines and Systems (ICEMS), 2011 International Conference on*, 2011, pp. 1–6.

[22] K. Kawasaki, T. Fukami, R. Hanaoka, and S. Takata, "Performance analysis of a self-excited synchronous reluctance generator with multiple-barrier rotor," *IEEJ Transactions on Industry Applications*, vol. 126, pp. 788–793, 2006.

[23] B. Andresen and J. Birk, "A high power density converter system for the gamesa G10x 4.5 MW wind turbine," in *Power Electronics and Applications, 2007 European Conference on*, sept. 2007, pp. 1 –8.

[24] B. Backlund and S. Ebner, "The wind power converter for tomorrow is already here," in *EWEA, Brussels, Belgium*, September 2011, pp. 329 –333.

[25] L. Lei, "High power IGBT modules for wind turbine applications," Infineon presentation, March 2009.

[26] E. Lepa, T. Thurnherr, and A. Faulstich, "Design and testing of a 7 MW wind turbine medium voltage electrical drivetrain with medium speed permanent magnet synchronous generator," in EWEA *2013 Europe's premier wind energy event*, 2013, pp. 1–8.

[27] Areva, "M5000 Technical data," Product brochure, 2010. [Online]. Available: http://www.areva-wind.com/fileadmin/infomaterial/AREVAwind_TechnicalData.pdf

[28] ABB, "Offshore but online," broschur data, 2008. [Online]. Available: http://www05.abb.com/global/scot/scot271.nsf/veritydisplay/a548e728678452e4c12574b900365bf0/$file/56-613m813_ENG72dpi.pdf

[29] ABB, "PCS 6000 for large wind turbines," Product brochure, 2011. [Online]. Available: http://www05.abb.com/global/scot/scot232.nsf/veritydisplay/c4de28147e528b0cc1257a8b00595934/$file/PCS6000Wind_3BHS351272_E01_RevA.pdf

[30] P. Roshanfekr, T. Thiringer, and S. Lundmark, "Efficiency comparison of a 5 MW wind turbine PMSG-equipped generating system using various dc-link voltages," in *EVER 12, Monte-Carlo, Monaco*, March 2012.

133

[31] A. Faulstich, J. Stinke, and F. Wittwer, "Medium voltage converter for permanent magnet wind power generators up to 5 MW," in *Power Electronics and Applications, 2005 European Conference on*, 0-0 2005, pp. 9 pp. –P.9.

[32] J. F. Gieras and M. Wing, *Permanent Magnet Motor Technology*.   Marcel Dekker, Inc., 2002.

[33] N. Mohan, T. M. Undeland, and W. P. Robbins, *Power Electronics Converters, Apllications, and design*.   John Wiley & Sons,Inc, 2003.

[34] J. Pyrhönen, T. Jokinen, and V. Hrabovcová, *Design of Rotating Electrical Machines*.   John Wiley & Sons, 2010.

[35] S. Keshavarz, "Design and evaluation of an active rectifier for a 4.1 MW off-shore wind turbine," Master's thesis, 2011, 42.

[36] A. EL-Refaie, "Fractional-slot concentrated-windings synchronous permanent magnet machines: Opportunities and challenges," *Industrial Electronics, IEEE Transactions on*, vol. 57, no. 1, pp. 107–121, 2010.

[37] F. Tahami, H. Nademi, and M. Rezaei, "Maximum torque per ampere control of permanent magnet synchronous motor using genetic algorithm," *TELKOMNIKA (Telecommunication, Computing, Electronics and Control)*, vol. 9, no. 2, 2013. [Online]. Available: http://journal.uad.ac.id/index.php/TELKOMNIKA/article/view/1311

[38] J. Hendershot and T. Miller, *Design of Brushless Permanent-Magnet Machines*. Florida, USA: Motor Design Books LLC, 2010.

[39] T. Jahns, G. Kliman, and T. W. Neumann, "Interior permanent-magnet synchronous motors for adjustable-speed drives," *Industry Applications, IEEE Transactions on*, vol. IA-22, no. 4, pp. 738–747, 1986.

[40] E. Rashad, T. Radwan, and M. Rahman, "A maximum torque per ampere vector control strategy for synchronous reluctance motors considering saturation and iron losses," in *Industry Applications Conference, 2004. 39th IAS Annual Meeting. Conference Record of the 2004 IEEE*, vol. 4, 2004, pp. 2411–2417 vol.4.

[41] A. Chiba and T. Fukao, "A closed-loop operation of super high-speed reluctance motor for quick torque response," *Industry Applications, IEEE Transactions on*, vol. 28, no. 3, pp. 600–606, 1992.

[42] R. Moghaddam, "Synchronous reluctance machine (SynRM) design," Master's thesis, April, 2007.

[43] D. Staton, T. Miller, and S. Wood, "Maximising the saliency ratio of the synchronous reluctance motor," *Electric Power Applications, IEE Proceedings B*, vol. 140, no. 4, pp. 249–259, 1993.

[44] R. Moghaddam, F. Magnussen, C. Sadarangani, and H. Lendenmann, "New theoretical approach to the synchronous reluctance machine behavior and performance," in *Electrical Machines, 2008. ICEM 2008. 18th International Conference on*, 2008, pp. 1–6.

[45] S. T. Lundmark, *Course Compendium Part II for the course* LUP *625 Electric Drives*. Göteborg, Sweden, Chalmers University of Technology, Department of Energy and Environment, 2011.

[46] D. Lin, P. Zhou, W. N. Fu, Z. Badics, and Z. Cendes, "A dynamic core loss model for soft ferromagnetic and power ferrite materials in transient finite element analysis," *Magnetics, IEEE Transactions on*, vol. 40, no. 2, pp. 1318–1321, 2004.

[47] J. Luomi, *Magnetic field calculations and electrical machines*. Göteborg, Sweden, Chalmers University of Technology, Department of Energy and Environment, 1997.

[48] M. H. Rashid, *Power Electronics Handbook - Devices, Circuits, and Applications*. Elsevier, 2011.

[49] Semicron, "Theory of Loss and Temperature Calculation," 2011. [Online]. Available: http://www.semikron.com/skcompub/en/eng_3_2_1_3.pdf

[50] A. Grauers, "Design of direct-driven permanent-magnet generators for wind turbines," Ph.D Thesis, Chalmers University of Technology, Department of Electric Power Enginering, Göteborg, Sweden, October 1996.

[51] G. L. Johnson, *Wind energy systems*. Manhattan KS: Electronic version, 2006.

[52] H. Li and Z. Chen, "Overview of different wind generator systems and their comparisons," *Renewable Power Generation, IET*, vol. 2, no. 2, pp. 123–138, 2008.

[53] P. Bresesti, W. Kling, R. Hendriks, and R. Vailati, "HVDC connection of offshore wind farms to the transmission system," *Energy Conversion, IEEE Transactions on*, vol. 22, no. 1, pp. 37–43, 2007.

[54] T. Thiringer, J. Paixao, and M. Bongiorno, "Monitoring of the ride-through ability of a 2 MW wind turbine in tvååker, halland," Chalmers University of Technology, Department of Energy and Enviroment, Göteborg, Sweden, Tech. Rep., 2009.

[55] W. Wu, "Modelling of electrical machines by using a circuit-coupled finite element method."

References

[56] C. Mi, G. Slemon, and R. Bonert, "Minimization of iron losses of permanent magnet synchronous machines," *Energy Conversion, IEEE Transactions on*, vol. 20, no. 1, pp. 121–127, 2005.

[57] ——, "Modeling of iron losses of permanent-magnet synchronous motors," *Industry Applications, IEEE Transactions on*, vol. 39, no. 3, pp. 734–742, 2003.

[58] Z. Zhu and D. Howe, "Influence of design parameters on cogging torque in permanent magnet machines," *Energy Conversion, IEEE Transactions on*, vol. 15, no. 4, pp. 407–412, 2000.

[59] T. Li and G. Slemon, "Reduction of cogging torque in permanent magnet motors," *Magnetics, IEEE Transactions on*, vol. 24, no. 6, pp. 2901–2903, 1988.

[60] L. Melcescu, M. Cistelecan, O. Craiu, and H. Cosan, "A new 4/6 pole-changing double layer winding for three phase electrical machines," in *Electrical Machines (ICEM), 2010 XIX International Conference on*, 2010, pp. 1–6.

[61] E. Palmberg, *Course Compendium for a* PHD *course in Eletromagnetics Design*. Department of Energy and Enviroment, Göteborg, Sweden: Göteborg, Sweden, Chalmers University of Technology, Department of Energy and Environment, 2012, 2012.

[62] F. Meier, "Permanent magnet synchronous machines with non-overlapping concentrated windings for low speed direct-drive applications," Ph.D Thesis, Royal Institute of Technology, School of Electrical Engineering, Stockholm, Sweden, 2008.

[63] P. Salminen, "Fractional slot permanent magnet synchronous motors for low speed applications," Ph.D Thesis, Lappeenranta University of Technology, Lappeenranta, Finland, Dec. 2004.

[64] C. Sadarangani, *Electrical Machines-Design and Analysis of Induction and Permanent Magnet Motors*. Royal Insitute of Technology, Stockholm, Sweden: KTH, 2006.

[65] E. Fornasiero, L. Alberti, N. Bianchi, and S. Bolognani, "Considerations on selecting fractional slot windings," in *Energy Conversion Congress and Exposition (ECCE), 2010 IEEE*, 2010, pp. 1376–1383.

[66] M. Bogomolov, C. Kral, A. Haumer, and E. Lomonova, "Modeling of permanent magnet synchronous machine with fractional slot windings," in *IECON 2012 - 38th Annual Conference on IEEE Industrial Electronics Society*, 2012, pp. 1894–1899.

[67] Y. Miyamoto, T. Higuchi, and T. Abe, "Consideration for fractional slot winding of permanent magnet type synchronous machine," in *Electrical Machines and Systems (ICEMS), 2011 International Conference on*, 2011, pp. 1–6.

[68] S. 0750G650300, "ABB HiPak IGBT Module," Data sheet, ABB Switzerland Ltd, 2009.

[69] S. 1500E330300, "ABB HiPak IGBT Module," Data sheet, ABB Switzerland Ltd, 2011.

[70] S. 2400E170100, "ABB HiPak IGBT Module," Data sheet, ABB Switzerland Ltd, 2006.

[71] A. Mazaheri, "A 5 MW wind turbine generator system for a dc grid application," Master's thesis, 2012, 75.